Block Copolymer Self-Assembly: From Thin Film Formation to Inorganic Nanostructures

Elsa Coline Giraud, MSc

October 2019

ORCID: 0000-0002-8556-570X

Department of Chemistry,

University College Cork,

Ireland

UCC

University College Cork, Ireland

Coláiste na hOllscoile Corcaigh

Presented for the PhD. Degree to the National University of Ireland

Supervisor: Prof. Michael A. Morris

Co-Supervisor: Prof. Justin D. Holmes

Head of Department: Dr. Humphrey Moynihan

Table of Contents

Declaration

This is to certify that the work I am submitting is my own and has not been submitted for another degree, either at University College Cork or elsewhere. All external references and sources are clearly acknowledged and identified within the contents. I have read and understood the regulation of University College Cork concerning plagiarism.

Elsa Coline Giraud

Abstract

Upon self-assembly, block copolymers (BCP) can form a variety of well-ordered nanofeatures, that makes them prime candidates for use in a wide range of applications, and for alternative approaches to traditional “top-down” processes in the microelectronic industry. Self-Assembly of block copolymer thin films is widely documented, notably thermal and vapour solvent annealing.

Chapter 1 introduces the main reasons and motivations for the research carried out during this PhD. It provides a brief overview of the state of the semiconductor industry, the principle of self-assembly in block copolymer thin films and different means of selective inorganic infiltration from vapour- and liquid- phase techniques to yield nanostructures with a one-to-one registration to the block copolymer scaffold.

Chapter 2 focuses on the structural rearrangement of PS-*b*-PEO micellar thin film using an argon plasma treatment, an interesting alternative to conventional thermal and solvent vapour annealing. This process is believed to be a balance between reorganisation and possible damage on the surface due to cross-linking and etching induced. With the right conditions, perpendicular and parallel arrangement of PEO blocks are obtained within the PS matrix, proving that plasma treatment could be a suitable technique to improve the order of self-assembled thin films.

Chapter 3 details the formation of titanium dioxide nanostructures using a vapour approach for the selective infiltration of the hydrophilic PEO block. This simple, yet effective approach, relies on the volatility of the precursor, the amphiphilic properties of the block copolymer and the relative humidity to form nanodots and nanowires. Grazing incidence small angle x-ray scattering was employed to analyse the ordering of the nanowires at different stages during exposure to the titanium precursor.

In Chapter 4, a liquid-phase approach was used to produce europium-doped gadolinium oxide exhibiting characteristic photoluminescence peak that could find application in biosensing due to the small size of nanodots and nanowires.

Chapter 5 summarizes the key achievement of each chapter and examines potential future directions related to the results discussed in Chapter 2 – 4.

Acknowledgments

This dissertation is the result of few years of research at University College Cork, Ireland and other long days in Trinity College Dublin, Ireland. The work presented in this thesis has been made possible through the efforts (and motivational speeches) of my colleagues and friends.

First and foremost, I would like to thank my supervisor, Prof. Mick Morris for taking a chance and giving me the opportunity to undertake this PhD research in his laboratory. I really appreciate his help and support over the years. I would like to express my gratitude to Prof. Justin A. Holmes, my co-supervisor, for providing help and support when Mick was not available. Prof. Christophe Sinturel may never see this page, but I would like to thank him endlessly for opening the '*world of block copolymers'* during my undergrad years in Orléans.

To the UCC postdoctoral researchers, past- and present- Parvaneh, Tandra, Sibu, Cian, for their perspective and endless reminders along the process. To Ross and David, postdoctoral researchers in TCD for their motivational input. To all the members of the Department of Chemistry, especially past- and present- members of labs 115 and 343 for making tea breaks fun and keeping discussion interesting. To Eileen and Elaine, E_3 members, for all the good times, and the crazy amount of teas and coffees. To all the members of Mick's group in the 'Dublin' laboratory: you arrived at a good time, and kept on pushing, and pushing me to finish this manuscript. Special thanks to Tom, Andrew, Nadia for the laughter, for the early 7.30 am breakfast meetings and the ridiculous amount of tea (still).

Finally, I would like to thank my parents and my siblings. Aude, Florent, Gary, Clément, Alexandre, Aloïs : those years away from home were made easy due to your incredible support regarding all my decisions throughout my time in Ireland. Thank so much for your continual interest, and I hope I can finally say "*C'est fini !*" next time I see you.

And to Sean for his brilliant support in the past couple of years (and for his incredible patience).

Published Articles

(1) Highly Ordered Titanium Dioxide Nanostructures *via* a Simple One-Step Vapor-Inclusion Method in Block Copolymer Films**, Elsa C. Giraud**, Parvaneh Mokarian-Tabari, Daniel T. W. Toolan, Thomas Arnold, Andrew J. Smith, Jonathan R. Howse, Paul D. Topham, and Michael A. Morris**,** *ACS Applied Nano Materials* **2018** 1 (7), 3426-3434

Articles in Preparation

(1) Structural rearrangement of block copolymer micellar thin films using an argon plasma, **Elsa C. Giraud,** Tandra Ghoshal and Michael A. Morris.

(2) Formation of Europium-Doped Gadolinium Phosphor Nanostructures via Salt Inclusion in Self-Assembled Block Copolymer Scaffold, **Elsa C. Giraud,** Tandra Ghoshal and Michael A. Morris.

(3) Thermal Annealing of PS-PMMA Systems and the Influence of the Heating Rate on Self-Assembly Kinetics. **Elsa C. Giraud,** Parvaneh Mokarian-Tabari and Michael A. Morris.

Conferences

(1) Block Copolymer Self Assembly as a Scaffold for the Fabrication of Titanium Dioxide Nanostructures, **Elsa C. Giraud,** Parvaneh Mokarian-Tabari and Michael A. Morris. Poster Presentation at the *24th Gordon Research Conference on Polymer Physics,* Mount Holyoke College, MA, US, July 13-18, 2014.

(2) Vapour Phase Methods for Inclusion of Inorganic Materials into Block Copolymer Patterns, **Elsa C. Giraud,** Tandra Ghoshal and Michael A. Morris. Poster and Oral presentation at the *67th Irish Universities Chemistry Research Colloquium,* Maynooth, Ireland, June 25-26, 2015.

(3) Ultra-rapid Plasma Treatment to Favour Self-Assembly in PS-*b*-PEO, **Elsa C. Giraud,** Cian Cummins, Tandra Ghoshal and Michael A. Morris. Poster presentation at the *2nd DSA Symposium,* Grenoble, France, October 11-13, 2016

(4) Towards faster self-assembly in block copolymer films: the use of plasma treatment. Poster presentation at the *45th International Conference on Micro and Nano Engineering MNE2019,* Rhodes Island, Greece, September 23-26, 2019.

Common abbreviations and acronyms

AFM: Atomic Force Microscope

ALD: Atomic Layer Deposition

BCP: Block Copolymer

CVD: Chemical Vapour Deposition

DSA: Direct Self-Assembly

f: Block Volume Fraction

GISAXS: Grazing Incidence Small Angle X-ray Scattering

M_n: Molecular Weight

N: Degree of polymerisation

P4VP: Poly(4-vinylpyridine)

PEO: Poly(ethylene oxide)

PMMA: Poly(methyl methacrylate)

PS: Poly(styrene)

SA: Self-Assembly

SCFM: Self-Consistent Mean Field

SEM: Scanning Electron Microscopy

Si: Silicon

SIS: Sequential Infiltration Synthesis

TB: Titanium butoxide

TTIP: Titanium tetraisopropoxide

VUV/UV: Vacuum Ultraviolet/Ultraviolet

XPS: X-Ray Photoelectron Spectroscopy

χ: Flory-Huggins Interaction Parameter (Chi)

Chapter 1

Introduction

1.1. Abstract

The self-assembly of block copolymers (BCP) holds promises for the fabrication of nanoscale structures for use in numerous applications from the microelectronic to the pharmaceutical industry, *e.g.* their arrangement on the nanoscale can help to overcome patterning challenges in the semiconductor industry[1,2] or help with the current roadblocks in cancer therapy[3,4]. This chapter provides the reader with an overview on the phase separation of block copolymer films. This process is driven by various phenomena, depending on the thickness of the film due to its inherent properties. Furthermore, the self-assembly of block copolymer thin films is explored. Additionally, this chapter presents common methodologies for the selective infiltration of inorganic materials in microphase separated patterns. Specifically, liquid phase (*e.g.* sol-gel, metal-salt inclusion, aqueous metal reduction) and vapour phase (*e.g.* atomic layer deposition, sequential infiltration synthesis, sputtering) approaches are highlighted.

1.2. Motivation, Scope and the Microelectronic Industry

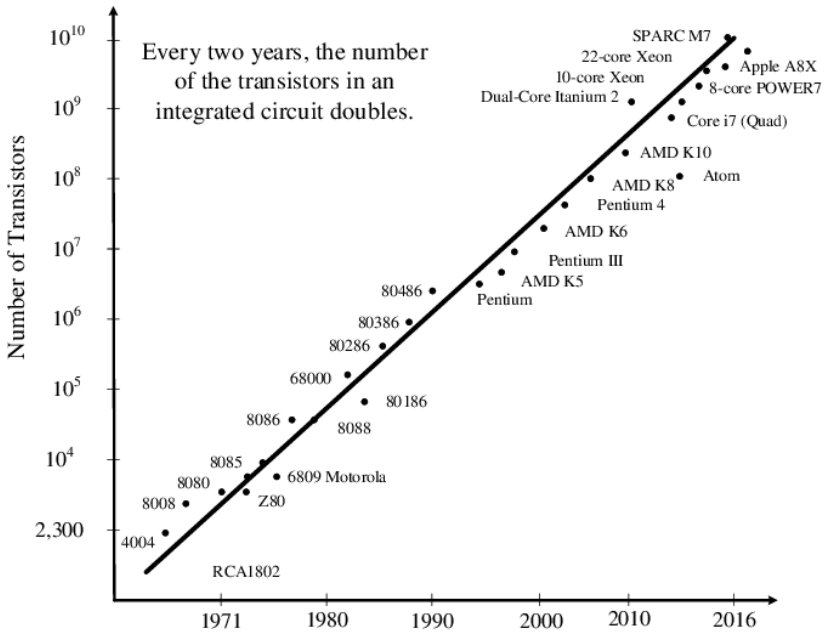

Figure 1-1. Evolution of the number of transistors for CPUs on integrated circuits, as predicted with Moore's Law[5].

Intel co-founder Gordon Moore's started a *"race to the bottom"* in the semiconductor and microelectronic industries when he wrote a paper in 1965 in which he predicted that the numbers of transistors on an integrated circuit would double every 18 months[6]. This prediction is known as Moore's Law and is described as a self-fulfilling prophecy, Figure 1-1, as this miniaturisation is included in all electronics transistor road maps. The impressive growing number of transistors per microchip, from 2300 in 1971 to over 10^{10} in the last few years, has been made possible through constant miniaturisation and continuous development in photolithographic processes[7,8].

The principle of photolithography involves transferring a pattern representing an integrated circuit component on a wafer coated with a photosensitive polymer (photoresist) by exposing it to ultraviolet (UV) light, projected through as mask as described in Figure 1-2. The UV light produces a chemical change in parts of the photoresist that has been exposed. Upon baking and removal of the chemically changed photoresist (development), the wafer is left with a protective mask that can be etched in order to transfer the pattern to the underlying substrate.

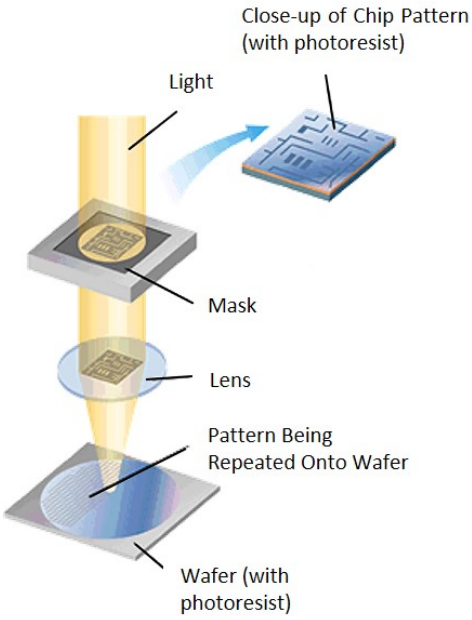

Figure 1-2. Schematic of the photolithographic process.

Huge resources were used to improve the lithographic process and, hence, the '*critical dimension'* (CD). CD is the minimum feature size that can be printed on a chip or wafer and is

therefore linked to the resolution. It can be described with the Rayleigh equation, (1-1); which relates the CD of a process to the numerical aperture and wavelength of the imaging system :

$$CD = k_1 \frac{\lambda}{NA} \qquad (1\text{-}1)$$

$$NA = n \sin\theta \qquad (1\text{-}2)$$

where λ is the wavelength of the imaging system, k_1 a process-dependent factor, NA the numerical aperture, n the refractive index, and $\sin\theta$ the maximum half-angle of the cone of light that can enter or exit the lens.

Improving the critical dimension was first implemented by changing the light source and decreasing the wavelength (λ) going from 436 nm (Hg lamp) in the 1980 to 193 nm (ArF laser). With a light source of 193 nm, it is possible to get small dimensions of around 100 nm. Alternatively, the CD can be improved by increasing the numerical aperture (NA) either by using larger lens and/or replacing the usual air gap between the wafer surface and the final lens with a liquid medium that has a refractive index higher than one. This technique is called immersion lithography (193i) and is widely used in the microelectronic industry. For example, water immersion reduces the CD by having a numerical aperture that could theoretically approach the refractive index of water (1.44) although most of the immersion tools have a NA of 1.35 realising 45 nm down to 28 nm feature size[9].

Before trying to reduce the light source wavelength, research was focused on alternatives to conventional lithography such as multipatterning techniques, nanoimprint lithography[10] or ultraviolet lithography[11,12]. However, those techniques are not without drawbacks, with resolution limitations fast approaching. Moreover, with decreased size of transistors to the nanoscale, development and manufacturing cost have grown larger in an exponential fashion. This trend is also known as Moore's Second Law – or Rock's Law[13,14]. Going forward, it is widely accepted that alternative methods to purely "top-down" approaches are necessary to pursue miniaturisation. "Bottom-up" processes have emerged for the fabrication of nanoscale features with one potential technique showing great promises: the self-assembly of block copolymers[15-17].

1.3. Block Copolymer Self Assembly

The concept of *"macromolecules"* can be traced back to 1920 when Hermann Staudinger published a paper entitled *"Uber Polymerisation"* where he described the first *"polymerization"* process by linking together a large number of small molecules to form high molecular weight molecules known as *"polymers"*. Meeting criticism and strong opposition from his peers whom argued no compounds could exceed molecular weights of 5000, he is nowadays considered as the father of macromolecular chemistry. His relentless efforts to establish the science of large molecules was rewarded when he won the Nobel Prize in Chemistry, in 1953. The development of polymer sciences sparked the production and the synthesis of new materials such as poly(methyl methacrylate), polyethylene, and polyurethane-polyurea copolymer brought to market in 1933, 1939 and 1959 respectively.

1.3.1. Block Copolymers

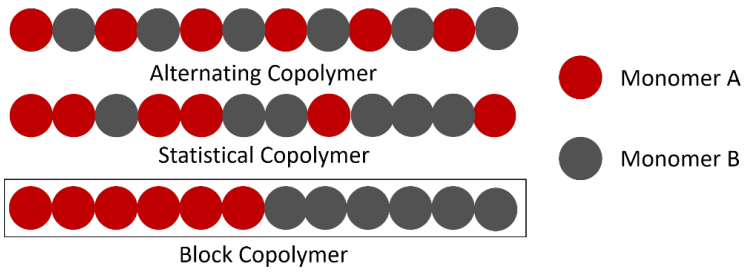

Figure 1-3. Schematic representation of some configurations of linear copolymers.

A copolymer is a polymer derived from two (or more) monomeric species, as opposed to a homopolymer where only one monomer is used. Depending how the monomeric species (units) arrange themselves, they can form linear (Figure 1-3) or branched copolymers (*incl.* brush, comb and graft, star copolymer).

Block Copolymers (BCP) are a specific type of linear copolymer and consist of two or more chemically incompatible polymeric chains (blocks) covalently bonded to each other. Block copolymer presented in Figure 1-3 is a diblock copolymer. Alternatively, other architectures include tri- and multiblock copolymer, heteroarms and other complex organisations[18-20] as illustrated in Figure 1-4:

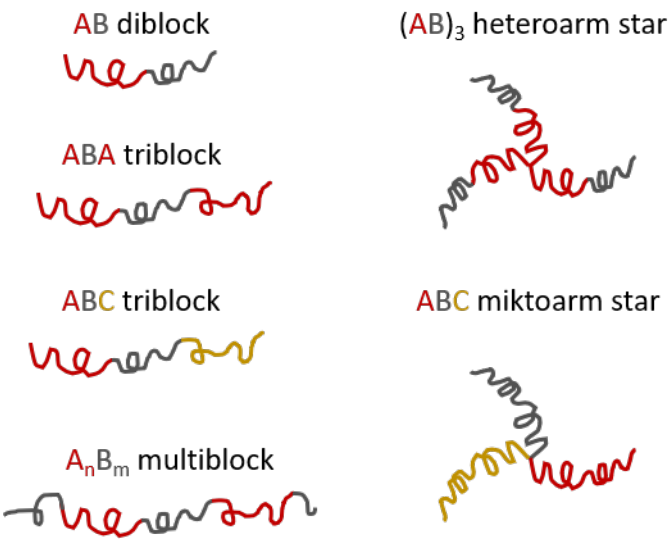

Figure 1-4. Schematic representation of some block copolymer architectures such as linear diblock, triblock and multiblock copolymers (left side) as well as heteroarms and miktoarm star polymer (right side). Schematic inspired by Ruzette and Leibler[21].

Block copolymers find applications in numerous areas from the textile to the microelectronic industry, primarily as lithographical mask but also as templates for a wide range of materials and nanostructures due to their propensity to form a large variety of well-ordered structures at a nanometre scale (10 – 100 nm).

1.3.2. Phase Separation, Microphase Separation and Phase Behaviour

The propensity of block copolymers to form well-ordered nanostructures is due to the size and immiscibility of the blocks they are made of, through a process called self-assembly (SA). This process is driven by mutual interactions of the blocks toward reducing the system free energy. Whitesides *et al.* identified two types of self-assembly: static and dynamic[22]. Static self-assembly, or equilibrium self-assembly, refers to stable (global or local) equilibrium structures characterised by a maximum in the system's entropy and no systematic energy flows[23] *e.g.* formation of molecular crystals, assemblies of block copolymers. In contrast, dynamic self-assembly refers to ordered nonequilibrium structures[24], prevented from reaching a free energy minimum. As such, they require a continuous supply of external energy to balance the intrinsic interaction between the building blocks (or between the blocks in the case of BCPs).

Molecular self-assembly is the most well-known subfield of dynamic self-assembly and can be either an intramolecular or intermolecular process: it does not involve chemical reactions but relies on electromagnetic and non-covalent interactions *i.e.* hydrogen bonding, metal coordination, van der Waals forces, hydrophobic force and/or electrostatic. The thermodynamics for a reversible spontaneous process of self-assembly can be described by the Gibbs Free Energy equation (1-3) below:

$$\Delta G_{SA} = \Delta H_{SA} - T\Delta S_{SA} \qquad (1\text{-}3)$$

where ΔG_{SA} is the change in free energy, where ΔH_{SA} is the enthalpy change and is representative of the intermolecular forces between the assembling unit, and where $T\Delta S_{SA}$ is the entropy change.

For a self-assembly process to be spontaneous, the change in free energy ΔG_{SA} must be negative. As the system becomes more ordered, the entropy of the system decreases meaning ΔS_{SA} is negative. As such, for the process to be spontaneous, the change of enthalpy ΔH_{SA} must be negative and in excess of entropy term. However, the Free Gibbs equation also shows that the process is temperature-dependent above a specific temperature, $T\Delta S_{SA}$ is greater than ΔH_{SA} and the self-assembly process do not occur.

In polymer blends, mixtures of A and B homopolymers, repulsion between the immiscible A and B blocks leads to macrophase separation at equilibrium. A common analogy is the mixture of water and oil: thermodynamic incompatibility facilitates their phase separation in order to minimise the contact between them, leading to the formation of two distinctive layers. In the case of block copolymers, however, both homopolymers (blocks) are linked together by a covalent bond, limiting their separation to the length of their chains. Because of the size constraint, this process is referred to as microphase separation.

When mixing two homopolymers, the Flory-Huggins equation describes the free energy of the system:

$$\frac{\Delta G_{mix}}{k_B T} = \frac{1}{N_A}\ln(f_A) + \frac{1}{N_B}\ln(f_B) + f_A f_B \chi_{AB} \qquad (1\text{-}4)$$

where k_B is the Boltzmann constant, f the block volume fraction, N the degree of polymerisation (or segment size), and χ_{AB} the Flory-Huggins interaction parameter.

This parameter describes the interaction between solvent and polymer molecules and is related to the degree of incompatibility of the different blocks. In order to calculate this parameter, few assumptions are made. Firstly, polymer segments and solvent molecules are randomly distributed in a volume R and are of the same size. Secondly, only the nearest neighbour interactions are included in the calculation. It can be defined as:

$$\chi_{AB} = \frac{z}{k_B T}\left(\varepsilon_{AB} - \frac{\varepsilon_{AA} + \varepsilon_{BB}}{2}\right) \qquad (1\text{-}5)$$

where z is the (average) number of contacts per molecule (also called lattice coordination number), k_B the Boltzmann constant, T the absolute temperature, and ε the interaction energy between two molecules.

As seen in equation (1-5), the degree of incompatibility χ_{AB} increases with the interaction energy between molecules A and B, ε_{AB}. Also, χ_{AB} can be controlled by modifying the temperature. In the case of a simple diblock copolymer, χ_{AB} can be re-written in terms of the Hildebrand solubility parameter (δ) which measure the tendency of one material to dissolve in another one particularly for non-polar materials:

$$\chi_{AB} = \frac{V_{ref}}{RT}\,(\delta_A - \delta_B)^2 \qquad (1\text{-}6)$$

where V_{ref} is an arbitrary reference volume normally taken as the molar free volume, R the gas constant and T the temperature.

However, since the theory was based on the behaviour of hydrocarbon solvents, δ did not account for polar forces and hydrogen bonding. A more accurate equation, re-written in term of Hansen solubility parameters (δ_d, δ_p, δ_h), would be:

$$\chi_{AB} = \frac{V_S}{4RT}\left[4\left(\delta_{d,A} - \delta_{d,B}\right)^2 + \left(\delta_{p,A} - \delta_{p,B}\right)^2 + \left(\delta_{h,A} - \delta_{h,B}\right)^2\right] \qquad (1\text{-}7)$$

where the Hansen solubility parameters are δ_d for dispersion (non-polar) forces, δ_p for dipolar intermolecular forces and δ_h for hydrogen bonding. At a given temperature, the repulsion between A and B blocks increases with χ_{AB}.

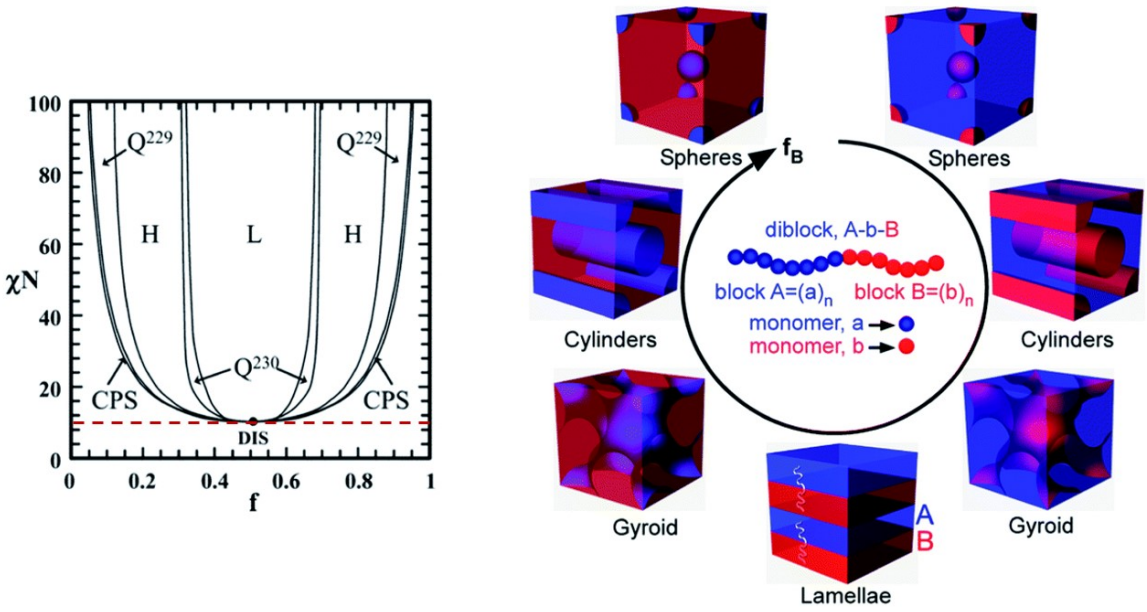

Figure 1-5. Phase diagram of a diblock copolymer by self-consistent field theory with CPS: close packed spheres, H: hexagonally packed cylinder, L: lamellae, Q^{229}: body centred spheres, Q^{230}: double-gyroid and DIS: disordered. Schematic illustration of microstructures with increased f_B, volume fraction of block B. Adapted from Hu *et al.* (Soft Matter, 2014)[25]

The product $\chi_{AB}N$ governs the microphase separation, and a theoretical value above 10.5 is needed for ordered morphologies to occur for symmetric systems (f = 0.5), as illustrated in Figure 1-5. Under this theoretical value, the order-disorder limit is reached meaning the two blocks are either too alike (χ_{AB}) or the segment size of their chain are too small (N). At $\chi_{AB}N$ ≈ 10.5, the phase separation will occur, and the system is considered to be in the weak segregation limit. At this stage, polymer chains are interpenetrating and the interface between blocks is not neat. Increasing $\chi_{AB}N \gg 10.5$ allows for strong segregation of the blocks, with a very narrow interface and, hence, better definition. Those weak and strong segregation limits were tied together with the self-consistent mean field (SCMF) theory[26-29].

For block copolymers with $\chi_{AB}N \geq 10.5$, the morphologies are determined by the volume fractions f_A and f_B of both blocks. Nanostructures observed are spherical, cylindrical, gyrodial or lamellar features as illustrated in Figure 1-5.

1.3.3. Block Copolymer Thin Films

Over the last decades, an increasing number of research has been focused on block copolymer films. Properties of sub-micron thick films differ from those in the bulk, with a great change in

the glass transition temperature, the viscosity or the chain diffusion coefficients[30]. As for the morphologies and domain sizes, whilst they are determined in bulk by the Flory-Huggins interaction parameter (χ_{AB}), the degree of polymerisation (N), and the volume fraction (f), additional factors have an impact on phase separation for thin and thick block copolymer films. These factors include the role of surface-interface interaction between atmosphere-polymer and polymer-substrate, the film thickness, and the domain periodicity or microdomain spacing (L_0). Furthermore, the domain periodicity (L_0) of the phase-separated microdomains can be described as follow:

$$L_0 \sim \alpha N^{2/3} \chi^{1/6} \qquad (1\text{-}8)$$

where α is the characteristic segment length of a monomer unit[31]. This means smaller periods (and features) can be achieved by reducing the degree of polymerization N while maintaining $\chi_{AB}N$ over the critical value for phase separation. Hu et al. considered the division between bulk and thin film (thickness less than c*a.* 200 nm) anecdotal, but essential for the phase separation and their possible directed self-assembly[25]. Directed assembly in the bulk can be achieve through shear alignment[32-34], electric field alignment[35,36], magnetic field alignment[37,38], temperature gradient field[39,40] (also referred as zone annealing), or directional solidification[41,42]. Although phase separation of block copolymer thick films is feasible, this thesis focuses on thin films.

1.3.4. Interfacial constraints and the effect of the thickness

Interaction of polymer with the interface is usually described by its interfacial tension, δ. This interfacial tension denotes the energy cost necessary to create an interface between the polymer and the environment. In the case of a thin film, two interfaces are available: polymer-substrate, and polymer-air. The polymer block with the lowest surface energy is attracted to the polymer-air interface while the block with the lowest interfacial energy is attracted to the polymer-substrate interface. If both blocks have similar surface energy, they wet equally the surface, and the substrate is considered as neutral.

In some cases, both substrate-polymer and air-polymer interfaces are wet by the same block: this phenomenon is called symmetric wetting, and the film thickness is an integer multiple of the microdomain spacing, L_0. Asymmetric wetting happens when the blocks have preferential

wetting to one of the interfaces. In this case, the thickness of the film is expressed by $(n+ ½)L_0$. Both wettings are shown in Figure 1-6.

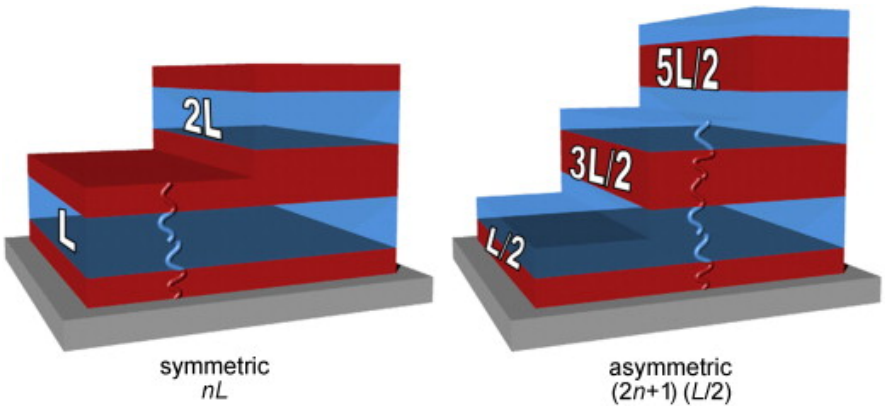

Figure 1-6. Schematics showing the effect of selective interfacial wetting in block copolymer thin films. Reprint from Darling[43]

The thickness of the block copolymer thin film can impact the morphology of the nanofeatures: there is a constraint imposed by the commensurability[44-46] between the film thickness (*t)* and the microdomain spacing (L_0). Incommensurability occurs when the film thickness is not equal to nL_0 or $(n+ ½)$ L_0 and the block copolymer film deviates from the its equilibrium morphology in order to relive the imposed frustration. If the film possesses a free surface, *i.e.* if it not confined, the surface topography presents terraces[47] of step height L_0 as presented in the Figure 1-6 above.

Manipulation of polymer-air and polymer-substrate interfaces provides greater control on the orientation of the nanostructures. A common method is to change the substrate for another material such as fused silica, sapphire or silicon nitride. Common substrate alteration would be sputtering of carbon- or gold- layer on the surface, homopolymer (brush) grafting, UV ozone treatment or Piranha solution treatment. Manipulating the polymer-air interface can be done by using solvent vapours: this is a common method, used in microphase separation *via* solvent annealing.

1.3.5. Thermal- and Solvent Vapours Annealing to Promote Self-Assembly.

Formation of block copolymer thin films often include the use of a spin-coater to yield a film thickness around 20-100 nm. During spin coating, the casting solution dries at a fast rate

trapping the block copolymer chains into a metastable equilibrium. Resulting morphologies included poorly ordered arrangement, disorganized microdomains and presence of micellar structures. To enhance the ordering of the microdomains, thermal-, solvent vapour annealing or a mix thereof are often used to promote chain mobility and facilitate microphase separation[48-51].

Thermal annealing is the simplest technique to induce phase separation of block copolymer films. Traditionally, films were heated in a vacuum oven for extended periods of time, above the glass-transition temperature (T_g) and under the order-to-disorder (T_{OTD}) and degradation temperatures. PS-*b*-PMMA BCPs, for example, were reported by Russell *et al.* to form order microdomains[52] after annealing for 1 day at 160 °C. However, the use of thermal annealing alone to induce phase separation is a lengthy process limited by the overall molecular weight of the block copolymer: high molecular weight systems hinder chain rearrangement.

Solvent vapour annealing is another effective annealing technique yielding highly ordered microdomains in block copolymer thin films[51]. Compared to thermal annealing, this process can be highly effective timewise. This is due to multiple factors such as (i) the dramatic enhancement of the chain mobility by the presence of plasticizing solvent species, (ii) the interaction between the solvent and the block copolymer chains and (iii) the swelling of the block copolymer thin films[43,54]. Additionally, solvent evaporation can induce an ordering propagating into the film and yielding perpendicular orientation, with final morphology being a function of the evaporation rate[55-56]. Phase separation using a solvent vapour process have been reported in several block copolymer films such as PS-*b*-PEO[57-59], PS-*b*-P2VP[60], PS-*b*-P4VP[61] or PS-*b*-PLA[62,63].

Combination of solvent and thermal annealing is another widely used technique[64,65] that combine increasing the polymer chains mobility, while promoting self-assembly *via* modification of the polymer-air interface, and evaporation induced ordering among other parameters. Alternatively, other interesting and unconventional techniques have been used to induce phase separation such as microwave annealing[66-68] or lased induced millisecond thermal annealing[69].

1.4. Block Copolymer and Inorganic Infiltration Strategies

The capabilities of block copolymers to self-assemble under thermal and solvent annealing to form microdomains with nanoscale dimensions is useful for bottom-up approaches and alternatives to top-down lithography technique in the microelectronic industry. Alteration to block copolymer systems, *e.g.* infiltration of inorganic material with BCP microdomains, results in nanostructures that find application as etch mask for nanolithography[70,71]. Alternatively, the formation of hybrid material can potentially interest a range of environmental, medical, optical and energy applications. This section focuses on some inorganic infiltration strategies in order to give some background to Chapters 3 and 4 of this these.

1.4.1. Liquid Phase Approaches

Spin coating inorganic nanoparticles is an attractive and efficient approach for the generation of functional nanofeatures. Combined with further treatment that would remove the organic (block copolymer) scaffold, *e.g.* calcination or exposure to UV ozone, can lead to the formation of ferroelectric or magnetic material[72]. Liu *et al.* assembled gold nanorods arrays onto air plasma-treated PS-*b*-PMMA template[73]. Gold nanorods infiltrated selectively the PMMA block and were converted to gold nanowires after a simple etch process due to confinement effect and capillary forces. Placement of nanomaterials *via* spin-coating is an easy method that could lead to the formation of numerous inorganic nanofeatures such as Fe_2O_3 nanoparticles or ZnO nanorods[74]. In the above examples, the block copolymer template only acts as a scaffold for the placement of nanoparticles and nanorods. This approach benefits from advances in nanoparticle synthesis, which allows researchers to tune composition, crystallinity, shape and particle size before their infiltration[75].

Alternatively, we have demonstrated a rich variety of metal oxide nanostructures *via* infiltration of a metal-salt solution into PS-*b*-PEO, PS-*b*-P2VP and PS-*b*-P4VP templates. Precursor solution is spun cast onto ethanol *"activated"* templates, a crucial step allowing the infiltration of the inorganic salt into the hydrophilic block. Ghoshal *et al.* fabricated a wide range of nanomaterials such as Fe_2O_3 that find applications as a hard mask[76] or Ce_2O_3 that could find potential applications as catalyst or phosphor[77]. This approach yields nanostructures with tuneable pitch size and dimension as their size depends on the block copolymer scaffold. Additionally, it is possible to tune the diameter by varying the precursor solution concentration, while keeping the pitch size identical.

Mayeda *et al.* also decoupled phase-separation of block copolymer template to the precursor infiltration with the hydrophilic block of the block copolymer, by developing the SPICE method (spincoat-pattern-immerse-complex-etch)[78]. Metal oxides are formed by immersion of the template in the precursor solution included MgO, Al_2O_3, MnO_2 and TiO_2 with the latter presenting a 13% increase in photocatalytic activity over TiO_2 produced by evaporation induced self-assembly (EISA). This method is similar to the one developed by Cha *et al*[79] in 2015, where they immersed self-assembled BCP thin film templates in a $HAuCl_4$ acidic aqueous solution to selectively deposit Au ionic precursors into P4VP domains. Resulting gold array were used as a seed to create Au@Ag core-shell nanoparticles with tuneable broadband enhancement of plasmonic resonance.

In-situ sol-gel methods[80-85] use a sacrificial block copolymer to arrange metal salt precursors and subsequently reduce, calcine or oxidise the composite to (i) remove the organic matrix and (ii) form the templated material. Within sol-gel methods, EISA is quite popular : polymer and metal precursors are combined in a single solution and spun cast on a substrate. The evaporation of the solvent creates an ordering evaporation front, common to induce ordering in block copolymer thin films. However, the ordering of the nanofeatures produced *via* EISA[86] remains quite poor due to polymer/metal inter- and intra- interaction inhibiting chains mobility and reorganisation[87].

1.4.2. Vapour Phase Approaches

Top-down approaches towards the fabrication of functional materials fabrication comprises atomic layer deposition (ALD) and sequential infiltration synthesis (SIS) among other techniques.

Atomic layer deposition is a versatile technique for depositing inorganic material for the controlled formation of uniform layers *via* vapour phase precursors. ALD processes allow the formation of a thin film on a substrate by exposing its surface to alternate gaseous species, referred to as precursors which are inserted as a series of non-overlapping and sequential pulses. The systematic nature of ALD cycles enables atomic level precursors through self-limiting surface reaction[88]. Peng *et al.* synthesised patterned nanomaterials, Al_2O_3 and TiO_2, by combining the unique molecular-level management of an ALD process with highly ordered self-assembled block copolymers. Li *et al.* developed 3D highly porous metal oxide networks of interconnected nanotubes yielding excellent pore connectivity and high porosity[89]. The

reaction between the metal precursors and the carbonyl groups of PMMA blocks, in PS-*b*-PMMA self-assembled templated, followed by removal of the polymer matrix generated nanostructures of aluminium dioxide or titanium dioxide. In 2014, Moon *et al.* used a porous PS template and an ALD alumina coating to generate highly ordered line and dot array with a pattern periodicity of 28 nm[90]. By using ALD to induce pattern density multiplication, they managed to reduce the pattern periodicity to 14 nm. Corresponding feature size was 5 nm, proving the possibility of ultrafine nanopatterning.

Sequential infiltration Synthesis is an ADL-derived process, that was first used by Peng *et al.* Using an appropriate precursor, they infiltrated PS-*b*-PMMA pattern with reactants such as trimethyl aluminium to create -Al-CH_3 and -Al-OH groups inside PMMA blocks[91]. Those groups then provide reactive sites for nucleation and growth of different materials such as Al_2O_3, SiO_2, ZnO and W. Tseng *et al.* used SIS on PS-*b*-PMMA templates to yield inorganic nanostructures that serves directly as a robust etch mask[92]. The etch mask mimics the block copolymer templates, shows improved transfer fidelity on the substrate over conventional liquid phase approaches. Although PS-*b*-PMMA templates are under scrutiny for the generation of hard mask using SIS process, they can also yield nanostructures with interesting applications. Rahman *et al.* used PS-*b*-PMMA phase separated films and exposed them to three sequential cycles of tri(methyl aluminium) and water. Upon etching of the self-assembled alumina pattern, they obtained densely packed silicon nanotextures with sub-50 nm feature sizes that could enhance the broadband antireflection band and improved planar antireflection coating[93].

1.5. Thesis overview

As explained in this chapter, block copolymers self-assembly provides an alternative for the fabrication of nanoscale structures (*e.g.* cylinders, lamellae) using a *"bottom-up"* approach as opposed to *"top-down"* ones. In particular, directed self-assembly of block copolymers is viewed as a promising approach that could overcome the current limitation of conventional photolithography (by bypassing it) to yield nanostructures of 3-7 nm. IMEC, CEA-Leti, IBM have R&D centres actively working on the development of nanostructures obtained *via* phase-separation of block copolymer thin films that could meet industrial expectations. Their approaches are multiple from the synthesis of high-χ block copolymers (with low degree of polymerisation) to their phase separation, reduction of defect densities, elimination of wet chemistry, etc. There are numerous approaches to make this technology industrially viable.

This thesis, financed by the semiconductor research corporation (SRC), addresses a few points that find relevance in the semiconductor industry. Focusing on the self-assembly of PS-*b*-PEO block copolymer systems, highly versatile and amphiphilic, this manuscript addresses the development of two novel techniques to (i) rearrange the thin film surface and (ii) yield inorganic nanostructures.

In Chapter 2, the surface rearrangement of PS-*b*-PEO micellar thin films using an argon plasma treatment is discussed. For the first time, perpendicular and parallel arrangement of PEO blocks in a PS matrix is observed using an alternative method to vapour and thermal annealing. By eliminating the use of solvent during the annealing phase (toluene), this process is more environmental- and user-friendly. Furthermore, the short processing time (matter of seconds) could multiply the number of wafers produced per hour in an industrial setting, while reducing the cost associated with heating during thermal annealing. Elsa Coline Giraud performed the block copolymer experiments and coordinated the research with the help of Tandra Ghoshal. Cian Cummins helped with the angled SEM images in Figure S2-3.

A novel vapour approach for the selective infiltration of PEO blocks by titanium precursor, yielding titanium dioxide nanostructures, is demonstrated in Chapter 3. This technique relies on the volatility of the precursor, the relative humidity of the processing chamber and the amphiphilic properties of the block copolymer. This technique was also developed for the industry with the main goals being (i) the suppression of a liquid-phase approach for the selective inclusion and (ii) avoiding the use of costly and bulky equipment (ALD, CVD chambers). Elsa Coline Giraud performed the block copolymer experiments and coordinated the research with the help of Parvaneh Mokarian-Tabari. Parvaneh Mokarian-Tabari performed ellipsometric measurement and the GISAXS experiment in Diamond Light Source with the help of Daniel T. W. Toolan, Thomas Arnold, Andrew J. Smith, Jonathan R. Howse, and Paul D. Topham.

Chapter 4 is not related to any industry requirement and details the formation of europium-doped gadolinium oxide nanostructures using a liquid-phase approach. Obtained nanostructures exhibit characteristic photoluminescence peak that could find application in biosensing due to the size nanodots (28-32 nm in diameter). Elsa Coline Giraud performed the experiments and coordinated the research with the help of Tandra Ghoshal.

Chapter 5 summarises key accomplishments of each chapter and examines the future potential directions related to results discussed in Chapter 2 – 4.

1.6. References

(1) Barnola, S.; Posseme, N.; Landis, S.; Darnon, M. 3 - Patterning Challenges in Microelectronics. *In Plasma Etching Processes for CMOS Devices Realization*; Posseme, N., Ed.; Elsevier, **2017**; pp 59–94. https://doi.org/10.1016/B978-1-78548-096-6.50003.

(2) Morris, M. A. Directed Self-Assembly of Block Copolymers for Nanocircuitry Fabrication. *Microelectronic Engineering* **2015**, 132, 207–217. https://doi.org/10.1016/j.mee.2014.08.009.

(3) Houdaihed, L.; Evans, J. C.; Allen, C. Overcoming the Road Blocks: Advancement of Block Copolymer Micelles for Cancer Therapy in the Clinic. *Mol. Pharmaceutics* **2017**, 14 (8), 2503–2517. https://doi.org/10.1021/acs.molpharmaceut.7b00188.

(4) Binkhathlan, Z.; Lavasanifar, A. Chapter 15 - Effects of Block Copolymer Micelles on the Pharmacokinetics of Encapsulated Drugs. In *Nanoarchitectonics in Biomedicine*; Grumezescu, A. M., Ed.; William Andrew Publishing, **2019**; pp 507–546. https://doi.org/10.1016/B978-0-12-816200-2.00017-7.

(5) Aydin, O.; Uçar, O. Design for Smaller, Lighter and Faster ICT Products: Technical Expertise, Infrastructures and Processes. *Adv. Sci. Technol. Eng. Syst. J.* **2017**, *2* (3), 1114–1128. https://doi.org/10.25046/aj0203141.

(6) Moore, G. E. Cramming More Components onto Integrated Circuits, Reprinted from Electronics, Volume 38, Number 8, April 19, 1965, Pp.114 Ff. *IEEE Solid-State Circuits Society Newsletter* **2006**, *11* (5), 33–35. https://doi.org/10.1109/N-SSC.2006.4785860.

(7) Rühe, J. And There Was Light: Prospects for the Creation of Micro- and Nanostructures through Maskless Photolithography. *ACS Nano* **2017**, *11* (9), 8537–8541. https://doi.org/10.1021/acsnano.7b05593.

(8) Liaros, N.; Tomova, Z.; Razo, S. A. G.; Cohen, S. R.; Fourkas, J. T.; Wolf, S. M.; Thum, M.; Falvey, D. E.; Ogden, H. M.; Mullin, A. S.; et al. The State of the Art in Multicolor Visible Photolithography. In *Novel Patterning Technologies 2018*; International Society for Optics and Photonics, 2018; Vol. 10584, p 1058407. https://doi.org/10.1117/12.2297653.

(9) Wuping Wang; Long Qin; Zhengkai Yang; Yulong Li; Zhibiao Mao; Yu Zhang. Illumination Optimization for Lithography Tools Ope Matching at 28 Nm Nodes. In *2017 China Semiconductor Technology International Conference (CSTIC)*; 2017; pp 1–4. https://doi.org/10.1109/CSTIC.2017.7919767.

(10) Traub, M. C.; Longsine, W.; Truskett, V. N. Advances in Nanoimprint Lithography. *Annual Review of Chemical and Biomolecular Engineering* **2016**, *7* (1), 583–604. https://doi.org/10.1146/annurev-chembioeng-080615-034635.

(11) Ashby, P. D.; Olynick, D. L.; Ogletree, D. F.; Naulleau, P. P. Resist Materials for Extreme Ultraviolet Lithography: Toward Low-Cost Single-Digit-Nanometer Patterning. *Advanced Materials* **2015**, *27* (38), 5813–5819. https://doi.org/10.1002/adma.201501171.

(12) Mack, C. A. Reducing Roughness in Extreme Ultraviolet Lithography. *JM3* **2018**, *17* (4), 041006. https://doi.org/10.1117/1.JMM.17.4.041006.

(13) Schaller, R. R. Moore's Law: Past, Present and Future. *IEEE Spectrum* **1997**, *34* (6), 52–59. https://doi.org/10.1109/6.591665.

(14) Rupp, K.; Selberherr, S. The Economic Limit to Moore's Law. *IEEE Transactions on Semiconductor Manufacturing* **2011**, *24* (1), 1–4. https://doi.org/10.1109/TSM.2010.2089811.

(15) Stoykovich, M. P.; Kang, H.; Daoulas, K. Ch.; Liu, G.; Liu, C.-C.; de Pablo, J. J.; Müller, M.; Nealey, P. F. Directed Self-Assembly of Block Copolymers for Nanolithography: Fabrication of Isolated Features and Essential Integrated Circuit Geometries. *ACS Nano* **2007**, *1* (3), 168–175. https://doi.org/10.1021/nn700164p.

(16) Durand, W. J.; Blachut, G.; Maher, M. J.; Sirard, S.; Tein, S.; Carlson, M. C.; Asano, Y.; Zhou, S. X.; Lane, A. P.; Bates, C. M.; et al. Design of High-χ Block Copolymers for Lithography. *Journal of Polymer Science Part A: Polymer Chemistry* **2015**, *53* (2), 344–352. https://doi.org/10.1002/pola.27370.

(17) Lo, T.-Y.; Krishnan, M. R.; Lu, K.-Y.; Ho, R.-M. Silicon-Containing Block Copolymers for Lithographic Applications. *Progress in Polymer Science* **2018**, *77*, 19–68. https://doi.org/10.1016/j.progpolymsci.2017.10.002.

(18) Zheng, W.; Wang, Z.-G. Morphology of ABC Triblock Copolymers. *Macromolecules* **1995**, *28* (21), 7215–7223. https://doi.org/10.1021/ma00125a026.

(19) Hadjichristidis, N.; Iatrou, H.; Pitsikalis, M.; Pispas, S.; Avgeropoulos, A. Linear and Non-Linear Triblock Terpolymers. Synthesis, Self-Assembly in Selective Solvents and in Bulk. *Progress in Polymer Science* **2005**, *30* (7), 725–782. https://doi.org/10.1016/j.progpolymsci.2005.04.001.

(20) Park, C.; Yoon, J.; Thomas, E. L. Enabling Nanotechnology with Self Assembled Block Copolymer Patterns. *Polymer* **2003**, *44* (22), 6725–6760. https://doi.org/10.1016/j.polymer.2003.08.011.

(21) Ruzette, A.-V.; Leibler, L. Block Copolymers in Tomorrow's Plastics. *Nature Mater* **2005**, *4* (1), 19–31. https://doi.org/10.1038/nmat1295.

(22) Whitesides, G. M.; Grzybowski, B. Self-Assembly at All Scales. *Science* **2002**, *295* (5564), 2418–2421. https://doi.org/10.1126/science.1070821.

(23) Thomas, S.; Shanks, R.; Chandran, S. Nanostructured Polymer Blends; William Andrew, **2013**; pp 258, chapter 7.

(24) Grzybowski, B. A.; Fitzner, K.; Paczesny, J.; Granick, S. From Dynamic Self-Assembly to Networked Chemical Systems. Chem. Soc. Rev. **2017**, 46 (18), 5647–5678. https://doi.org/10.1039/C7CS00089H.

(25) Hu, H.; Gopinadhan, M.; O. Osuji, C. Directed Self-Assembly of Block Copolymers: A Tutorial Review of Strategies for Enabling Nanotechnology with Soft Matter. *Soft Matter* **2014**, *10* (22), 3867–3889. https://doi.org/10.1039/C3SM52607K.

(26) Matsen, M. W.; Schick, M. Stable and Unstable Phases of a Diblock Copolymer Melt. *Phys. Rev. Lett.* **1994**, *72* (16), 2660–2663. https://doi.org/10.1103/PhysRevLett.72.2660.

(27) Whitmore, M. D.; Vavasour, J. D. Self-Consistent Field Theory of Block Copolymers and Block Copolymer Blends. *Acta Polymerica* **1995**, *46* (5), 341–360. https://doi.org/10.1002/actp.1995.010460501.

(28) Matsen, M. W.; Bates, F. S. Unifying Weak- and Strong-Segregation Block Copolymer Theories. *Macromolecules* **1996**, *29* (4), 1091–1098. https://doi.org/10.1021/ma951138i.

(29) Petera, D.; Muthukumar, M. Self-Consistent Field Theory of Diblock Copolymer Melts at Patterned Surfaces. *J. Chem. Phys.* **1998**, *109*, 5101–5107. https://doi.org/10.1063/1.477124.

(30) Green, P. F.; Limary, R. Block Copolymer Thin Films: Pattern Formation and Phase Behavior. *Advances in Colloid and Interface Science* **2001**, *94* (1), 53–81. https://doi.org/10.1016/S0001-8686(01)00055-0.

(31) Hadjichristidis, N.; Hirao, A. Anionic Polymerization: Principles, Practice, Strength, Consequences and Applications; Springer, **2015**, chapter 5.

(32) Angelescu, D. E.; Waller, J. H.; Adamson, D. H.; Deshpande, P.; Chou, S. Y.; Register, R. A.; Chaikin, P. M. Macroscopic Orientation of Block Copolymer Cylinders in Single-Layer Films by Shearing. *Advanced Materials* **2004**, *16* (19), 1736–1740. https://doi.org/10.1002/adma.200400643.

(33) Amundson, K.; Helfand, E.; Quan, X.; Smith, S. D. Alignment of Lamellar Block Copolymer Microstructure in an Electric Field. 1. Alignment Kinetics. *Macromolecules* **1993**, *26* (11), 2698–2703. https://doi.org/10.1021/ma00063a010.

(34) Amundson, K.; Helfand, E.; Quan, X.; Hudson, S. D.; Smith, S. D. Alignment of Lamellar Block Copolymer Microstructure in an Electric Field. 2. Mechanisms of Alignment. *Macromolecules* **1994**, *27* (22), 6559–6570. https://doi.org/10.1021/ma00100a047.

(35) Thurn-Albrecht, T.; DeRouchey, J.; Russell, T. P.; Kolb, R. Pathways toward Electric Field Induced Alignment of Block Copolymers. *Macromolecules* **2002**, *35* (21), 8106–8110. https://doi.org/10.1021/ma020567v.

(36) Xu, T.; Zhu, Y.; Gido, Samuel. P.; Russell, T. P. Electric Field Alignment of Symmetric Diblock Copolymer Thin Films. *Macromolecules* **2004**, *37* (7), 2625–2629. https://doi.org/10.1021/ma035805g.

(37) Gopinadhan, M.; Majewski, P. W.; Beach, E. S.; Osuji, C. O. Magnetic Field Alignment of a Diblock Copolymer Using a Supramolecular Route. *ACS Macro Lett.* **2012**, *1* (1), 184–189. https://doi.org/10.1021/mz2001059.

(38) Gopinadhan, M.; Majewski, P. W.; Choo, Y.; Osuji, C. O. Order-Disorder Transition and Alignment Dynamics of a Block Copolymer Under High Magnetic Fields by In Situ X-Ray Scattering. *Phys. Rev. Lett.* **2013**, *110* (7), 078301. https://doi.org/10.1103/PhysRevLett.110.078301.

(39) Singh, G.; Yager, K. G.; Berry, B.; Kim, H.-C.; Karim, A. Dynamic Thermal Field-Induced Gradient Soft-Shear for Highly Oriented Block Copolymer Thin Films. *ACS Nano* **2012**, *6* (11), 10335–10342. https://doi.org/10.1021/nn304266f.

(40) Berry, B. C.; Bosse, A. W.; Douglas, J. F.; Jones, R. L.; Karim, A. Orientational Order in Block Copolymer Films Zone Annealed below the Order−Disorder Transition Temperature. *Nano Lett.* **2007**, *7* (9), 2789–2794. https://doi.org/10.1021/nl071354s.

(41) Yoon, J.; Lee, W.; Thomas, E. L. Highly Oriented Thin-Film Microdomain Patterns of Ultrahigh Molecular Weight Block Copolymers via Directional Solidification of a Solvent. *Advanced Materials* **2006**, *18* (20), 2691–2694. https://doi.org/10.1002/adma.200600741.

(42) Angelescu, D. E.; Waller, J. H.; Adamson, D. H.; Register, R. A.; Chaikin, P. M. Enhanced Order of Block Copolymer Cylinders in Single-Layer Films Using a Sweeping Solidification Front. *Advanced Materials* **2007**, *19* (18), 2687–2690. https://doi.org/10.1002/adma.200602904.

(43) Darling, S. B. Directing the Self-Assembly of Block Copolymers. *Progress in Polymer Science* **2007**, *32* (10), 1152–1204. https://doi.org/10.1016/j.progpolymsci.2007.05.004.

(44) Huang, E.; Mansky, P.; Russell, T. P.; Harrison, C.; Chaikin, P. M.; Register, R. A.; Hawker, C. J.; Mays, J. Mixed Lamellar Films: Evolution, Commensurability Effects, and Preferential Defect Formation. *Macromolecules* **2000**, *33* (1), 80–88. https://doi.org/10.1021/ma9912711.

(45) Sunday, D. F.; Ashley, E.; Wan, L.; Patel, K. C.; Ruiz, R.; Kline, R. J. Template–Polymer Commensurability and Directed Self-Assembly Block Copolymer Lithography. *Journal of Polymer Science Part B: Polymer Physics* **2015**, *53* (8), 595–603. https://doi.org/10.1002/polb.23675.

(46) Cheng, J. Y.; Ross, C. A.; Thomas, E. L.; Smith, H. I.; Vancso, G. J. Templated Self-Assembly of Block Copolymers: Effect of Substrate Topography. *Advanced Materials* **2003**, *15* (19), 1599–1602. https://doi.org/10.1002/adma.200305244.

(47) Xiang, H.; Shin, K.; Kim, T.; Moon, S.; Mccarthy, T. J.; Russell, T. P. The Influence of Confinement and Curvature on the Morphology of Block Copolymers. *Journal of Polymer Science Part B: Polymer Physics* **2005**, *43* (23), 3377–3383. https://doi.org/10.1002/polb.20641.

(48) Cummins, C.; Mokarian-Tabari, P.; Andreazza, P.; Sinturel, C.; Morris, M. A. Solvothermal Vapor Annealing of Lamellar Poly(Styrene)-Block-Poly(d,l-Lactide) Block Copolymer Thin Films for Directed Self-Assembly Application. *ACS Appl. Mater. Interfaces* **2016**, *8* (12), 8295–8304. https://doi.org/10.1021/acsami.6b00765.

(49) Cavicchi, K. A.; Berthiaume, K. J.; Russell, T. P. Solvent Annealing Thin Films of Poly(Isoprene-b-Lactide). *Polymer* **2005**, *46* (25), 11635–11639. https://doi.org/10.1016/j.polymer.2005.09.072.

(50) Kim, T. H.; Hwang, J.; Hwang, W. S.; Huh, J.; Kim, H.-C.; Kim, S. H.; Hong, J. M.; Thomas, E. L.; Park, C. Hierarchical Ordering of Block Copolymer Nanostructures by Solvent Annealing Combined with Controlled Dewetting. *Advanced Materials* **2008**, *20* (3), 522–527. https://doi.org/10.1002/adma.200700651.

(51) Sinturel, C.; Vayer, M.; Morris, M.; Hillmyer, M. A. Solvent Vapor Annealing of Block Polymer Thin Films. *Macromolecules* **2013**, *46* (14), 5399–5415. https://doi.org/10.1021/ma400735a.

(52) Kim, H.-C.; Jia, X.; Stafford, C. M.; Kim, D. H.; McCarthy, T. J.; Tuominen, M.; Hawker, C. J.; Russell, T. P. A Route to Nanoscopic SiO2 Posts via Block Copolymer Templates. *Advanced Materials* **2001**, *13* (11), 795–797. https://doi.org/10.1002/1521-4095(200106)13:11<795::AID-ADMA795>3.0.CO;2-1.

(53) Stahl, B. C.; Kramer, E. J.; Hawker, C. J.; Lynd, N. A. Controlled Co-Solvent Vapor Annealing and the Importance of Quenching Conditions in Thin-Film Block Copolymer Self-Assembly. *Journal of Polymer Science Part B: Polymer Physics* **2017**, *55* (15), 1125–1130. https://doi.org/10.1002/polb.24366.

(54) Hayat, J.; Mitra, I.; Qiao, Y.; Stein, G. E.; Tang, C. Improving Humidity-Controlled Solvent Annealing Processes for Block Copolymer Poly(Ethylene Oxide)-b-Polystyrene. *European Polymer Journal* **2015**, *71*, 476–489. https://doi.org/10.1016/j.eurpolymj.2015.08.019.

(55) Susca, E. M.; Beaucage, P. A.; Thedford, R. P.; Singer, A.; Gruner, S. M.; Estroff, L. A.; Wiesner, U. Preparation of Macroscopic Block-Copolymer-Based Gyroidal Mesoscale Single Crystals by Solvent Evaporation. *Advanced Materials* **2019**, *31* (40), 1902565. https://doi.org/10.1002/adma.201902565.

(56) Wan, L.; Ji, S.; Liu, C.-C.; Craig, G. S. W.; Nealey, P. F. Directed Self-Assembly of Solvent-Vapor-Induced Non-Bulk Block Copolymer Morphologies on Nanopatterned Substrates. *Soft Matter* **2016**, *12* (11), 2914–2922. https://doi.org/10.1039/C5SM02829A.

(57) Metwalli, E.; Perlich, J.; Wang, W.; Diethert, A.; Roth, S. V.; Papadakis, C. M.; Müller-Buschbaum, P. Morphology of Semicrystalline Diblock Copolymer Thin Films upon Directional Solvent Vapor Flow. *Macromolecular Chemistry and Physics* **2010**, *211* (19), 2102–2108. https://doi.org/10.1002/macp.201000343.

(58) Zhang, M.; Yang, L.; Yurt, S.; Misner, M. J.; Chen, J.-T.; Coughlin, E. B.; Venkataraman, D.; Russell, T. P. Highly Ordered Nanoporous Thin Films from Cleavable Polystyrene-Block-Poly(Ethylene Oxide). *Advanced Materials* **2007**, *19* (12), 1571–1576. https://doi.org/10.1002/adma.200602461.

(59) Ghoshal, T.; Holmes, J. D.; Morris, M. A. Development of Ordered, Porous (Sub-25 Nm Dimensions) Surface Membrane Structures Using a Block Copolymer Approach. *Sci Rep* **2018**, *8* (1), 1–11. https://doi.org/10.1038/s41598-018-25446-0.

(60) Jin, C.; Olsen, B. C.; Luber, E. J.; Buriak, J. M. Nanopatterning via Solvent Vapor Annealing of Block Copolymer Thin Films. *Chem. Mater.* **2017**, *29* (1), 176–188. https://doi.org/10.1021/acs.chemmater.6b02967.

(61) van Zoelen, W.; Asumaa, T.; Ruokolainen, J.; Ikkala, O.; ten Brinke, G. Phase Behavior of Solvent Vapor Annealed Thin Films of PS-b-P4VP(PDP) Supramolecules. *Macromolecules* **2008**, *41* (9), 3199–3208. https://doi.org/10.1021/ma702780c.

(62) Phillip, W. A.; Hillmyer, M. A.; Cussler, E. L. Cylinder Orientation Mechanism in Block Copolymer Thin Films Upon Solvent Evaporation. *Macromolecules* **2010**, *43* (18), 7763–7770. https://doi.org/10.1021/ma1012946.

(63) Ho, R.-M.; Tseng, W.-H.; Fan, H.-W.; Chiang, Y.-W.; Lin, C.-C.; Ko, B.-T.; Huang, B.-H. Solvent-Induced Microdomain Orientation in Polystyrene-b-Poly(l-Lactide) Diblock Copolymer Thin Films for Nanopatterning. *Polymer* **2005**, *46* (22), 9362–9377. https://doi.org/10.1016/j.polymer.2005.07.069.

(64) Gotrik, K. W.; Ross, C. A. Solvothermal Annealing of Block Copolymer Thin Films. *Nano Lett.* **2013**, *13* (11), 5117–5122. https://doi.org/10.1021/nl4021683.

(65) Gotrik, K. W.; Lam, T.; Hannon, A. F.; Bai, W.; Ding, Y.; Winterstein, J.; Alexander-Katz, A.; Liddle, J. A.; Ross, C. A. 3D TEM Tomography of Templated Bilayer Films of Block Copolymers. *Advanced Functional Materials* **2014**, *24* (48), 7689–7697. https://doi.org/10.1002/adfm.201402457.

(66) Zhang, X.; Harris, K. D.; Wu, N. L. Y.; Murphy, J. N.; Buriak, J. M. Fast Assembly of Ordered Block Copolymer Nanostructures through Microwave Annealing. *ACS Nano* **2010**, *4* (11), 7021–7029. https://doi.org/10.1021/nn102387c.

(67) Borah, D.; Shaw, M. T.; Holmes, J. D.; Morris, M. A. Sub-10 Nm Feature Size PS-b-PDMS Block Copolymer Structures Fabricated by a Microwave-Assisted Solvothermal Process. *ACS Appl. Mater. Interfaces* **2013**, *5* (6), 2004–2012. https://doi.org/10.1021/am302830w.

(68) Jin, C.; Murphy, J. N.; Harris, K. D.; Buriak, J. M. Deconvoluting the Mechanism of Microwave Annealing of Block Copolymer Thin Films. *ACS Nano* **2014**, *8* (4), 3979–3991. https://doi.org/10.1021/nn5009098.

(69) Jacobs, A. G.; Jung, B.; Ober, C. K.; Thompson, M. O. Control of PS-b-PMMA Directed Self-Assembly Registration by Laser Induced Millisecond Thermal Annealing. In *Alternative Lithographic Technologies VI*; International Society for Optics and Photonics, 2014; Vol. 9049, p 90492B. https://doi.org/10.1117/12.2046513.

(70) Jeong, S.-J.; Kim, J. Y.; Kim, B. H.; Moon, H.-S.; Kim, S. O. Directed Self-Assembly of Block Copolymers for next Generation Nanolithography. *Materials Today* **2013**, *16* (12), 468–476. https://doi.org/10.1016/j.mattod.2013.11.002.

(71) Kwak, J.; Mishra, A. K.; Lee, J.; Lee, K. S.; Choi, C.; Maiti, S.; Kim, M.; Kim, J. K. Fabrication of Sub-3 Nm Feature Size Based on Block Copolymer Self-Assembly for Next-Generation Nanolithography. *Macromolecules* **2017**, *50* (17), 6813–6818. https://doi.org/10.1021/acs.macromol.7b00945.

(72) Darling, S. B.; Yufa, N. A.; Cisse, A. L.; Bader, S. D.; Sibener, S. J. Self-Organization of FePt Nanoparticles on Photochemically Modified Diblock Copolymer Templates. *Advanced Materials* **2005**, *17* (20), 2446–2450. https://doi.org/10.1002/adma.200500960.

(73) Liu, Z.; Huang, H.; He, T. Large-Area 2D Gold Nanorod Arrays Assembled on Block Copolymer Templates. *Small* **2013**, *9* (4), 505–510. https://doi.org/10.1002/smll.201201503.

(74) Son, J. G.; Bae, W. K.; Kang, H.; Nealey, P. F.; Char, K. Placement Control of Nanomaterial Arrays on the Surface-Reconstructed Block Copolymer Thin Films. *ACS Nano* **2009**, *3* (12), 3927–3934. https://doi.org/10.1021/nn900914q.

(75) Daniel, M.-C.; Astruc, D. Gold Nanoparticles: Assembly, Supramolecular Chemistry, Quantum-Size-Related Properties, and Applications toward Biology, Catalysis, and Nanotechnology. *Chem. Rev.* **2004**, *104* (1), 293–346. https://doi.org/10.1021/cr030698+.

(76) Ghoshal, T.; Fleming, P. G.; Holmes, J. D.; Morris, M. A. The Stability of "Ce2O3" Nanodots in Ambient Conditions: A Study Using Block Copolymer Templated Structures. *J. Mater. Chem.* **2012**, *22* (43), 22949–22957. https://doi.org/10.1039/C2JM35073D.

(77) Ghoshal, T.; Shaw, M. T.; Bolger, C. T.; Holmes, J. D.; Morris, M. A. A General Method for Controlled Nanopatterning of Oxide Dots: A Microphase Separated Block Copolymer Platform. *J. Mater. Chem.* **2012**, *22* (24), 12083–12089. https://doi.org/10.1039/C2JM30468F.

(78) Mayeda, M. K.; Hayat, J.; Thomas H Epps, I. I. I.; Lauterbach, J. Metal Oxide Arrays from Block Copolymer Thin Film Templates. *J. Mater. Chem. A* **2015**, *3* (15), 7822–7829. https://doi.org/10.1039/C5TA00117J.

(79) Cha, S. K.; Mun, J. H.; Chang, T.; Kim, S. Y.; Kim, J. Y.; Jin, H. M.; Lee, J. Y.; Shin, J.; Kim, K. H.; Kim, S. O. Au–Ag Core–Shell Nanoparticle Array by Block Copolymer Lithography for Synergistic Broadband Plasmonic Properties. *ACS Nano* **2015**, *9* (5), 5536–5543. https://doi.org/10.1021/acsnano.5b01641.

(80) Sun, Z.; Kim, D. H.; Wolkenhauer, M.; Bumbu, G. G.; Knoll, W.; Gutmann, J. S. Synthesis and Photoluminescence of Titania Nanoparticle Arrays Templated by Block-Copolymer Thin Films. *Chem. Eur. J. of Chem. Phys.* **2006**, *7* (2), 370–378. https://doi.org/10.1002/cphc.200500340.

(81) Orilall, M. C.; Wiesner, U. Block Copolymer Based Composition and Morphology Control in Nanostructured Hybrid Materials for Energy Conversion and Storage: Solar Cells, Batteries, and Fuel Cells. *Chem. Soc. Rev.* **2011**, *40* (2), 520–535. https://doi.org/10.1039/C0CS00034E.

(82) Kästle, G.; Boyen, H.-G.; Weigl, F.; Lengl, G.; Herzog, T.; Ziemann, P.; Riethmüller, S.; Mayer, O.; Hartmann, C.; Spatz, J. P.; et al. Micellar Nanoreactors—Preparation and Characterization of Hexagonally Ordered Arrays of Metallic Nanodots. *Advanced Functional Materials* **2003**, *13* (11), 853–861. https://doi.org/10.1002/adfm.200304332.

(83) Boyen, H.-G.; Kästle, G.; Zürn, K.; Herzog, T.; Weigl, F.; Ziemann, P.; Mayer, O.; Jerome, C.; Möller, M.; Spatz, J. P.; et al. A Micellar Route to Ordered Arrays of Magnetic Nanoparticles: From Size-Selected Pure Cobalt Dots to Cobalt–Cobalt Oxide Core–Shell Systems. *Advanced Functional Materials* **2003**, *13* (5), 359–364. https://doi.org/10.1002/adfm.200304319.

(84) Polleux, J.; Rasp, M.; Louban, I.; Plath, N.; Feldhoff, A.; Spatz, J. P. Benzyl Alcohol and Block Copolymer Micellar Lithography: A Versatile Route to Assembling Gold and in Situ Generated Titania Nanoparticles into Uniform Binary Nanoarrays. *ACS Nano* **2011**, *5* (8), 6355–6364. https://doi.org/10.1021/nn201470f.

(85) Spatz, J. P.; Mössmer, S.; Hartmann, C.; Möller, M.; Herzog, T.; Krieger, M.; Boyen, H.-G.; Ziemann, P.; Kabius, B. Ordered Deposition of Inorganic Clusters from Micellar Block Copolymer Films. *Langmuir* **2000**, *16* (2), 407–415. https://doi.org/10.1021/la990070n.

(86) Brinker, C. J. Evaporation-Induced Self-Assembly: Functional Nanostructures Made Easy. *MRS Bulletin* **2004**, *29* (9), 631–640. https://doi.org/10.1557/mrs2004.183.

(87) Lee, D. H.; Han, S. H.; Joo, W.; Kim, J. K.; Huh, J. Phase Behavior of Polystyrene-Block-Poly(4-Vinylpyridine) Copolymers Coordinated by Metal Chloride. *Macromolecules* **2008**, *41* (7), 2577–2583. https://doi.org/10.1021/ma702403k.

(88) Peng, Q.; Tseng, Y.-C.; Darling, S. B.; Elam, J. W. Nanoscopic Patterned Materials with Tunable Dimensions via Atomic Layer Deposition on Block Copolymers. *Adv. Mater.* **2010**, *22* (45), 5129–5133. https://doi.org/10.1002/adma.201002465.

(89) Li, F.; Yao, X.; Wang, Z.; Xing, W.; Jin, W.; Huang, J.; Wang, Y. Highly Porous Metal Oxide Networks of Interconnected Nanotubes by Atomic Layer Deposition. *Nano Lett.* **2012**, *12* (9), 5033–5038. https://doi.org/10.1021/nl3028312.

(90) Moon, H.-S.; Kim, J. Y.; Jin, H. M.; Lee, W. J.; Choi, H. J.; Mun, J. H.; Choi, Y. J.; Cha, S. K.; Kwon, S. H.; Kim, S. O. Atomic Layer Deposition Assisted Pattern Multiplication of Block Copolymer Lithography for 5 Nm Scale Nanopatterning. *Advanced Functional Materials* **2014**, *24* (27), 4343–4348. https://doi.org/10.1002/adfm.201304248.

(91) Peng, Q.; Tseng, Y.-C.; Darling, S. B.; Elam, J. W. A Route to Nanoscopic Materials via Sequential Infiltration Synthesis on Block Copolymer Templates. *ACS Nano* **2011**, *5* (6), 4600–4606. https://doi.org/10.1021/nn2003234.

(92) Tseng, Y.-C.; Peng, Q.; Ocola, L. E.; Elam, J. W.; Darling, S. B. Enhanced Block Copolymer Lithography Using Sequential Infiltration Synthesis. *J. Phys. Chem. C* **2011**, *115* (36), 17725–17729. https://doi.org/10.1021/jp205532e.

(93) Rahman, A.; Ashraf, A.; Xin, H.; Tong, X.; Sutter, P.; Eisaman, M. D.; Black, C. T. Sub-50-Nm Self-Assembled Nanotextures for Enhanced Broadband Antireflection in Silicon Solar Cells. *Nat Commun* **2015**, *6* (1), 1–6. https://doi.org/10.1038/ncomms6963.

Chapter 2

Structural rearrangement of block copolymer micellar thin films using an argon plasma

2.1. Abstract

Block Copolymers (BCPs) self-assembly have shown promise as a next generation nanolithography technology as their phase separation at a nanometre scale can overcome the limitations of conventional lithography. Critical step towards this approach is reproducible phase separation of the films with perpendicular orientation of the BCP nanostructures to the surface. Here, we report on using an alternative method to conventional thermal and solvent annealing by exposing as-cast micellar PS-*b*-PEO thin film to a mild argon plasma. Resulting films show perpendicular and parallel arrangement of poly(ethylene oxide) to the surface, depending on the morphology of the initial micelle shape. This method is a fast process, that could reduce thermo-solvent annealing time (hours) to few seconds, while allowing phase separation on large and industrial substrates. We discuss the balance between the energy input of the argon plasma leading to large-scale surface reorganisation, and the possible damage of the surface due to cross-linking and/or etching.

2.2. Introduction

The semiconductor industry is facing multiple challenges in order to reduce the critical dimension of advanced semiconductor devices while improving performance and microprocessor density[1]. Going beyond the resolution limit of conventional photolithography necessitates the development of multiple "top-down" and "bottom-up" approaches. Among "bottom-up" methods, directed self-assembly (DSA) of block copolymer (BCPs) thin films has been studied extensively and recognised as a promising strategy to extend Moore's Law due to their use as hard masks in nanolithography[2-4]. Linear di-block copolymers can self-assemble in various nanostructured morphologies with dimensions ranging from sub-10 to 100+ nm (i.e. cylinders, lamellae, spheres) due to the chemical incompatibility of the blocks. Desired morphologies can be tailored by varying the molecular weight of both blocks, their volume fraction, their interaction and the degree of polymerization *N*.

Great efforts have been made to promote the self-assembly of BCPs[5-7]. Nowadays, phase separation can be achieved with numerous techniques such as thermal[8-11] solvent vapour[12,13] annealing or a combination[14] thereof. Other promising techniques are laser annealing[15], the use of solvent gradient during solvent annealing[16] and the use of external forces such as an electric field[17] or shear force[18]. For the semiconductor industry, a perpendicular $C_{\perp}$

orientation of the microdomain to the surface substrate is desirable. Unfortunately, the surface/interface energy difference between the two blocks often leads to a $C_{\parallel}$ orientation[19]. Perpendicular orientation has been implemented by providing neutral conditions between the surface and the interface of the film by using random polymer brushes[20,21] surfactants[22] or top-coats[23,24]

Recently, plasma treatments have emerged as an alternative to top-coat methods[24,25]. Lu *et al.* plasma-oxidised a star-block PS-PDMS to provide a neutral layer at the surface to obtain perpendicular cylinders after a simple thermal annealing procedure[26]. Oh *et al.* used an argon filtered plasma on various block copolymer systems to produce a cross-linked layer[27]. Perpendicular orientation of BCP microdomains was also obtained after thermal annealing. In these two approaches, the cross-liked layer had to be removed and/or etched to expose the underlying nanostructures.

Here, we introduce a mild argon plasma treatment to induce the structural rearrangement of spun casted thin films, from two PS-*b*-PEO systems without the need of top-coat removal and thermal annealing favouring perpendicular ordering. Inert argon gas was chosen to minimize chemical reaction between the surface of the thin film and the plasma. Although argon ion bombardment and vacuum ultraviolet/ultraviolet irradiation inevitably lead to both etching and cross-linking[28-30] of polymers, we believe the energy provided by the argon plasma is sufficient to drive the structural reorganisation without significant etching damage or chemical modifications. We show that this simple process enables the formation of vertical and parallel cylinders domain alike after few seconds of treatment.

2.3. Experimental Section

Materials. PS-*b*-PEO diblock copolymers were purchased from Polymer Source Inc. and used without any further purification. The two systems are represented as SEO_{42K} and SEO_{32K}; their number-average molecular weights (Mn) are 42-11.5 kg mol^{-1} and 32-11 kg mol^{-1} with polydispersity indexes, PDI, of 1.07 and 1.06 respectively. Highly polished single-crystal silicon <100> wafers (p-type) with a native oxide layer were used as a substrate without any attempt to remove the native layer (~2-5 nm). Toluene (HPLC grade, 99.9%) was purchased from Sigma-Aldrich and used as received.

Micellar Film Formation. Silicon substrates were cleaned by ultrasonication in acetone and toluene for 20 min respectively and dried under a nitrogen stream. The PS-*b*-PEO copolymers were dissolved in toluene by stirring at room temperature to yield a 1 wt% solution for at least an hour prior to use. PS-*b*-PEO thin films were spin-coated onto silicon substrates at 3000 rpm for 30 s using a SCS G3P-8 spincoater.

Argon Plasma Treatment on As-Cast Micellar Thin Films. As-cast PS-*b*-PEO films were exposed to Argon plasma in a Plasmalab System 100 (Oxford instrument) for Reactive Ion Etching (RIE). Plasma treatment was performed using a range of argon flow gas (6, 10 and 15 sccm) for different periods of time (3 to 20 s) under various RF forward powers ranging from 60 to 200 W.

Characterization. BCP film thicknesses were measured using a spectroscopic ellipsometer "Plasmos SD2000 Ellipsometer" at a fixed angle of 70 °C on at least five different locations on the sample. Average values were reported as the measured thickness value. A two-layer β-spline model (SiO_2 + BCP) was used to simulate experimental data. Surface morphologies of the nanostructured thin films were analysed with an AFM (Park systems, XE-100 and XE-7) in tapping mode (XE-100) and true non-contact mode (XE-7) under ambient conditions using silicon microcantilever probes tip. Topographic, phase and amplitude images were recorded simultaneously. Static contact angles of deionized water were measured at ambient temperature using a Data Physics Contact Angle goniometer (OCA15 model). Combined with X-Ray Photoelectron Spectroscopy (XPS) analysis, water contact angle gives an insight regarding the evolution of the micelles under argon plasma treatment. XPS was performed on VG Scientific ECSAlab Mk II system using Al Kα mono X-ray source (1486.6 eV). SEM measurements were carried out on a JEOL model FEI FP 2031/11 Inspect F field emission at an accelerating voltage of 5 or 10 keV.

2.4. Results and Discussion

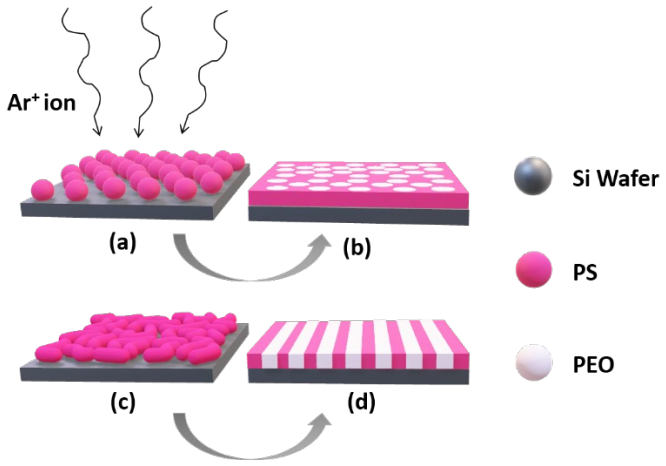

Scheme 2-1. Illustration of the structural reorganisation process of PS-*b*-PEO structure using a mild argon plasma treatment. (a,c) As-cast thin film of PS-*b*-PEO solution on silicon substrate showing spherical and wormlike micelle and (b,d) resulting ordered PS-*b*-PEO thin film after exposure to argon plasma.

Micellization of PS-b-PEO Block Copolymer on Silicon Substrate.

The block copolymer used has PEO as the minority, cylinder forming block in a PS matrix; it was dissolved in a toluene casting solution. We used the Hansen solubility method to estimate the polymer-solvent Flory-Huggins interaction parameter χ_{AB}[31]. Systems with a low interaction parameter are highly selective *i.e.* as cast polymer solutions have higher chance to produce micelle features. From the Hansen method, the interaction parameter is given by equation (2-1):

$$\chi_{AB} = \frac{V_S}{4RT}\left[4\left(\delta_{d,A} - \delta_{d,B}\right)^2 + \left(\delta_{p,A} - \delta_{p,B}\right)^2 + \left(\delta_{h,A} - \delta_{h,B}\right)^2\right] \quad (2\text{-}1)$$

where V_s is the molecular volume, R is the gas constant and T is the temperature (K). Material specific solubility parameters for non-specific dispersive (δ_d), specific polar (δ_p) and specific hydrogen bonding (δ_h) interaction for solvent and PE, PEO were found from the literature[31,32]. The polymer-solvent Flory-Huggins interaction parameters were estimated as $\chi_{PS\text{-}tol} = 0.06$ and $\chi_{PEO\text{-}tol} = 1.96$. Because of the low interaction parameter between PS and toluene, solutions formed are turbid and likely contains micelles with a PS corona and PEO core. When the casting solution was spun-casted onto silicon substrate, micelle features survived the spin-coating and solvent evaporation: as-cast films presents micelles

arrangement on the silicon surface, with water contact angle (WCA) measurement confirming the hypothesis of a PS corona with a value of ~89° (value typical of PS).

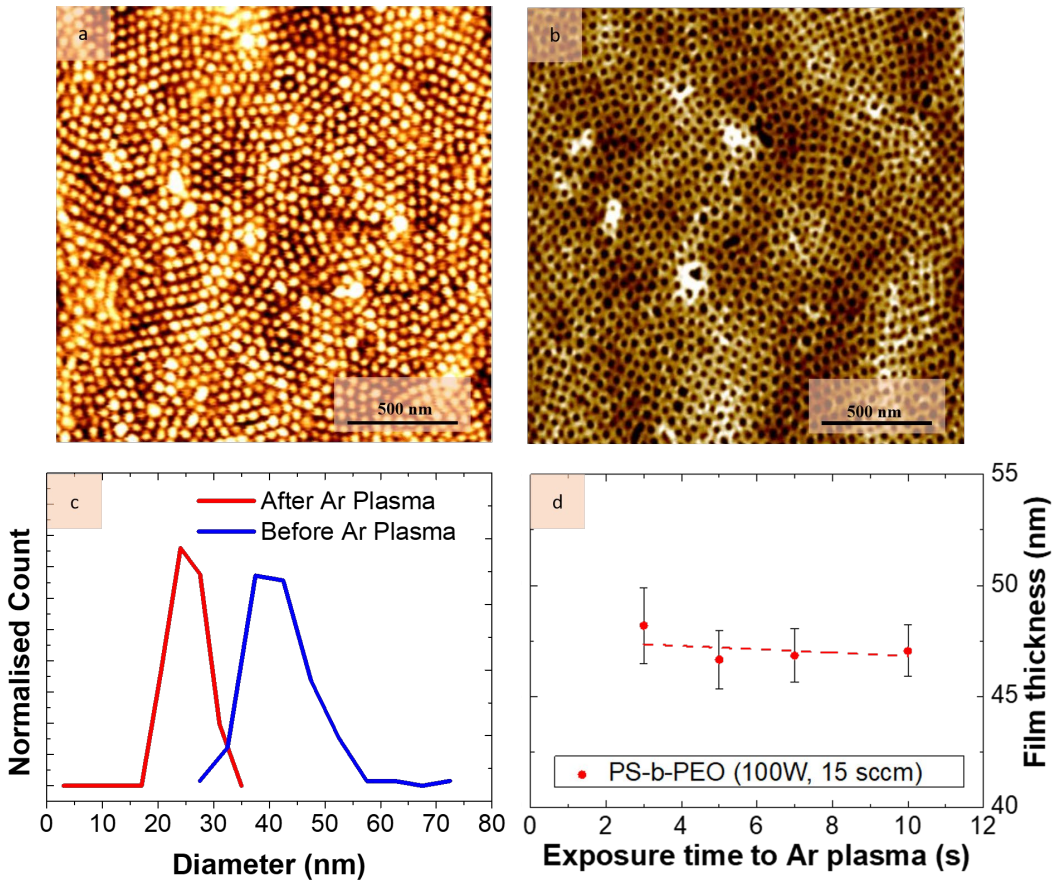

Figure 2-1. Morphology differences of PS-b-PEO thin film. Tapping mode AFM of (a) as-cast PS-b-PEO thin film and (b) argon plasma treated thin film @ 100W for 7 seconds and with an argon flow of 10 sccm. (c) shows the evolution of diameter from the micellar form (blue line) to the rearranged PEO domains (red line). (d) shows the evolution of the film thickness as a function of exposure time to argon plasma using a RF power of 100 W and an argon flow of 15 sccm.

Figure 2-1 shows the representative tapping mode AFM topography images of PS-*b*-PEO film (a) before i.e. as-cast and (b) after argon plasma treatment for 7 seconds, with an argon flow of 10 sccm and a RF power of 100 W. In Figure 2-1 (a), the average diameter of the micelles was measured to be 42.3 (± 6.3) nm with a centre-to-centre distance between two micelles of 58.7 (± 4.8) nm. In the experimental conditions used, they most likely form a monolayer of densely packed micelles forming disordered hexagonal or cubic arrangement. The existence of a micellar structure can be confirmed with the measured thickness presented in Figure 2-1 (d) after 3 s, 5 s, 7 s and 10 s of exposure to a 100 W argon plasma with a 15 sccm argon flow : the average diameter of the micelles (~42 nm) is in close agreement with

the film thickness before any plasma treatment (~49 nm). Indeed, in case of a monolayer of packed micelles, the thickness is of the film is comparable to the diameter of spherical micelles. The small difference of 7 nm could be due to the existence of a wetting layer on the silicon substrate, under the array of micelles. Figure 2-1 (b) shows the evolution of the micelle arrangement into a perpendicular arrangement of PEO domains within a PS matrix. Although the pitch size is similar, 58.4 (± 7.6) nm, there is a clear decrease in the diameter of PEO domains to 27.1 (± 3.0) nm, as seen in Figure 2-1 (c). The diameter of the PEO cylinders after exposure to argon plasma is comparable with dimensions obtained in previous studies for phase separated BCP films exposed to thermo-solvent annealing[33]. Lighter colours in the AFM correspond to PS block while darker colours are attributed to PEO block.

Structural rearrangement after exposure to argon plasma.

To further investigate the role of argon plasma on structural reorganisation and/or surface modification of the block-copolymer thin film, a range of parameters were explored such as applied RF forward power, argon (Ar) flow rate and duration of plasma exposure to the films. During any argon plasma treatment, a few phenomena can occur such as carbonization from accelerated Ar ion physically bombarding the surface and forming a modified amorphous carbon-like layer within few seconds[34]. Ion bombardment can also result in cross-linking of polymer chains near the surface. Increased roughness and chemical modification of polymer films can occur from exposure to VUV/UV photons leading to breakage of C-H and C-C bonds in the polymer backbone[35]. In the present work, the use of argon plasma treatment was conducted on micelles and worm-like micelles. Spherical micelles were obtained with a PS-*b*-PEO system having a molecular weight of 42K-*b*-11.5K while a smaller molecular weight of 32K-*b*-11K (higher volume fraction of PEO block) was required to obtain wormlike micelles. In the case of wormlike micelles, PEO lines in a PS matrix are obtained post argon plasma treatment. Information regarding work on worm-like micelles, using PS-*b*-PEO 32K-*b*-11K is available in the appendix: Figure S2-1, Figure S2-2, and Figure S2-3.

Figure 2-2 shows the morphology at the surface after exposure to argon plasma alongside their corresponding water contact angle images and data using a flow rate of 10 sccm. As cast films in Figure 2-2 (a-f) were exposed to argon plasma with a RF power of 60W for 7 s to 20 s and resulted in a change of the surface morphology. Films in Figure 2-2 (a-c), after 7 – 12 s of exposure, showed the disappearance of micelle structure and the formation of

PEO cylinder in a $C_{\perp}$ arrangement with water contact angle values ranging from 88° to 93°. After 12 s of exposure to argon plasma, a drop in WCA is observed to 44° - 50° where it reaches a plateau, Figure 2-2 (d-f). The evolution of the wettability for those samples can be found in Figure 2-3 where the corresponding water contact angle values are plotted.

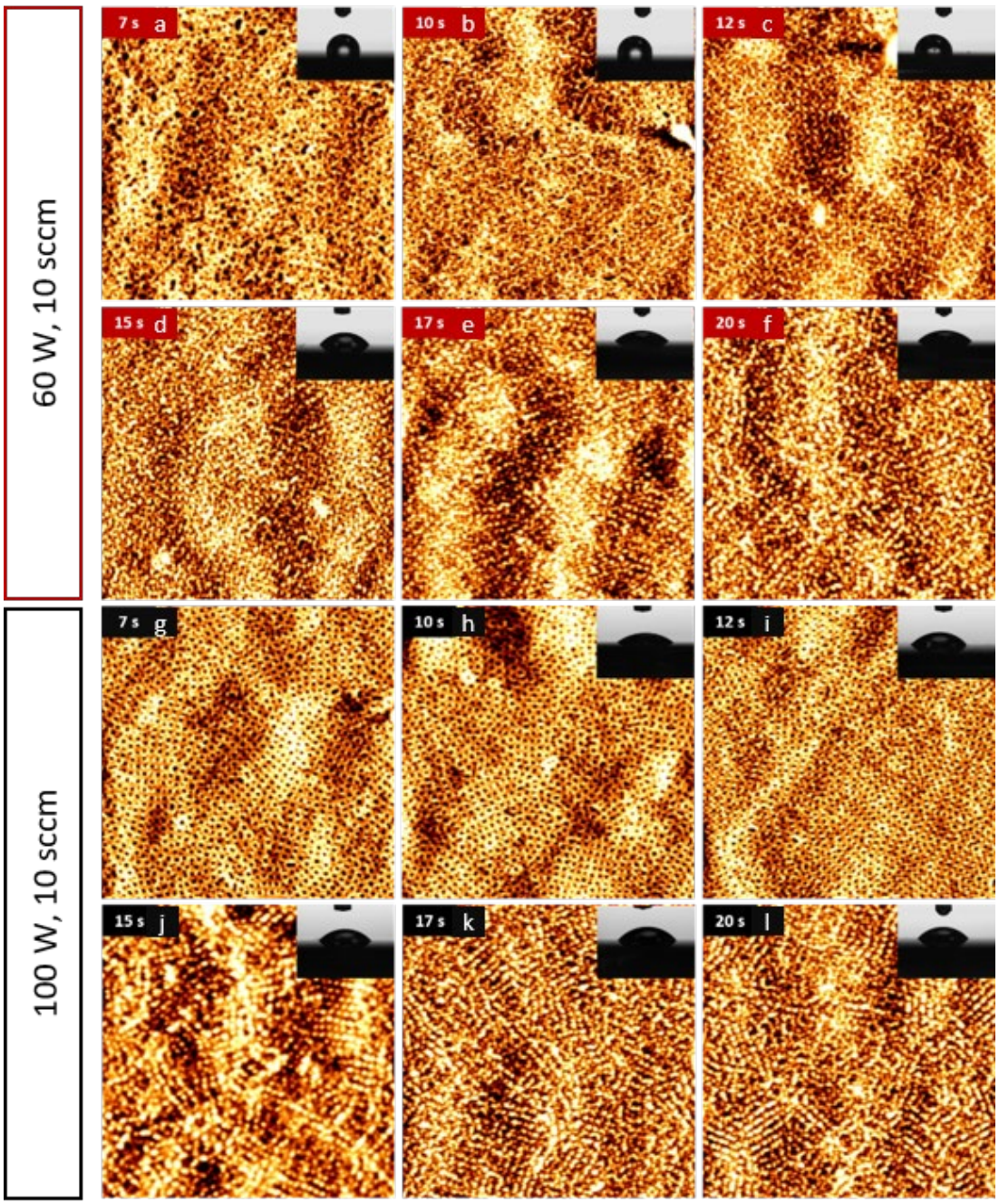

Figure 2-2. Evolution of surface morphology. AFM topographic images of PS-*b*-PEO after exposure to argon plasma using a flow rate of 10 sccm and a RF power of (a-f) 60 W (top, red) and (g-l) 100 W (bottom, black). The inset in each picture shows a drop of water deposited on the surface, used to calculate the water contact angle.

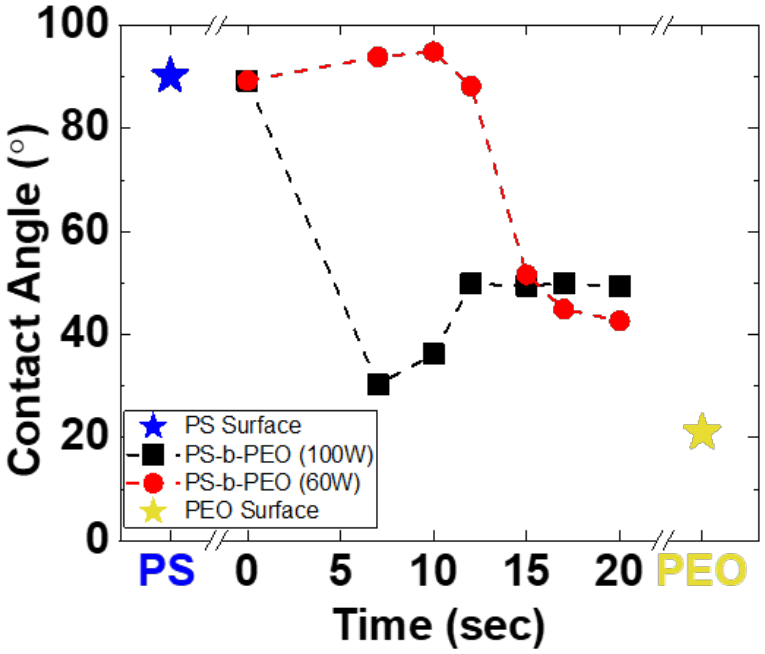

Figure 2-3. Evolution of surface wettability of PS-*b*-PEO thin films after exposure to argon plasma using a flow rate of 10 sccm and a RF power of 60 W and 100 W. The contact angle value for the PS surface was determined experimentally, from a 1 wt% PS solution dissolved in toluene (blue star, left). The contact angle value for PEO was taken from the literature[36] (yellow star, right).

Due to this promising observation of evolution of a micellar to rearranged film structure with perpendicular arrangement of PEO domains to the surface, the plasma power was increased to 100 W while the argon flow and exposure time were kept identical. Results are shown in Figure 2-2 (g-l). At higher RF power, after 7 s of exposure to argon plasma, a drop of WCA from 89° to 30° is observed. Surface morphology, assessed by AFM, show signs of structural rearrangement from the micellar phase to PEO cylinder perpendicular to the surface. Patterns obtained after 10 and 12 s of argon plasma, Figure 2-2 (h-i), exhibit similar perpendicular features obtained after 7 s of exposure to argon plasma with increased contact angle values to 36° and 50° where another plateau is reached. However, as-cast films exposed for more than 12 s do not present vertical cylinder arrangements but rather retain micellar type structures. Additional data obtained with an argon flow rate of 15 sccm and a RF power of 100 W are available in the appendix, Figure S2-4.

From qualitative observations of the AFM topography images and their associated water contact angle, we believe in the structural rearrangement of the micelles into ordered and

disordered structures. Applying a RF power of 60 W is enough to change the surface structure although longer exposure time is needed to observe lower contact angle value suggesting the presence of the hydrophilic PEO block on the surface. Increasing the RF power from 60 to 100 W resulted in a discernible drop of the water contact angle at the beginning of the experiment: we believe the reaction is a balance between structural rearrangement and damage. A gentle process, *i.e.* 60 W, is preferable to overcome the energy barrier leading to reorganisation. Using harsher process, *i.e.* higher RF forward power of 100 W, implies higher rates of bond scission and subsequent cross-linking and damage. Exposing the as-cast films to higher energy is possible for a short period of time. Unfortunately, longer exposure time to argon plasma causes the film to become damaged or cross-linked before the reorganisation process could occur.

Water contact angle values of ~50°, observed after 20 s of exposure to argon plasma in both experiments, are most likely due to the presence PEO and PS block at the surface suggesting the effectiveness of the treatment to rearrange the structure of block-copolymer thin films. This value is midway between the water contact angle value of both pristine PS and PEO. It is worth noticing that argon plasma treatment can also lower the contact angle and has been used in the past to improve surface wettability of few polymers[37-40]. Energetic ion bombardment can create active sites on the polymer surface through C-H and C-C bond scission: those sites can bind to other atoms and molecules, especially oxygen when the surface is thereafter exposed to atmosphere. As such, aforementioned ion bombardment was found to create an amorphous carbon-like damage layer on the surface[41-43]. Due to the mild conditions of our plasma (60 and 100 W, lower than 300+ W) and phase image of Ar plasma treated surfaces, we believe there is little damage to the film surface. Hence, the drop observed with water contact angle is most likely due to the exposure of PEO domains at the surface due to surface reorganisation and little damage. In some cases, Ar plasma treatment may lead to superhydrophobicity when the exposure to plasma is long enough to increase surface roughness[44].

Surface rearrangement could be due to four phenomena: heat gradient between the surface of the film and the substrate when exposed to argon plasma, active reorganisation from energetic ions (although photons could also lead to chain scission in the polymer), coalescence of the micelles and etching of the surface to expose PEO domains. In inert gas plasma, dominant ‘damage’ process is hydrogen abstraction and subsequent

functionalisation (oxygen incorporation) when plasma treated surface is exposed to laboratory atmosphere. However, when oxygen functionalities are present in the polymer backbone, e.g. PEO, etching is observed rather than oxygen incorporation[54]. As for PS, it is well known that the etching is offset by its aromaticity. Further study to determine the possible mechanism behind the surface rearrangement is required.

Compositional Analysis of PS-b-PEO Thin Film Post-Exposure to Argon Plasma.

To assess the chemical nature of the surface, XPS analysis was performed before and after exposure to argon plasma *i.e.* on as-cast film and film exposed to argon plasma for 7 s with an argon flow of 10 sccm and a RF power of 100 W. In order to compensate for charging effect, the adventitious carbon C *1s* binding energy was adjusted to 284.8 eV.

Recorded surface survey indicated the presence of expected elemental signals, C *1s* and O *1s*, as well as a F *1s* peak, Figure 2-4 (a,c) for micellar as-cast film, *i.e.* before plasma treatment. Organic fluorine is commonly observed as a surface contaminant on silicon wafers. The presence of micelles with a PS corona for the as-cast film is supported by the data shown in Figure 2-4 (a,b). The measured C *1s* derived atomic percentage is ~96.2 % while O *1s* suggests an atomic percentage of ~2.4 %. This high C:O atomic ratio is consistent with a carbon overlayer. The small O *1s* feature observed on surface survey is likely adventitious in nature deriving from oxidation of the surface, water or adventitious contamination. C *1s* spectra, Figure 2-4 (b), is dominated by a feature typical of C-C bonds at a binding energy of 284.8 eV consistent with the PS backbone. Curve-fitting reveals a small binding energy feature in the C *1s* spectra assignable to C-O bonds at a binding energy of ~286 eV. This is probably due to surface oxidation or underlying PEO. A feature at 291.5 eV can be assigned to a π-π* satellite peak is further evidence of PS at the surface[45]. However, the atomic percentage of Si *2p* (~ 0.9 %) is believed to be too low to suggest the existence of a monolayer of micelles as their arrangement should expose more silicon substrate, and not cover the entire surface. This data would be more in agreement with the existence of a PS wetting layer on the surface under the micelles. Such a layer would explain the small atomic percentage linked to the Si *2p* peak, as well as the extra thickness observed in Figure 2-1(d).

After exposure to argon plasma, there is dramatic change in the C *1s* spectra envelope. The sample exhibits an increase in both F *1s* and O *1s* peak and a decrease of C *1s*, Figure 2-4

(c-e). The C *1s* spectrum, Figure 2-4 (d), was carried out to analyse the carbon chemical environment. Peaks centred at 284.8 eV and 286.3 eV, already present before argon plasma exposure, are attributed to C-C bonds and C-O bonds[46]. However, C-O bonds contribution is more significant, and its relative intensity (peak area) relative to C-C bonds increased by a factor of 5. Due to the increased presence of fluorine, peaks are observed at 291.9 eV and 294 eV can be attributed to CF_2 and CF_3, with literature values[47-49] of 292 eV and 293.5 eV respectively. Those peaks are attributed to residual gas and the use of fluorine-containing cooling oil during the plasma process. Because of the intensity of CF_2 and CF_3 peaks, the presence of π-π* satellite from the PS block is obscured. It is sometimes assumed the aromatic rings of polystyrene are sensitive to O_2 and N_2 plasma treatment, leading to C=C bond breakage[50]. Other studies have shown that argon plasma can be used to incorporated functionalities on pristine PS, where the incorporation happens at ring sites[51]. UV radiation in an important factor[52] for inert-gas plasmas as the chemical reactions between the plasma and the substrate surface are limited[30]. However, bond scission happens for more reactive plasma treatment (O_2) and for harsher conditions of argon plasma. In 'neutral' and milder plasma, as is the case in this experiment, it has been shown that PS is rather stable as PS can be UV-insensitive[34] and dissipate excess energy by fluorescence[53]. Only photons with energy exceeding covalent bonding (9.2 eV for benzene ring) can lead to bond dissociation[28,54]. Extensive O *1s* spectrum after argon plasma was also recorded, Figure 2-4 (e). It consists of two peaks centred at 532.5 eV and 536.7 eV attributed to organic C-O and O-F_x which is consistent with the XPS spectra[55] of PEO and with the presence of fluorine on the surface. Thus, these data suggest that PEO is being exposed following mild plasma treatments and consistent with a surface rearrangement to the vertical cylinder structure.

Although the block copolymer was spin-coated onto the silicon substrate, no peaks were observed for Si *2p* (both elemental and oxide state). We can only conclude on the excellent coverage of the block copolymer film with enough thickness and without any dewetted and/or delaminated areas. XPS data in conjunction with water contact angle values and AFM images clearly shows an evolution of the surface structure and composition from micelle with PS-corona to exposed PEO cylinder in a PS matrix in a $C_{\perp}$ arrangement.

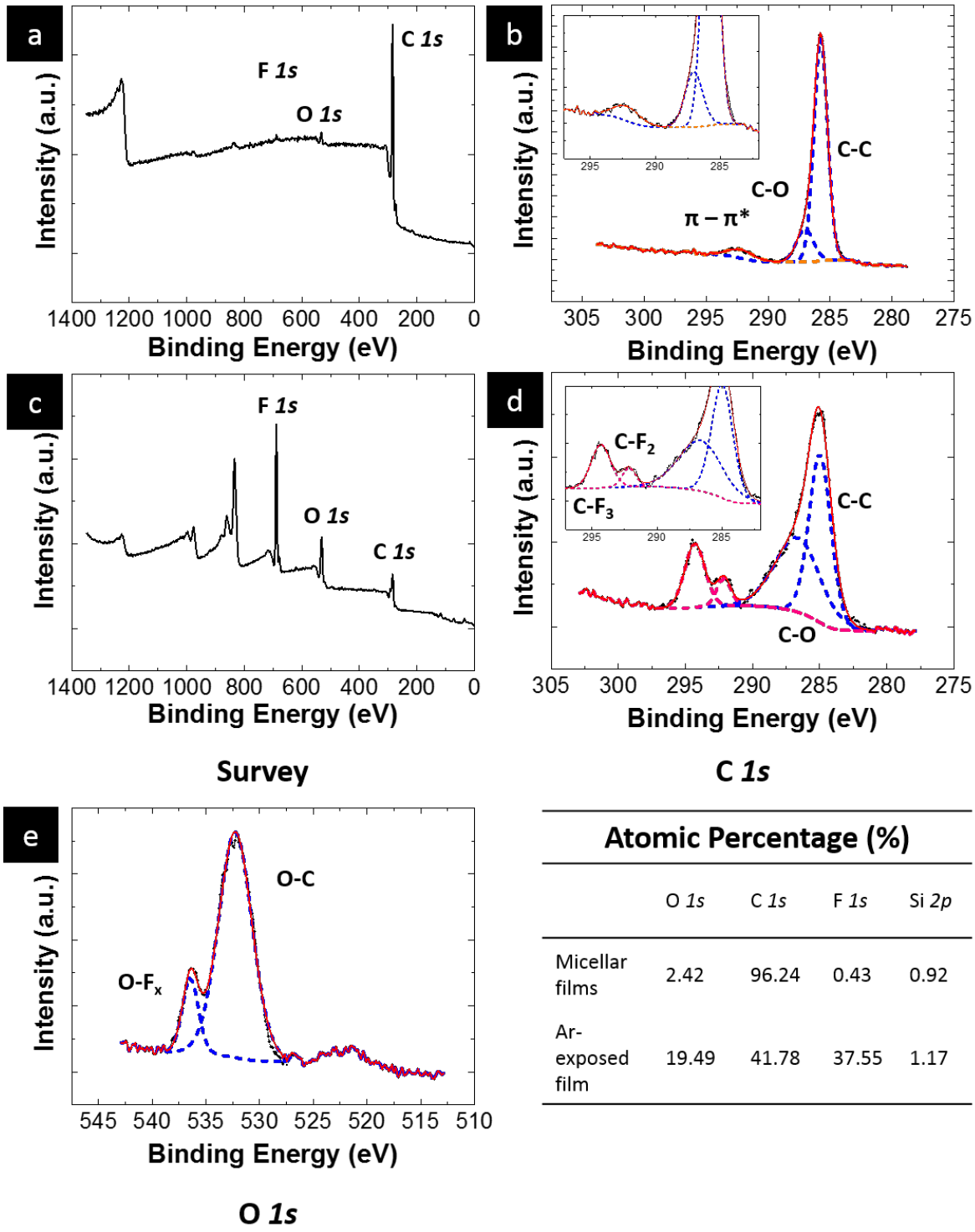

Atomic Percentage (%)				
	O *1s*	C *1s*	F *1s*	Si *2p*
Micellar films	2.42	96.24	0.43	0.92
Ar-exposed film	19.49	41.78	37.55	1.17

Figure 2-4. Evolution of the film composition by XPS. (a-b) Survey and core C *1s* spectra of micellar as-cast film. (c-e) Survey, C *1s* and O *1s* spectra of micellar thin film exposed to argon plasma for 7 s, with an argon flow of 10 sccm and a RF power of 100 W. Evolution of the atomic percentage for the elements is recorded in the table.

Large-scale Microphase Separation and Etching Phenomenon Analysis.

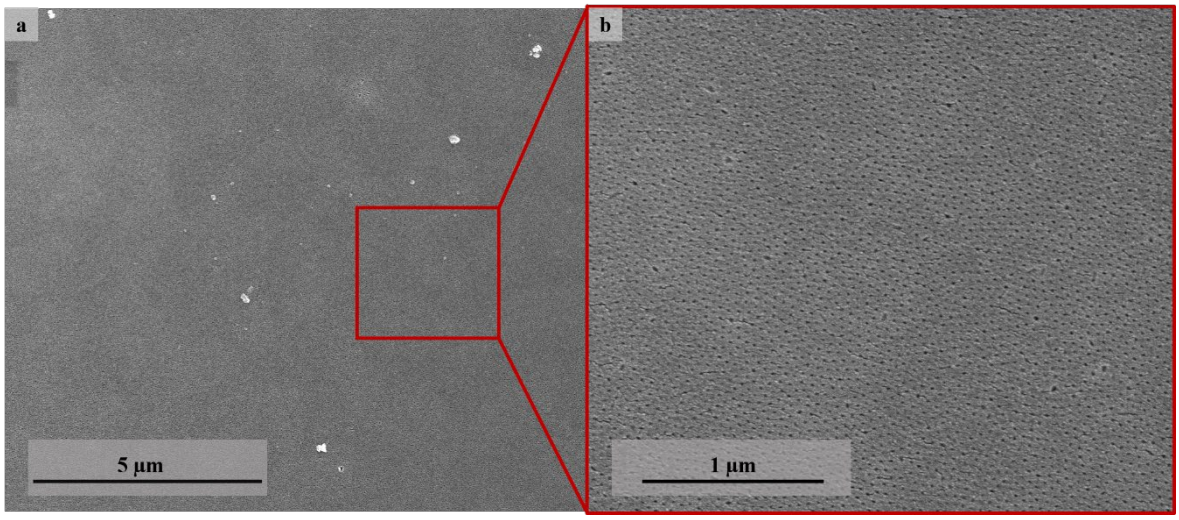

Figure 2-5. Large scale reorganisation of the BCP thin film. Top-down SEM images of sample exposed to argon plasma for 12 s, with an argon flow of 10 sccm and a RF power of 100 W.

The plasma driven surface reorganisation is not a local event and happens across the entire surface as seen in Figure 2-5. Further evidence is available in the appendix, Figure S2-5. Noticeably, little damage or delamination of the polymer film is observed. Small lines and/or cracks on the SEM images recorded are associated with the presence of a gold layer, sputtered on the surface to reduce the charging effect of the block copolymer film. If extensive damage occurred, this would be expected to be obvious in these large-scale images. Surface wrinkling is a common phenomenon observed on argon plasma-treated samples when the top-layer is modified by Ar^+ ion bombardment. Roughening of the surface of a polymer during plasma etching is a result of buckling instability: a large difference in elastic modulus between stiff plasma-induced (amorphous, carbon-like damage) and polymer layer can cause micron-scale wrinkling when exposed to compressive stress[56-60]. Lack of surface roughness and microscale wrinkles suggest there is little modification of both chemistry and modulus of our block-copolymer surface to drive the buckling instability. Plasma filtered treatment can also yield ultra-low to no damage (roughness, wrinkling) by reducing ion bombardment and surface modification by VUV-UV[61-63].

Although we cannot exclude the presence of a small modified amorphous layer on the surface, we suggest that all the data shown is consistent with structural reorganisation of block copolymer thin film from the initial micellar arrangement. Short exposure and mild

conditions could be enough to drive the phase separation, while limiting surface damage and roughness.

To rule out possible etching of the films during argon plasma treatment, we followed the evolution of the thickness for films exposed to the following conditions: RF power of 100 W, exposure from 3 s to 10 s. The argon flow rate was increased to 15 sccm to increase the effect of Ar^+ ion bombardment on the surface, and hence damage layer and/or etching phenomena as shown in Figure 2-1 (d). Measured thickness after 3 s, 5 s, 7 s and 10 s of exposure to argon plasma were measured to be 48.2 (± 1.7), 46.7 (± 1.3), 46.8 (± 1.2) and 47.1 (± 1.2) nm respectively. Those values were obtained using a spectroscopy ellipsometer and they were consistent with experimental error and uncertainties to enable us to conclude there is insignificant etch happening. If any significant removal of material is occurring, it is probably within the top 2 nm of the film since this is difficult to quantify. Furthermore, the ellipsometry measurements reinforced the idea of the absence of an amorphous damage carbon-like layer. The two-layer model (SiO_2 + PS-*b*-PEO) we used to simulate experimental data model fitted perfectly without having to include an extra modified carbon-like layer.

2.5. Conclusions

Overall, our results demonstrate an alternative and effective approach to induce surface reorganisation from spun-cast micellar thin films on a large scale using a mild argon plasma treatment. This simple process enables the formation of vertical and parallel cylinders domain alike after few seconds of treatment. Inert argon gas was chosen to minimise chemical reaction between the surface of the thin film and the plasma, while maximising physical interaction by bombarding the sample with Ar^+ ions. Samples treated with low RF power (60W compared to 100W) and flow rate (10 sccm compared to 15 sccm) present characteristics of microphase separated films, as assessed by topographic AFM and evolution of chemical composition. We believe the energy provided by the argon plasma is sufficient to overcome the energy barrier to drive surface rearrangement, and structural reorganisation. On the contrary, samples treated with harsher conditions tend to yield rough surface and lack visible short- and long-range order for longer exposure time to argon plasma. A plausible cause would be that exposure to argon plasma in higher Ar^+ ion bombardment regime causes the film to become damage or cross-linked before any chance of reorganisation. Phase-separation using a plasma approach appears to be a balance

between reorganisation and damage. Damage could be further minimised by using a filtered plasma by reducing ion bombardment and surface modification by VUV-UV.

2.6. References

(1) Khan, H. N.; Hounshell, D. A.; Fuchs, E. R. H. Science and Research Policy at the End of Moore's Law. *Nat. Electron.* **2018**, No. 1, 14–21.

(2) Kwak, J.; Mishra, A. K.; Lee, J.; Lee, K. S.; Choi, C.; Maiti, S.; Kim, M.; Kim, J. K. Fabrication of Sub-3 Nm Feature Size Based on Block Copolymer Self-Assembly for Next-Generation Nanolithography. *Macromolecules* **2017**, *50* (17), 6813–6818. https://doi.org/10.1021/acs.macromol.7b00945.

(3) Arias-Zapata, J.; Garnier, J. D.; Mehedi, H.; Legrain, A.; Salem, B.; Cunge, G.; Zelsmann, M. Engineering Self-Assembly of a High-χ Block Copolymer for Large-Area Fabrication of Transistors Based on Functional Graphene Nanoribbon Arrays. *Chem. Mater.* **2019**, *31* (9), 3154–3162. https://doi.org/10.1021/acs.chemmater.8b04936.

(4) Li, T.; Wang, Z.; Schulte, L.; Hansen, O.; Ndoni, S. Fast & Scalable Pattern Transfer via Block Copolymer Nanolithography. *RSC Adv.* **2015**, No. 5, 102619. https://doi.org/10.1039/c5ra21188c.

(5) Hu, H.; Gopinadhan, M.; O. Osuji, C. Directed Self-Assembly of Block Copolymers: A Tutorial Review of Strategies for Enabling Nanotechnology with Soft Matter. *Soft Matter* **2014**, *10* (22), 3867–3889. https://doi.org/10.1039/C3SM52607K.

(6) Segalman, R. A. Patterning with Block Copolymer Thin Films. *Materials Science and Engineering: R: Reports* **2005**, *48* (6), 191–226. https://doi.org/10.1016/j.mser.2004.12.003.

(7) Darling, S. B. Directing the Self-Assembly of Block Copolymers. *Progress in Polymer Science* **2007**, *32* (10), 1152–1204. https://doi.org/10.1016/j.progpolymsci.2007.05.004.

(8) Yang, G.-W.; Wu, G.-P.; Chen, X.; Xiong, S.; Arges, C. G.; Ji, S.; Nealey, P. F.; Lu, X.-B.; Darensbourg, D. J.; Xu, Z.-K. Directed Self-Assembly of Polystyrene-b-Poly(Propylene Carbonate) on Chemical Patterns via Thermal Annealing for Next Generation Lithography. *Nano Lett.* **2017**, *17* (2), 1233–1239. https://doi.org/10.1021/acs.nanolett.6b05059.

(9) Welander, A. M.; Kang, H.; Stuen, K. O.; Solak, H. H.; Müller, M.; de Pablo, J. J.; Nealey, P. F. Rapid Directed Assembly of Block Copolymer Films at Elevated Temperatures. *Macromolecules* **2008**, *41* (8), 2759–2761. https://doi.org/10.1021/ma800056s.

(10) Perego, M.; Lupi, F. F.; Ceresoli, M.; Giammaria, T. J.; Seguini, G.; Enrico, E.; Boarino, L.; Antonioli, D.; Gianotti, V.; Sparnacci, K.; et al. Ordering Dynamics in Symmetric PS-b-PMMA Diblock Copolymer Thin Films during Rapid Thermal Processing. *J. Mater. Chem. C* **2014**, *2* (32), 6655–6664. https://doi.org/10.1039/C4TC00756E.

(11) Pang, Y.; Jin, X.; Huang, G.; Wan, L.; Ji, S. Directed Self-Assembly of Styrene-Methyl Acrylate Block Copolymers with Sub-7 Nm Features via Thermal Annealing. *Macromolecules* **2019**, *52* (8), 2987–2994. https://doi.org/10.1021/acs.macromol.9b00174.

(12) Sinturel, C.; Vayer, M.; Morris, M.; Hillmyer, M. A. Solvent Vapor Annealing of Block Polymer Thin Films. *Macromolecules* **2013**, *46* (14), 5399–5415. https://doi.org/10.1021/ma400735a.

(13) Cummins, C.; Kelly, R. A.; Gangnaik, A.; Georgiev, Y. M.; Petkov, N.; Holmes, J. D.; Morris, M. A. Solvent Vapor Annealing of Block Copolymers in Confined Topographies: Commensurability Considerations for Nanolithography. *Macromolecular Rapid Communications* **2015**, *36* (8), 762–767. https://doi.org/10.1002/marc.201400722.

(14) Gu, X.; Gunkel, I.; Hexemer, A.; Russell, T. P. Controlling Domain Spacing and Grain Size in Cylindrical Block Copolymer Thin Films by Means of Thermal and Solvent Vapor Annealing. *Macromolecules* **2016**, *49* (9), 3373–3381. https://doi.org/10.1021/acs.macromol.6b00429.

(15) Jiang, J.; Jacobs, A. G.; Wenning, B.; Liedel, C.; Thompson, M. O.; Ober, C. K. Ultrafast Self-Assembly of Sub-10 Nm Block Copolymer Nanostructures by Solvent-Free High-Temperature Laser Annealing. *ACS Appl. Mater. Interfaces* **2017**, *9* (37), 31317–31324. https://doi.org/10.1021/acsami.7b00774.

(16) Son, J. G.; Gotrik, K. W.; Ross, C. A. High-Aspect-Ratio Perpendicular Orientation of PS-*b*-PDMS Thin Films under Solvent Annealing. *ACS Macro Lett.* **2012**, *1* (11), 1279–1284. https://doi.org/10.1021/mz300475g.

(17) Olszowka, V.; Hund, M.; Kuntermann, V.; Scherdel, S.; Tsarkova, L.; Böker, A. Electric Field Alignment of a Block Copolymer Nanopattern: Direct Observation of the Microscopic Mechanism. *ACS Nano* **2009**, *3* (5), 1091–1096. https://doi.org/10.1021/nn900081u.

(18) Osuji, C.; Zhang, Y.; Mao, G.; Ober, C. K.; Thomas, E. L. Transverse Cylindrical Microdomain Orientation in an LC Diblock Copolymer under Oscillatory Shear. *Macromolecules* **1999**, *32* (22), 7703–7706. https://doi.org/10.1021/ma991155y.

(19) Hamley, I. W.; Hamley, I. W. *The Physics of Block Copolymers*; Oxford: Oxford University Press, 1998.

(20) Sparnacci, K.; Antonioli, D.; Gianotti, V.; Laus, M.; Ferrarese Lupi, F.; Giammaria, T. J.; Seguini, G.; Perego, M. Ultrathin Random Copolymer-Grafted Layers for Block Copolymer Self-Assembly. *ACS Appl. Mater. Interfaces* **2015**, *7* (20), 10944–10951. https://doi.org/10.1021/acsami.5b02201.

(21) Lupi, F. F.; Giammaria, T. J.; Seguini, G.; Ceresoli, M.; Perego, M.; Antonioli, D.; Gianotti, V.; Sparnacci, K.; Laus, M. Flash Grafting of Functional Random Copolymers for Surface Neutralization. *J. Mater. Chem. C* **2014**, *2* (25), 4909–4917. https://doi.org/10.1039/C4TC00328D.

(22) Son, J. G.; Bulliard, X.; Kang, H.; Nealey, P. F.; Char, K. Surfactant-Assisted Orientation of Thin Diblock Copolymer Films. *Advanced Materials* **2008**, *20* (19), 3643–3648. https://doi.org/10.1002/adma.200800670.

(23) Sunday, D. F.; Maher, M. J.; Tein, S.; Carlson, M. C.; Ellison, C. J.; Willson, C. G.; Kline, R. J. Quantifying the Interface Energy of Block Copolymer Top Coats. *ACS Macro Lett.* **2016**, *5* (12), 1306–1311. https://doi.org/10.1021/acsmacrolett.6b00684.

(24) Kim, E.; Kim, W.; Lee, K. H.; Ross, C. A.; Son, J. G. A Top Coat with Solvent Annealing Enables Perpendicular Orientation of Sub-10 Nm Microdomains in Si-Containing Block Copolymer Thin Films. *Advanced Functional Materials* **2014**, *24* (44), 6981–6988. https://doi.org/10.1002/adfm.201401678.

(25) Suh, H. S.; Kim, D. H.; Moni, P.; Xiong, S.; Ocola, L. E.; Zaluzec, N. J.; Gleason, K. K.; Nealey, P. F. Sub-10-Nm Patterning via Directed Self-Assembly of Block Copolymer Films with a Vapour-Phase Deposited Topcoat. *Nature Nanotechnology* **2017**, *12* (6), 575–581. https://doi.org/10.1038/nnano.2017.34.

(26) Lu, K.-Y.; Lo, T.-Y.; Georgopanos, P.; Avgeropoulos, A.; Shi, A.-C.; Ho, R.-M. Orienting Silicon-Containing Block Copolymer Films with Perpendicular Cylinders via Entropy and Surface Plasma Treatment. *Macromolecules* **2017**, *50* (23), 9403–9410. https://doi.org/10.1021/acs.macromol.7b02218.

(27) Oh, J.; Suh, H. S.; Ko, Y.; Nah, Y.; Lee, J.-C.; Yeom, B.; Char, K.; Ross, C. A.; Son, J. G. Universal Perpendicular Orientation of Block Copolymer Microdomains Using a Filtered Plasma. *Nat Commun* **2019**, *10* (1), 1–8. https://doi.org/10.1038/s41467-019-10907-5.

(28) Yakut, S.; Ulutas, K.; Deger, D. Plasma Discharge Power Dependent AC Conductivity of Plasma Poly(Ethylene Oxide) Thin Films. *Thin Solid Films* **2018**, *645*, 269–277. https://doi.org/10.1016/j.tsf.2017.10.048.

(29) Choukourov, A.; Gordeev, I.; Ponti, J.; Uboldi, C.; Melnichuk, I.; Vaidulych, M.; Kousal, J.; Nikitin, D.; Hanyková, L.; Krakovský, I.; et al. Microphase-Separated PE/PEO Thin Films Prepared by Plasma-Assisted Vapor Phase Deposition. *ACS Appl. Mater. Interfaces* **2016**, *8* (12), 8201–8212. https://doi.org/10.1021/acsami.5b12382.

(30) Tajima, S.; Komvopoulos, K. Effect of Reactive Species on Surface Crosslinking of Plasma-Treated Polymers Investigated by Surface Force Microscopy. *Appl. Phys. Lett.* **2006**, *89* (12), 124102. https://doi.org/10.1063/1.2338635.

(31) Hansen, C. M. *Hansen Solubility Parameters: A User's Handbook, Second Edition*; CRC Press, 2007.

(32) Starý, Z. Thermodynamics and Morphology and Compatibilization of Polymer Blends. In *Characterization of Polymer Blends*; John Wiley & Sons, Ltd, 2014; pp 93–132. https://doi.org/10.1002/9783527645602.ch03.

(33) Giraud, E. C.; Mokarian-Tabari, P.; Toolan, D. T. W.; Arnold, T.; Smith, A. J.; Howse, J. R.; Topham, P. D.; Morris, M. A. Highly Ordered Titanium Dioxide Nanostructures via a Simple One-Step Vapor-Inclusion Method in Block Copolymer Films. *ACS Appl. Nano Mater.* **2018**, *1* (7), 3426–3434. https://doi.org/10.1021/acsanm.8b00632.

(34) Bruce, R. L.; Weilnboeck, F.; Lin, T.; Phaneuf, R. J.; Oehrlein, G. S.; Long, B. K.; Willson, C. G.; Vegh, J. J.; Nest, D.; Graves, D. B. Relationship between Nanoscale Roughness and Ion-Damaged Layer in Argon Plasma Exposed Polystyrene Films. *Journal of Applied Physics* **2010**, *107* (8), 084310. https://doi.org/10.1063/1.3373587.

(35) Wilken, R.; Holländer, A.; Behnisch, J. Vacuum Ultraviolet Photolysis of Polyethylene, Polypropylene, and Polystyrene. *Plasmas and Polymers* **2002**, *7* (2), 185–205. https://doi.org/10.1023/A:1016247524912.

(36) Wu, H.; Huang, X. Structural Evolution of Low-Molecular-Weight Poly(Ethylene Oxide)-Block-Polystyrene Diblock Copolymer Thin Film. *The Scientific World Journal* **2013**, 1–7. https://doi.org/10.1155/2013/539457.

(37) Guruvenket, S.; Rao, G. M.; Komath, M.; Raichur, A. M. Plasma Surface Modification of Polystyrene and Polyethylene. *Applied Surface Science* **2004**, *236* (1), 278–284. https://doi.org/10.1016/j.apsusc.2004.04.033.

(38) De Geyter, N.; Morent, R.; Leys, C.; Gengembre, L.; Payen, E. Treatment of Polymer Films with a Dielectric Barrier Discharge in Air, Helium and Argon at Medium Pressure. *Surface and Coatings Technology* **2007**, *201* (16), 7066–7075. https://doi.org/10.1016/j.surfcoat.2007.01.008.

(39) Lai, J.; Sunderland, B.; Xue, J.; Yan, S.; Zhao, W.; Folkard, M.; Michael, B. D.; Wang, Y. Study on Hydrophilicity of Polymer Surfaces Improved by Plasma Treatment. *Applied Surface Science* **2006**, *252* (10), 3375–3379. https://doi.org/10.1016/j.apsusc.2005.05.038.

(40) Duca, M. D.; Plosceanu, C. L.; Pop, T. Surface Modifications of Polyvinylidene Fluoride (PVDF) under Rf Ar Plasma. *Polymer Degradation and Stability* **1998**, *61* (1), 65–72. https://doi.org/10.1016/S0141-3910(97)00130-4.

(41) Bruce, R. L.; Engelmann, S.; Lin, T.; Kwon, T.; Phaneuf, R. J.; Oehrlein, G. S.; Long, B. K.; Willson, C. G.; Végh, J. J.; Nest, D.; et al. Study of Ion and Vacuum Ultraviolet-Induced Effects on Styrene- and Ester-Based Polymers Exposed to Argon Plasma. *Journal of Vacuum Science & Technology B: Microelectronics and Nanometer Structures Processing, Measurement, and Phenomena* **2009**, *27* (3), 1142–1155. https://doi.org/10.1116/1.3136864.

(42) Végh, J. J.; Nest, D.; Graves, D. B.; Bruce, R.; Engelmann, S.; Kwon, T.; Phaneuf, R. J.; Oehrlein, G. S.; Long, B. K.; Willson, C. G. Near-Surface Modification of Polystyrene by Ar+: Molecular Dynamics Simulations and Experimental Validation. Appl. Phys. Lett. 2007, 91 (23), 233113. https://doi.org/10.1063/1.2821226.

(43) Végh, J. J.; Nest, D.; Graves, D. B.; Bruce, R.; Engelmann, S.; Kwon, T.; Phaneuf, R. J.; Oehrlein, G. S.; Long, B. K.; Willson, C. G. Molecular Dynamics Simulations of Near-Surface

Modification of Polystyrene: Bombardment with Ar+ and Ar+/Radical Chemistries. *Journal of Applied Physics* **2008**, *104* (3), 034308. https://doi.org/10.1063/1.2963708.

(44) Nokes, J. M.; Sharma, H.; Tu, R.; Kim, M. Y.; Chu, M.; Siddiqui, A.; Khine, M. Nanotextured Shrink Wrap Superhydrophobic Surfaces by Argon Plasma Etching. *Materials* **2016**, *9* (3), 196. https://doi.org/10.3390/ma9030196.

(45) Tardio, S.; Abel, M.-L.; Carr, R. H.; Watts, J. F. Polystyrene-silicon Bonding through π Electrons: A Combined XPS and DFT Study - Tardio - 2016 - Surface and Interface Analysis - Wiley Online Library. *Surf. Interface Anal.* **2016**, No. 48, 556–560. https://doi.org/10.1002/sia.5879.

(46) Louette, P.; Bodino, F.; Pireaux, J.-J. Poly(Ethylene Oxide) (PEO) XPS Reference Core Level and Energy Loss Spectra. *Surface Science Spectra* **2005**, *12* (1), 59–63. https://doi.org/10.1116/11.20050912.

(47) Schulze, M.; Bolwin, K.; Gülzow, E.; Schnurnberger, W. XPS Analysis of PTFE Decomposition Due to Ionizing Radiation. *Fresenius J Anal Chem* **1995**, *353* (5–8), 778–784. https://doi.org/10.1007/BF00321370.

(48) Vandencasteele, N.; Reniers, F. Plasma-Modified Polymer Surfaces: Characterization Using XPS. *Journal of Electron Spectroscopy and Related Phenomena* **2010**, *178–179*, 394–408. https://doi.org/10.1016/j.elspec.2009.12.003.

(49) Friedrich, J.; Kühn, G.; Jansen, K.; Möller, B.; Fischer, S. Fluorination of Polymer Surfaces. *Vakuum in Forschung und Praxis 14* (5), 285–290.

(50) Ba, O. M.; Marmey, P.; Anselme, K.; Duncan, A. C.; Ponche, A. Surface Composition XPS Analysis of a Plasma Treated Polystyrene: Evolution over Long Storage Periods. *Colloids and Surfaces B: Biointerfaces* **2016**, *145*, 1–7. https://doi.org/10.1016/j.colsurfb.2016.04.026.

(51) France, R. M.; Short, R. D. Plasma Treatment of Polymers: The Effects of Energy Transfer from an Argon Plasma on the Surface Chemistry of Polystyrene, and Polypropylene. A High-Energy Resolution X-Ray Photoelectron Spectroscopy Study. *Langmuir* **1998**, *14* (17), 4827–4835. https://doi.org/10.1021/la9713053.

(52) Poncin-Epaillard, F.; Vallon, S.; Drévillon, B. Illustration of Surface Crosslinking of Different Polymers Treated in Argon Plasma. *Macromolecular Chemistry and Physics* **1997**, *198* (8), 2439–2456. https://doi.org/10.1002/macp.1997.021980807.

(53) Truica-Marasescu, F.-E.; Wertheimer, M. R. Vacuum Ultraviolet Photolysis of Hydrocarbon Polymers. *Macromolecular Chemistry and Physics* **2005**, *206* (7), 744–757. https://doi.org/10.1002/macp.200400510.

(54) Wilken, R.; Holländer, A.; Behnisch, J. Surface Radical Analysis on Plasma-Treated Polymers. *Surface and Coatings Technology* **1999**, *116–119*, 991–995. https://doi.org/10.1016/S0257-8972(99)00282-0.

(55) Louette, P.; Bodino, F.; Pireaux, J.-J. Poly(Styrene) XPS Reference Core Level and Energy Loss Spectra. *Surface Science Spectra* **2005**, *12* (1), 96–99. https://doi.org/10.1116/11.20050920.

(56) Lin, T.-C.; Bruce, R. L.; Oehrlein, G. S.; Phaneuf, R. J.; Kan, H.-C. Direct and Quantitative Evidence for Buckling Instability as a Mechanism for Roughening of Polymer during Plasma Etching. *Appl. Phys. Lett.* **2012**, *100* (23), 233113. https://doi.org/10.1063/1.4718940.

(57) Oehrlein, G. S.; Phaneuf, R. J.; Graves, D. B. Plasma-Polymer Interactions: A Review of Progress in Understanding Polymer Resist Mask Durability during Plasma Etching for Nanoscale Fabrication. *Journal of Vacuum Science & Technology B* **2011**, *29* (1), 010801. https://doi.org/10.1116/1.3532949.

(58) Corbella, C.; Pranda, A.; Portal, S.; Arcos, T. de los; Grundmeier, G.; Oehrlein, G. S.; Keudell, A. von. Validation of Etching Model of Polypropylene Layers Exposed to Argon Plasmas. *Plasma Processes and Polymers* **2019**, *16* (6), 1900019. https://doi.org/10.1002/ppap.201900019.

(59) Nest, D.; Chung, T.-Y.; Graves, D. B.; Engelmann, S.; Bruce, R. L.; Weilnboeck, F.; Oehrlein, G. S.; Wang, D.; Andes, C.; Hudson, E. A. Understanding the Roughening and Degradation of 193 Nm Photoresist during Plasma Processing: Synergistic Roles of Vacuum Ultraviolet Radiation and Ion Bombardment. *Plasma Processes and Polymers* **2009**, *6* (10), 649–657. https://doi.org/10.1002/ppap.200900039.

(60) Nest, D.; Graves, D. B.; Engelmann, S.; Bruce, R. L.; Weilnboeck, F.; Oehrlein, G. S.; Andes, C.; Hudson, E. A. Synergistic Effects of Vacuum Ultraviolet Radiation, Ion Bombardment, and Heating in 193nm Photoresist Roughening and Degradation. *Appl. Phys. Lett.* **2008**, *92* (15), 153113. https://doi.org/10.1063/1.2912028.

(61) Wu, C.; Wang, J.; Zhang, W.; Luo, Y. Modeling and Simulation of Ion-Filtered Inductively Coupled Plasma Using Argon Plasma. *Jpn. J. Appl. Phys.* **2015**, *54* (3), 036101. https://doi.org/10.7567/JJAP.54.036101.

(62) Huang, C.-H.; Su, C.-Y.; Lai, C.-S.; Li, Y.-C.; Samukawa, S. Ultra-Low-Damage Radical Treatment for the Highly Controllable Oxidation of Large-Scale Graphene Sheets. *Carbon* **2014**, *73*, 244–251. https://doi.org/10.1016/j.carbon.2014.02.060.

(63) Clouet, F.; Shi, M. K. Interactions of Polymer Model Surfaces with Cold Plasmas: Hexatriacontane as a Model Molecule of High-Density Polyethylene and Octadecyl Octadecanoate as a Model of Polyester. I. Degradation Rate versus Time and Power. *Journal of Applied Polymer Science* **1992**, *46* (11), 1955–1966. https://doi.org/10.1002/app.1992.070461108.

2.7. Appendix

Application of argon plasma treatment to worm-like micelles obtained after spin-coating of a turbid solution of PS-*b*-PEO 32K-*b*-11K yielding parallel arrangement of PEO domains to the surface: Figure S2-1, Figure S2-2, Figure S2-3.

Figure S2-1 shows the application of an argon plasma treatment to worm-like micelles and the subsequent evolution of surface morphology. Experimental conditions were 15 s exposure to argon plasma, with a RF power of 100 W and a flow rate of 10 sccm. Wormlike micelles from Figure S2-1 (a) become more defined with the treatment, with the formation of continuous lines as presented in Figure S2-1 (b). Pitch size is ~ 33.2 nm, as determined in Figure S2-1 (c).

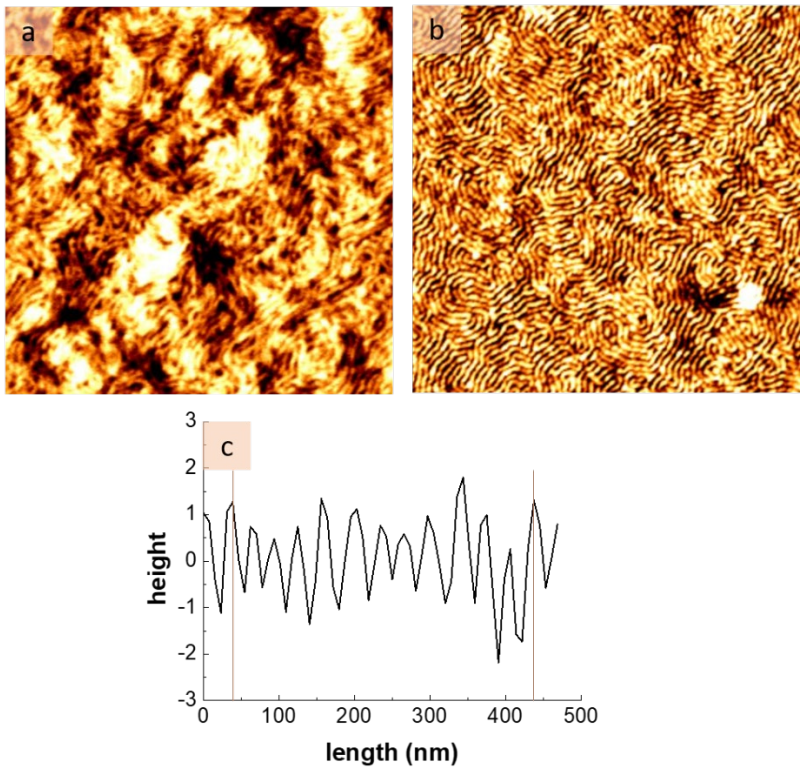

Figure S2-1. Morphology differences of PS-b-PEO thin film. Tapping mode AFM of (a) as-cast thin film and (b) argon plasma treated thin film. (c) Line profile of plasma treated sample.

As for the spherical micelles, wormlike micelles were exposed to argon plasma. Because of preliminary data on spherical micelles (Figure 2-2), we decided to keep the argon flow rate at 10 sccm and to study the effect of two applied RF forward powers: 60 W and 100 W.

Surface morphologies were assessed by AFM after 5 to 12 s argon plasma. Evolution of the morphologies is presented in Figure S2-2. Gentle 60 W forward power, Figure S2-2 (b-e), leads to nanowires with better definition.

Top-down and angled SEM were performed on a sample exposed to 60 W for 10 s under a flow rate of 10 sccm, Figure S2-3, to confirm the absence of any dewetted area and/or possible unequal etching of the surface. Corresponding AFM images is available is Figure S2-2 (d).

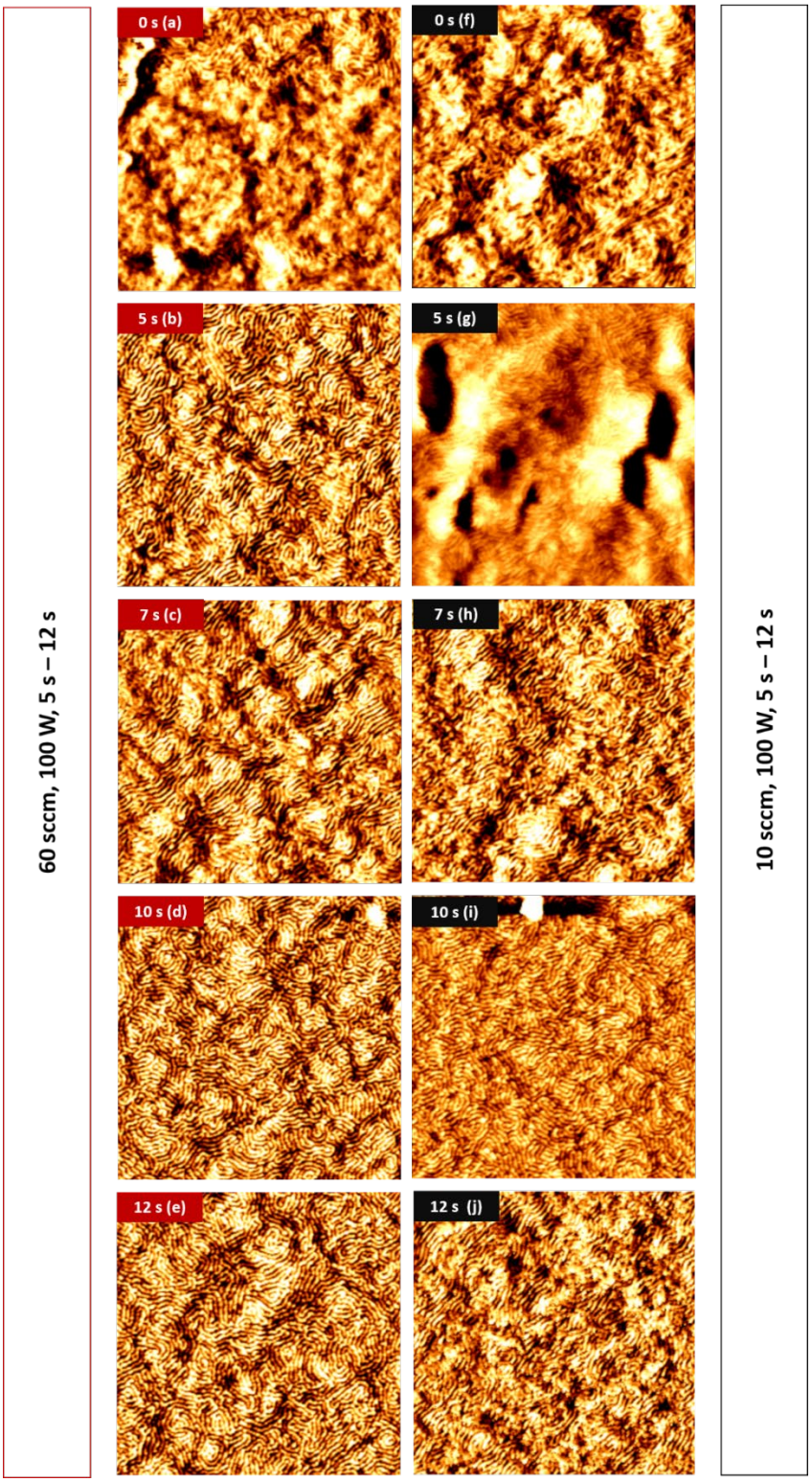

Figure S2-2. Evolution of surface morphology of wormlike micelles. AFM topographic images of PS-*b*-PEO after exposure to plasma using a flow rate of 10 sccm and a RF power of 60 W (red, a-e) and 100 W (black, f-j).

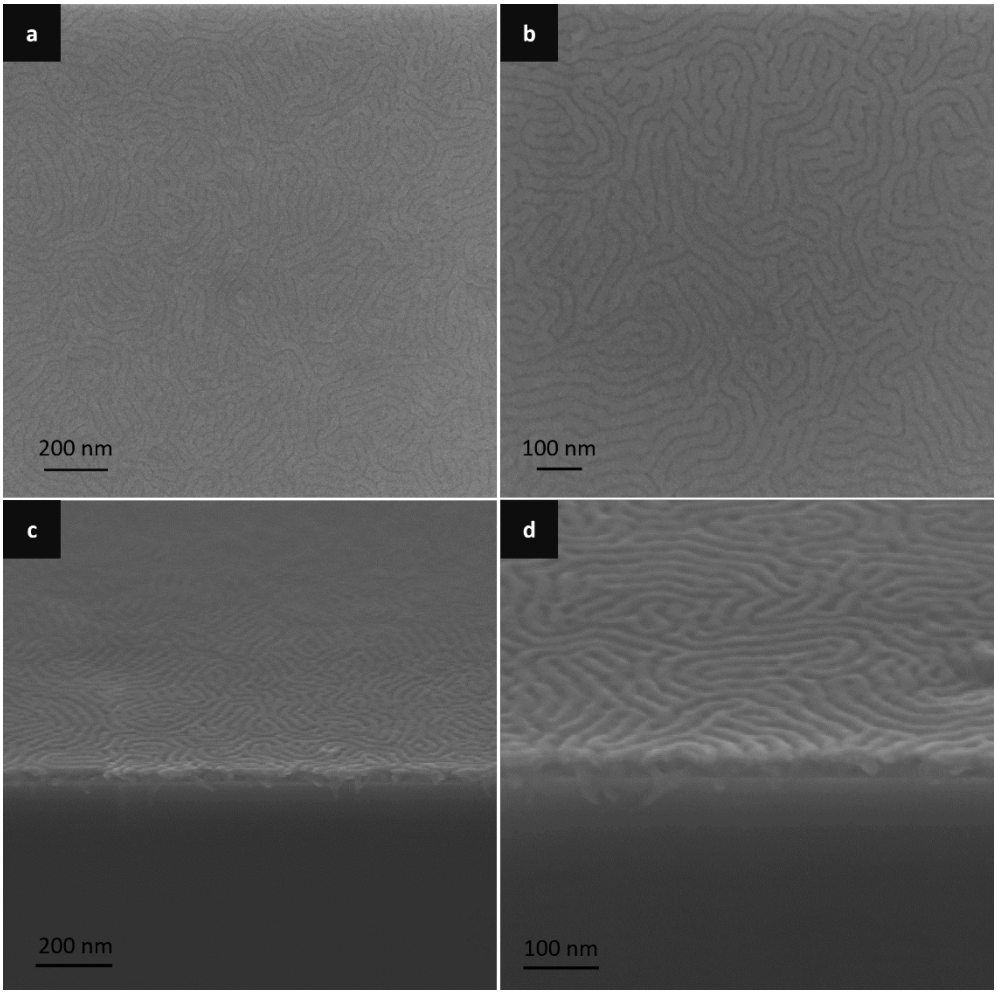

Figure S2-3. (a), (b) top-down SEM and (c), (d) angled SEM at 20° of wormlike micellar film exposed to argon plasma for 10 s with a flow rate of 10 sccm and a RF power of 60 W.

Evolution of surface morphology and wettability of micellar PS-*b*-PEO (42K-*b*-11.5K) after exposure to argon plasma at 100 W with a higher flow rate of 15 sccm: Figure S2-4. We decided to compare the influence of the flow rate on the surface structural evolution by increasing it from 10 sccm to 15 sccm, under a RF power of 100 W. Similar trend, comparable to Figure 2-2 (g-l), is observed with a drop in the contact angle value from ~ 89° to ~ 40°. Although the surface recovers parts of its hydrophobic nature with plateau at ~60°, this recovery is most likely due to the presence of cross-linked and amorphous layer on the surface. Topographic images, Figure S2-4 (a-d), show no evidence of a self-assembly. We believe Ar^+ ion bombardment causes increased surface damage, as a superior flow rate is used.

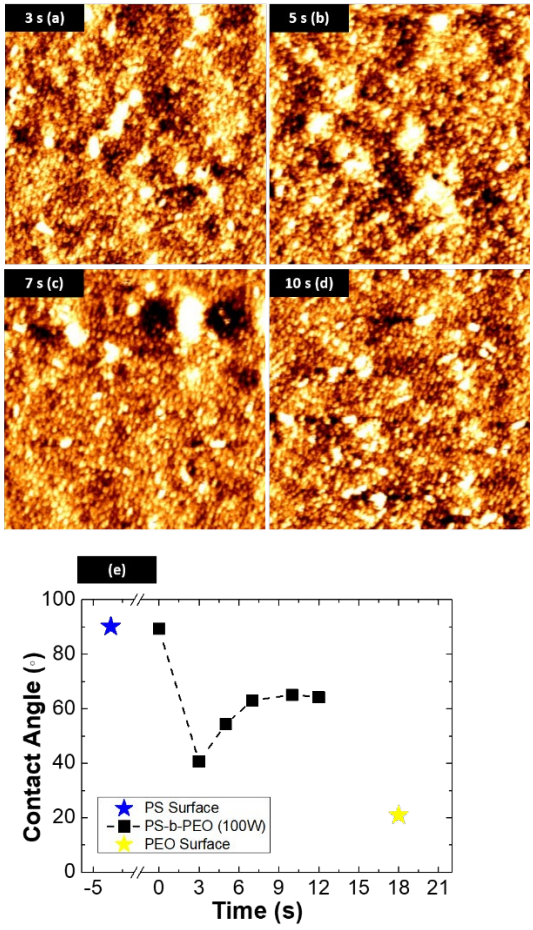

Figure S2-4. Evolution of surface morphology and wettability. AFM topographic images of PS-*b*-PEO after exposure to argon plasma using a flow rate of 15 sccm and a RF power (a-d) 100 W and (e) their corresponding water contact angle. The contact angle value for the PS surface was determined experimentally using a film prepared from a 1wt% PS solution dissolved in toluene (blue star, on the left). The contact angle value for PEO was taken from ref[36]

Large-scale Microphase Separation and Etching Phenomenon Analysis on PS-*b*-PEO (42K-*b*-11.5K) exposed to argon plasma for 15 s under a flow rate of 10 sccm and a RF power of 60 W: Figure S2-5.

Surface reorganisation *via* argon exposure is noticeable in Figure S2-5 (a,b) with little damage to the surface or delamination of the film. This suggests the process is not a local event and happens across the entire surface. As for Figure 2-5, the small lines visible are due to the gold layer, sputtered atop the surface to limit the charging effect.

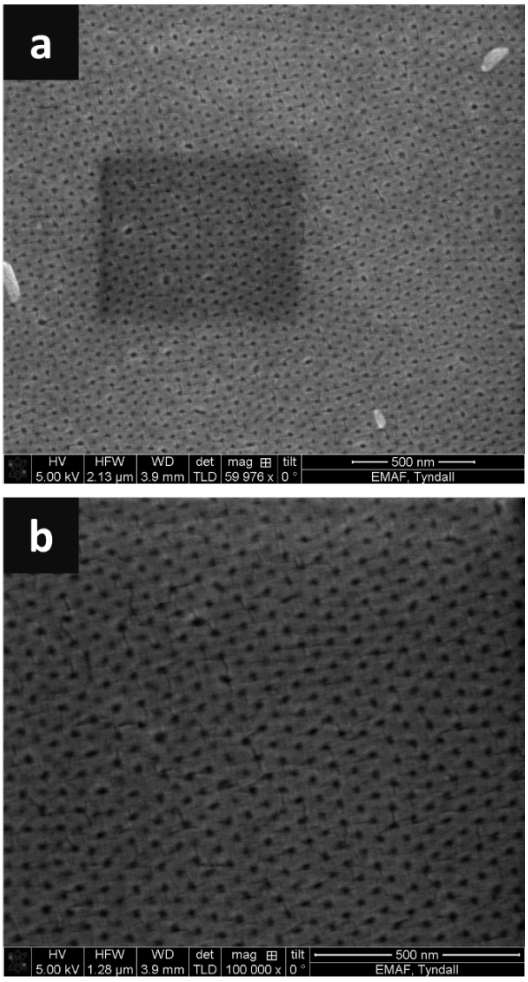

Figure S2-5. Top down SEM images of PS film exposed to argon plasma for 15 s with a flow rate of 10 sccm and a RF power of 60 W.

Chapter 3

Highly Ordered Titanium Dioxide Nanostructures via a Simple One Step Vapour Inclusion Method in Block Copolymer Thin Films

3.1. Abstract

Nanostructured crystalline titanium dioxide (TiO_2) finds applications in numerous fields such as photocatalysis or photovoltaics where its physical and chemical properties depend on its shape and crystallinity. We report a simple method of fabricating TiO_2 nanowires by selective area deposition of titanium tetraisopropoxide (TTIP) and water in a facile vapour phase (CVD-like) approach at low temperature by utilizing a PS-*b*-PEO self-assembled block copolymer thin films as template. Parameters such as exposure time to TTIP (minutes to hours), working temperature (~18 to 40 °C) and relative humidity (20 to 70 %) were systemically investigated through GISAXS, SEM and XPS and optimized for fabrication of TiO_2 nanostructures. The resulting processing conditions yielded titanium dioxide nanowires with a diameter of 24 nm. An extra calcination step (500 °C) was introduced to burn off the remaining organic matrix and introduce phase change from amorphous to anatase in TiO_2 nanowires without any loss in order.

3.2. Introduction

Crystalline and nanocrystalline titanium dioxide (TiO_2), is one of the most studied transition-metal oxides due to its excellent physical and chemical properties. Depending on the TiO_2 polymorph (*i.e.* anatase, rutile and brookite or combinations thereof), TiO_2 nanostructures find applications in various fields such as gas sensing[1,2] photovoltaics[3,4], photocatalysis[5,6] and cell-culture[7].

Methods for forming TiO_2 include chemical and physical vapour deposition (CVD and PVD)[8-10] sol-gel[11,12] plasma laser deposition (PLD)[13], atomic layer deposition (ALD and PEALD)[14-17] and reactive electron beam evaporation[18]. However, those methods (apart from sol-gels) require precision control of gas flow, substrate temperature and working pressure. Although the above mentioned TiO_2 production methods yield highly crystalline films, they require costly equipment and offer poor control over nanostructural arrangement, significantly limiting nanoapplications.

Self-assembled block copolymer (BCP) patterning and/or templating offers a cost-effective approach for the formation of well-defined nanostructured thin film architectures. Block copolymers consist of two (or more) incompatible, covalently bonded polymers that form ordered morphologies with dimensions of sub-10 to 100 nm when phase-separated in the

right conditions[19-21]. BCP thin films can be used to produce an organic/inorganic hybrid material. The organic component can be subsequently removed, yielding nanostructured inorganic materials[22]. In the past, sol-gel processes have been widely used to form titanium dioxide where a polymer solution and a metal precursor (usually alkoxides) solution are mixed together prior to film coating[23-25] or evaporation[26]. A range of different nanostructures (micelles, worm-like, nanowires, nanodots, etc.) may be obtained through controlling a wide range of conditions including sol-gel concentration, solvent, evaporation rate and spin coater speed. However, titanium alkoxide precursors are highly reactive with water and generally require acidic solutions (*e.g.* acetic acid, hydrochloric acid and trifluoroacetic anhydride) to stabilize the precursors and slow down their hydrolysis[27,28]. Evaporation induced self-assembly (EISA) method, among other sol-gel techniques, is a commonly used method for templating inorganic materials. However, obtaining highly ordered nanostructured films via this approach remains highly challenging[29]. An alternative, single step fabrication route involves incorporating pre-formed particles within block copolymer solutions, allowing precise control of the size, shape and crystallinity of the particles. Limited miscibility between the inorganic particles and BCP solutions, however, often results in segregation and is therefore a significant drawback.

Control over nanostructure shapes (nanowires, nanodots, etc.) and, hence, titanium dioxide nanostructures, can be obtained by decoupling block copolymer self-assembly from metal oxide incorporation. Here, BCP templates are used as a scaffold or template for the formation of inorganic nanostructures[30]. After removal of all organic components, a one-to-one registration is observed between the original pattern and the inorganic counterpart. The order of resulting oxide arrangement is strictly dependent on the film order of the original BCP film. In the methods reported in the literature, for the oxide to be selectively incorporated in the hydrophilic part of the BCP, a metal precursor in a compatible solvent solution can be spun cast over the substrate[31]. Alternatively, the pattern may be immersed in metal precursor solution[32]. However, as for sol-gel methods, precise control over metal precursor concentration and stabilization is required.

Here, we adapt the former approach (decoupling pattern formation from metal incorporation) by introducing the metal precursors using a CVD-like method. To date, extensive work has been carried out onto PS-*b*-PMMA in CVD, ALD and SIS chambers[33] to form nanostructured materials and thin films[34-36.] However, to our knowledge, no attempt using

simple evaporation of the precursors under ambient and low temperature has been recorded. Because we aim to selectively deposit inorganic material, PS-*b*-PEO is a block-copolymer of choice for templating, over PS-*b*-PMMA, as hydrophilic functional groups (Ti-O) are capable of bonding with the hydrophilic PEO component[37].

Advantaging the amphiphilic properties of PS-b-PEO, the high chemical contrast of the two blocks and the hydrolysis of a titanium alkoxide precursor, we are able to form well-ordered TiO_2 nanostructures without the need of any precise precursor solution formulation or high control over gas flow and pressure. Furthermore, no complex chamber or processing is required as it is for ALD method. The method presented here (although similar to SIS which borrows its chemistries from ALD and consists of cyclic infiltration and reaction), eliminates the sequential steps of the SIS process[34]. All chemicals, including the titanium precursor, are introduced to the chamber at the same time. Highly uniform TiO_2 nanowires and nanodots mimicking the original BCP patterns are produced over large area as evidenced by microscopy analysis. Additionally, this novel approach is both industrially compatible and environmental-friendly (minimizing solvent used). We envisage that the simple, yet highly effective process reported herein may be used widely for selective vapour infiltration of block copolymer domains producing functional inorganic nanostructured materials.

3.3. Experimental

Materials. Highly polished single-crystal silicon <100> wafers (p-type) with a native oxide layer (~2-5 nm) were used as a substrate. No attempt was taken to remove the native oxide. Wafers were cleaned by ultrasonication in acetone and toluene respectively for 20 min and dried with a nitrogen stream prior to deposition of the BCP via spincoating. PS-*b*-PEO was purchased from Polymer Source Inc. (Dorval, Canada) and used without any further purification. (Mn_{PS} = 42 kg mol^{-1}, Mn_{PEO} = 11.5 kg mol^{-1} where Mn is the number average molecular weight, PDI = 1.07 where PDI is the polydispersity index). Titanium tetraisopropoxide (TTIP, 97%), titanium butoxide (TB), toluene (HPLC grade, 99.9%), acetone (HPLC grade, ≥ 99.8%) were purchased from Sigma-Aldrich and used as received.

Template and titanium dioxide formation.

Block-copolymer solution preparation, deposition and pattern formation: Solutions of PS-*b*-PEO were made in toluene (1 wt%) and stirred for at least 1 hour prior to use. Following

dissolution, PS-b-PEO thin films were formed by spincoating the 1 wt% BCP solution at 3000 rpm for 30 s onto Si wafer, using a SCS G3P-8 spincoater. Post deposition, the as-cast films were solvent annealed. Films were placed in a 150 mL closed glass jar with a small vial containing 3 mL of toluene and annealed at 60 °C. Line formation (a single row of parallel hexagonally arranged PEO cylinders in a PS matrix) was induced with a 2-hour annealing time.

Titanium dioxide nanostructure formation: Samples were attached upside-down at the top of a 15 mL-closed glass vial (height = 50 mm, diameter = 24 mm) containing 1 mL of titanium tetraisopropoxide. Exposure to TTIP vapour results in the formation of titanium hydroxides and was conducted under ambient temperature (~ 18 °C), 30 °C and 40 °C for time intervals ranging from 5 minutes to 4 hours. In addition, to study the influence of humidity on the evaporation rate of TTIP and subsequent nanostructures formation, the vials were placed in a relative humidity-controlled chamber where relative humidity varied between 20 and 70 RH. The deposited titanium hydroxide nanostructures were oxidized to form titanium dioxide via UV ozone treatment for 3 hours (PSD Pro Series Digital UV/Ozone System; Novascan Technologies, Inc., USA). UV/ozone treatment was also used to ensure the stability of the nanostructures. Samples were then subjected to high temperature (400 to 800 °C) for 2 to 4 hours with 1 and 5 °C /min ramp, resulting in calcination and altering to promote the formation of the anatase phase of titanium dioxide. All the results shown were obtained after calcination at 500 °C unless otherwise stated.

Characterization. BCP film thicknesses were measured using a spectroscopic ellipsometer "Plasmos SD2000 Ellipsometer" at a fixed angle of 70 °C on at least five different places on the sample and was reported as the film thickness result. A two-layer model (SiO_2 + BCP) was used to simulate experimental data. Surface morphologies of the nanostructured thin films were analysed with an AFM (Park systems, XE-100) in tapping mode under ambient conditions using silicon microcantilever probes tips with a force constant of 42 Nm^{-1}. Topographic, phase and amplitude images were recorded simultaneously. AFM was used to ensure the quality of the film before titanium dioxide nanostructure formation. SEM measurements were carried out on a JEOL model FEI FP 2031/11 Inspect F field emission instrument at an accelerating voltage of 10 or 20 kV. X-Ray Photoelectron Spectroscopy (XPS) was performed on VG Scientific ECSAlab Mk II system using Al Kα mono X-ray source (1486.6 eV). XPS analysis was used to inform about the chemical state of the

titanium. Raman scattering spectroscopy was collected with a Renishaw InVia Raman spectrometer equipped with a 2400 lines/mm grating using a 514 nm 30 mW Argon Ion laser, spectra were collected using a RenCam CCD camera. The beam was focused onto the samples using either a 20x or 50x objective lens. The laser power density was adjusted to ensure that the thin film surfaces did not undergo sample heating during the full spectral acquisition time. X-Ray Diffraction (XRD) analysis was performed using a Phillips Xpert PW3719 diffractometer using Cu Kα radiation. (Cu Kα, λ = 0.15418 nm, operation voltage 40 kV, current 40 mA). Grazing-Incidence Small-Angle X-ray Scattering (GISAXS) was performed at beamline I07 and I22, Diamond Light Source Ltd (Didcot, Oxfordshire, UK).

3.4. Results and Discussion

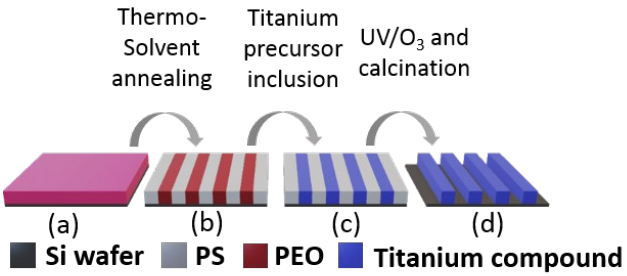

Scheme 3-1. Illustration of the formation of titanium dioxide nanowires. (a) As-cast thin film of PS-*b*-PEO solution on Si substrate, (b) self-assembled PS-*b*-PEO obtained after thermo-solvent annealing at 60 °C in toluene vapour; (c) PS-*b*-PEO thin film with SEO/TiO_2 hybrid and (d) titanium dioxides nanowires after UV/O_3 and calcination process.

The method used to produce ordered titanium dioxide nanowires is illustrated in Scheme 3-1.

Block Copolymer Self-Assembly.

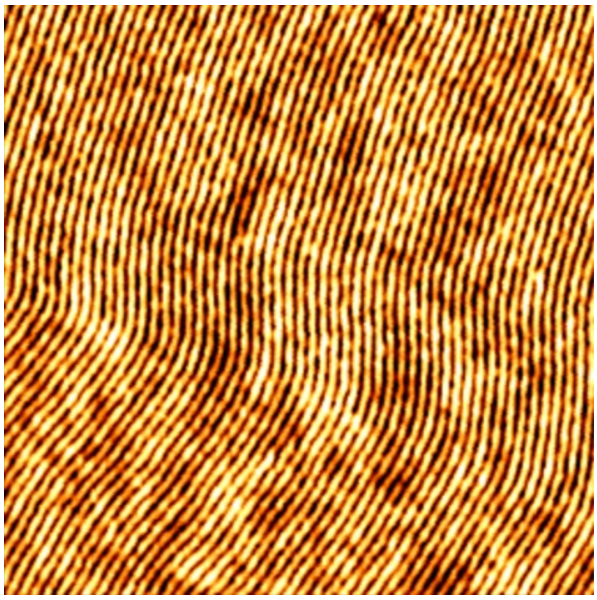

Figure 3-1. AFM image (2x2 μm) of self-assembled PS-*b*-PEO thin film acting as a template. Conditions for thermo-solvent annealing was exposure to toluene vapours for 2 hours at 60 °C.

The first stage in this novel CVD-based TiO_2 nanostructure fabrication route utilises BCP thin films acting as a template for selective adsorption of a TiO_2 precursor. BCP films possess a propensity to self-assemble via microphase separation, forming highly ordered nanostructures. PS-*b*-PEO thin films were fabricated via spin-coating to produce highly uniform thin films with thicknesses of ~40 nm as measured by ellipsometry (Figure S3-1). As-cast films show poorly ordered films with mixed orientation of PEO cylinders within a PS matrix and, therefore, do not possess a significant degree of long-range order that would make them attractive templates for the generation of ordered TiO_2 nanostructures. Solvo-thermal annealing was used to optimise the BCP morphology, where the combination of heat and solvent vapour are employed to promote mobility of the polymer chains, enabling chain re-organization and the formation of morphologies closer to thermodynamic equilibrium.

On one hand, toluene is a good solvent for the PS domains, allowing the chains to stretch to maximize their contact with the solvent molecules (At T = 298K, the solvent-polymer interaction parameters[38,39] were estimated as $\chi_{PS\text{-}tol} = 0.46$ and $\chi_{PEO\text{-}tol} = 5.34$. They indicate good dissolution if smaller than 0.5).

The Antoine equation is a class of semi-empirical correlations that describes the relation between temperature and vapour pressure for a pure substance, and is defined as:

$$\log_{10} p = A - \frac{B}{C+T} \qquad (3\text{-}1)$$

where p is the vapour pressure, T is the temperature and A, B and C are component-specific constants. Using the data from Besley and Bottomley[40], the National Institute of Standards and Technology calculated the coefficients for the temperature range 273.13 K – 297.89 K. At room temperature (20 °C), the vapour pressure of toluene is 2.96 kPa. This pressure is too low for the vapour to penetrate the glassy PS film[41] and enhance chain mobility and favour phase-separation. Such a phenomenon, the swelling of a polymer glass by sorption of a small molecule (toluene), is known as case-II diffusion. Increasing the temperature to 60 °C rises toluene vapour pressure to 19.93 kPa and the amount of toluene molecules in the gas phase. Because of the case-II diffusion for glass polymer, it is assumed that more toluene molecules can be absorbed into the polymer network, solvating the polystyrene chains and promoting their mobility. This absorption mechanism is driven by the chemical potential equilibrium which is linked to the swelling of the polymer film in order to balance the forces between the gas phase and the polymer film. At higher temperature and higher toluene vapour pressure, the swelling of the polymer film is increased and can cause dewetting in some areas. As such, to induce phase separation of the block copolymer film at 60 °C, it is necessary to limit the exposure time of the film to toluene vapours. There is a balance between how much the film can be swelled without being dewetted, and how much toluene species can be absorbed to solvate the polystyrene and induce its mobility.

On the other hand, water is a good solvent for the PEO[42] domains, due to hydrophilic interactions, and the air moisture in the annealing chamber is sufficient to induce mobility of PEO chains. A topographic AFM image of a BCP film exposed to toluene vapour at 60 °C for 2 hours is shown in Figure 3-1 where the centre-to-centre distance was measured to be 38 nm with a line width of 26 nm comparable with dimensions in our previous studies[30,41]. The ability of BCP thin films to adopt different nanoscale morphologies[41] offers routes to generate a range of different TiO_2 nanostructures. Figure S3-2 presents vertical arrangement (pillars) of PEO domains with a PS matrix and, after incorporation, subsequent titanium dioxide nanodots.

Titanium dioxide nanostructure fabrication.

To fabricate TiO_2 nanowires, PS-*b*-PEO thin films with morphologies consisting of cylinders orientated parallel to the surface were used as a template (Figure 3-1) to generate the desired titanium dioxide nanostructures. This was achieved by exposing the BCP thin films to titanium alkoxide vapour, which undergoes hydrolysis and subsequent condensation to form titanium hydroxides. Titanium alkoxide precursors, known to be susceptible to hydrolysis, are scarcely used in aqueous or humid environments[43] and are often diluted in alcohol prior to use to manage the reaction rate[44]. The two different components of PS-*b*-PEO possess different affinities to titanium alkoxides. PEO has been shown to have a high affinity for cations due to hydrophilic inter-action between cations and oxygen atoms from the PEO domain[45]. On the contrary, the hydrophobic nature of the PS excludes cation incorporation. By exposing the polymer film to pure titanium tetraisopropoxide (TTIP) solution, we aim to selectively deposit Ti^{4+} cations within the PEO domains. After ion incorporation, UV ozone treatment was performed to ensure complete oxidation of the titanium precursor to titanium dioxide and to remove most organic components (TTIP reacting with PEO, it is likely that some PEO remains under TiO_2 domains). The resulting titanium dioxide nanowires, after 3 hours of exposure to TTIP vapour and UV ozone treatment, have a thickness of 12 nm as determined by ellipsometry (Figure S3-1). In the approach presented herein, precise control over the relative humidity (RH) and temperature enables selective generation of TiO_2 onto the PEO domains of the BCP template.

Influence of the Precursor.

Two different titanium alkoxide precursors were investigated, titanium tetraisopropoxide and titanium butoxide, which both possess high volatility and high vapour pressure making them suitable for this CVD-based approach. AFM images of titanium dioxide formed under ambient conditions (~18 °C) after 30- to 255-minute exposure to TTIP vapour are available in Figure S3-3. AFM images of titanium dioxide nanowires formed under ambient conditions (ambient temperature, without control over relative humidity) after exposure to TTIP vapours for (a) 30 min, (b) 75 min, (c) 120 min, (d) 150 min, (e) 210 min and (f) 255 min. The average line width was measured to be 24 nm (2 nm smaller than the original template[30]) while the average centre-to-centre distance was 38 nm. However, when using titanium butoxide, little or no titanium dioxide nanostructures were observed. This is due to a phenomenon called oligomerisation which lower the volatility of titanium butoxide[16].

Oligomerisation is the formation of polymeric species, *e.g.* $(Ti(OBu)_4)_n$, and is driven by the tendency of the metal to saturate its coordination number. As such, the alkyl group act as a bridging ligand with increased intermolecular forces within the alkyl chains. Compared to the titanium butoxide monomer, the volatility of the oligomer is decreased. Furthermore, titanium butoxide existing as a polymeric cluster, its incorporation within PEO domains is prevented by steric hindrance. On the contrary, it is well known that bulky alkyl groups prevent oligomerisation and promote higher volatility. This is the case for titanium tetraisopropoxide.

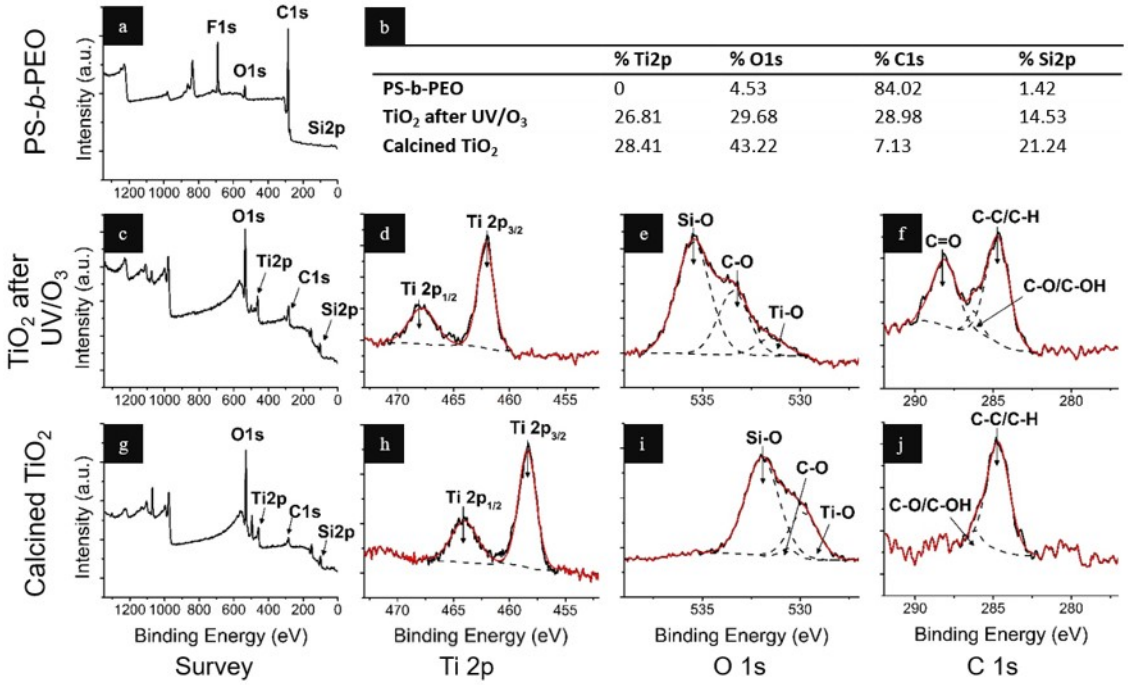

Figure 3-2. XPS spectra of (a) block copolymer thin film prior to titanium dioxide incorporation, (c) – (f) titanium dioxide nanowires on silicon after UV ozone treatment and before calcination at 500 °C, and (g) – (j) titanium dioxide nanowires on silicon wafer after UV ozone treatment and calcination. High resolution XPS spectra were recorded for Ti 2p core level (d) and (h), O 1s core level (e) and (i), and C 1s core level (f) and (j). Table (b) gives the atomic percentage of each element. Conditions for titanium dioxide formation are as follow: 20 min exposure to TTIP, at 30 ºC and 60 RH.

XPS was used to study the chemical nature of the incorporated titanium precursor after UV-O_3 treatment and after calcination. Data shown here, in Figure 3-2, are for titanium dioxide nanowires obtained after 20 min exposure to TTIP, at 30 °C and 60 RH. Recorded surface survey after UV-O_3 treatment and calcination indicated the presence of expected elements (Si, Ti, O) as well as C *1s* (286 eV) peaks as shown in Figure 3-2 (f) and (j). The fluorine peak, only present in the PS-*b*-PEO thin film survey, Figure 3-2 (a) is believed to be a

consequence of cross-contamination. Most organic components are removed following UV-O_3 treatment, as shown in the Table (b) of Figure 3-2, with a drop in C *1s* atomic percentage from 84 to 29 % due to polymer degradation after exposure to UV-O_3.

Calcination process at 500 °C, under ambient conditions, is applied to remove even further the remaining traces of the organic matrix. Another drop in C *1s* atomic percentage from 29 to 7% is observed for the same sample. Furthermore, an increase in Si *2p* atomic percentage after two hours of calcination at 500 °C is an indirect evidence of removal of the organic matrix as more silicon surface is readily available. As such, the contrast observed in the SEM images (Figure 3-3) reflects the formation of the inorganic TiO_2 nanowires. Extensive Ti *2p* spectra, Figure 3-2 (d) and (h), were recorded to analyse with exactitude the titanium chemical environment. The Ti *2p* doublet observed is characteristic to Ti^{4+} species in TiO_2 (O–Ti–O bonding)[46, 47]. It consists of Ti $2p_{3/2}$ peak at ~460 eV (462 and 458.5 eV before and after calcination, respectively) and Ti $2p_{1/2}$ peak at ~466 eV (468 and 464 eV before and after calcination, respectively). The presence of Ti^{3+} and Ti^{2+} species are not observed within experimental error. Figure 3-2 (e) and (i) show the core level of O *1s* spectra, before and after calcination, which consist of a broad peak. The peaks centred at 531.4 and 529.8 eV, before and after calcination respectively are attributed to titanium dioxide at the surface[48] (Ti-O bonds). Peaks at 535.4 and 531.9 eV are attributed to SiO_2 while peaks at 533.4 and 530.6 eV are attributed to the presence of remaining PEO groups after UV-O_3 treatment and calcination (C-O and C=O bonds). Presence of the polymer is also confirmed in Figure 3-2 (f) and (j) with peaks at 288.2 and 286.3 eV before calcination, and peak at 286.2 eV after calcination. Adventitious carbon peak was calibrated to be 284.8 eV. Calcination of samples is a requirement to obtain pure titanium dioxides nanostructures supported on SiO_2.

Influence of the temperature on titanium precursor deposition.

Under ambient conditions (at T ~18°C), well-defined amorphous TiO_2 nanostructures were obtained after 2 hours and up to 4 hours of TTIP exposure (Figure S3-3). Evaporation and incorporation processes can be accelerated and optimized by changing the working temperature. At fixed relative humidity, increasing the temperature from 18°C (room temperature) to 30 °C enhances TTIP evaporation rate due to higher vapour pressure. Also, it decreases effective exposure time needed to form titanium dioxide nanowires dramatically from hours (Figure S3-3) to minutes (*e.g.* Figure 3-3 h). At 40 °C (Figure S3-3 and Figure S3-5), however, the hydrolysis rate of TTIP is too high and it is not possible to generate TiO_2

nanostructures reproducibly. Further, it was not possible to achieve selective incorporation within the PEO domains, leading to overfilling and increased surface roughness. Due to the faster evaporation rate, there is a competition between selective incorporation into the PEO domains and gas-phase reaction between TTIP and water vapour before reaching the substrate[49]. Additional data on the evolution of nanowires fabricated at 40 °C is available in appendix (Figure S3-4 and Figure S3-5).

Influence of relative humidity on titanium precursor deposition.

SEM images (Figure 3-3) show the evolution of titanium dioxide formation as a function of relative humidity (y-axis) and exposure time (x-axis) at fixed temperature of 30 °C. Images were taken after exposure to UV-O_3 for 3 hours. Low relative humidity values (under 40 RH), lowering "air moisture", requires longer exposure time to form well-defined TiO_2 as shown in Figure 3-3 (m-p): after 5 minutes exposure, no nanostructures are observed at 30 RH. To form nanostructures after a short exposure to TTIP vapour, it is necessary to increase the relative humidity: higher water content favours TTIP hydrolysis and evaporation while enhancing Ti–O bond formation[49]. In Figure 3-3 (i-l) and (e-h), 50 and 60 RH respectively, nanowires formation is observed after 5 min exposure to TTIP. Although, best results are obtained after longer exposure time of 15 - 20 minutes. At high relative humidity values, 70 RH and above, the substrate tends to overfill, and nanowires are not well defined. Sometimes, a titanium dioxide film covering the surface can be observed: chemical reaction between the precursor and water molecules occur in the gas state prior to deposition (as seen in Figure S3-4). Such a phenomenon is beginning to be visible for longer exposure time at 70 RH as shown in Figure 3-3 (d). These observations give information about the existence of an optimized processing window for the formation of titanium dioxide nanowires. Figure 3-3 (l), surrounded by an orange border, shows well-defined nanowires obtained after 20 minutes of exposure to TTIP at 30 °C and 50 RH.

For more quantitative information regarding TiO_2 nanowires incorporation, Grazing Incidence Small Angle X-Ray Scattering (GISAXS) was performed. Figure 3-4 (a-e) shows the GISAXS data for samples exposed to TTIP vapour at 30 °C, 60 RH for 5 - 25 minutes. The corresponding SEM images are available in Figure 3-3 (e)-(h), excluding 25 minutes of exposure. Note that Figure 3-4 (a) is the starting reference for the experiment showing a native self-assembled PS-b-PEO thin film, prior to TTIP exposure. The two-dimensional GISAXS patterns presented in Figure 3-4 (a-g) exhibit strong scattering features

perpendicularly orientated to the substrate surface, corresponding to cylinder domains aligned parallel to the substrate. By increasing the TTIP exposure time, initially the intensity of the first order peak increases (Figure 3-4 b-d) and reaches a maximum after 15 minutes (Figure 3-4 d). However, when increasing the exposure time further and beyond 20-25 minutes, the intensity of the first order peak becomes significantly weaker, Figure 3-4 (e-f).

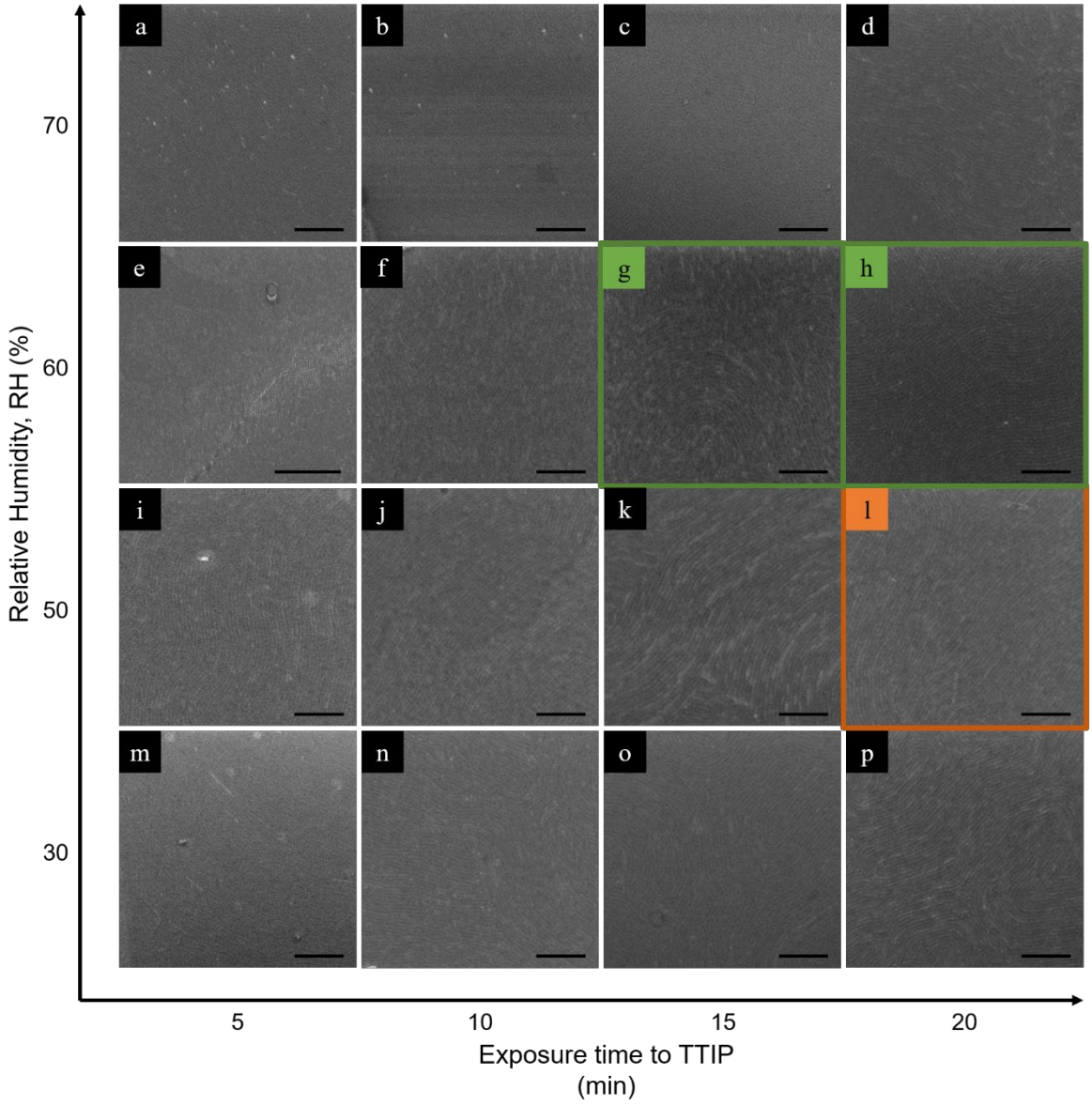

Figure 3-3. SEM images showing the evolution of formed titanium dioxide nanowires at 30 °C as a function of exposure time to TTIP (x-axis) and relative humidity (y-axis). The self-assemble BCP thin films were exposed to TTIP in 70% relative humidity for (a) 5 min, (b) 10 min, (c) 15 min and (d) 20 min ; in 60% relative humidity for (e) 5min, (f) 10 min, (g) 15 min, (h) 20 min ; in 50% relative humidity for (i) 5 min, (j) 10 min, (k) 15 min and (l) 20 min; in 30% relative humidity for (m) 5 min, (n) 10 min, (o) 15 min and (p) 20 min. All scale bars = 500 nm, except in (e) were scale bar = 1 µm. All images were taken after a 3-hour UV ozone treatment.

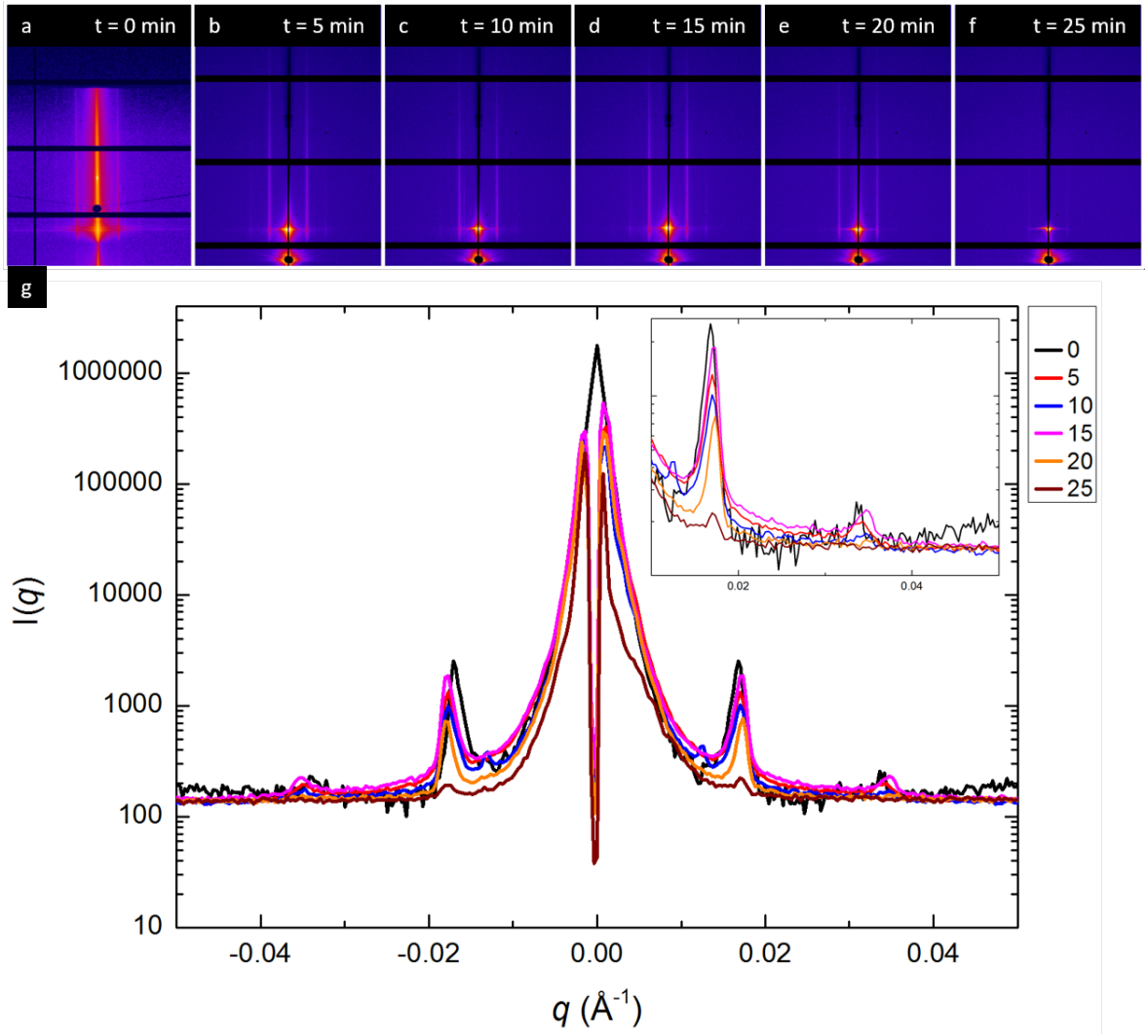

Figure 3-4. Experiment recorded on titanium dioxide nanowires made at 30 °C, under 60 RH a after UV-O_3. 2D-GISAXS patterns of (a) self-assemble BCP thin film (no exposure to titanium), and titanium dioxide nanowires after an exposure time to TTIP of (b) 5 min, (c) 10 min, (d) 15 min, (e) 20 min and (f) 25 minutes respectively. Intensity profile (g) showing peak intensity as a function of q, at various time.

We believe this reflects that in the initial part of the process, the reaction of TTIP forms a significant amount of titanium on the PEO domains (before being oxidized to TiO_2 after UV-O_3 treatment). After 15 minutes a saturation point is reached, and the intensity of the first order peak scattering diminishes as titanium hydroxides covers both PEO and PS domains. As a result of full coverage, instead of selective impregnation to PEO domains, the contrast between the domains diminished and the scattering pattern weakens. Moreover, for exposure time of 5, 10 and 15 minutes, in Figure 3-4 (b-d), a second order peak is visible. This second

order peak disappear after 15 minutes exposure to TTIP, meaning there is an optimum exposure time to titanium tetraisopropoxide.

Figure 3-4 (g) presents the horizontal integrated scattering with the corresponding first and second order position. The position of the first order scattering peak ranges from ~0.0168 to ~0.0174 $Å^{-1}$, corresponding to 37.3 and 36.1 nm respectively. This domain spacing correlates well with the AFM data of the PS-b-PEO template shown in Figure 3-1, where the repeat distance of the PEO domains was ~38 nm. The SEM data provided in Figure 3-3 (e-h, l) together with the corresponding GISAXS data in Figure 3-4 (a-g) reinforce the effectiveness of this simple CVD-based evaporation method to pattern TiO_2 features. A green border on Figure 3-3 (g, h) highlights the optimum process window to form TiO_2 nanowires: 30 °C, 60 RH and 15 – 20 minutes exposure to TTIP.

Calcination and recrystallization of amorphous titanium dioxide nanostructures.

The last stage of this CVD-based method involves calcination of the sample at 500 °C to (a) remove any remaining organic component and (b) convert the titanium dioxide phase from amorphous to anatase. Due to the processing conditions to obtain titanium dioxide nanostructures (low temperature, ambient relative humidity), the TiO_2 nanowires fabricated here are most likely to be amorphous in nature[50]. Following calcination at 500 °C for two hours, titanium dioxide nanowire phases were analysed *via* Raman spectroscopy and XRD. However, because of their small size, analysis was inconclusive. To address the issue, TTIP was drop-cast onto a glass substrate, left to dry and calcined under the same conditions to mimic the ambient processing conditions of this CVD-based approach. Figure 3-5 (a) and (b) represent the phase change from amorphous to crystalline in drop-cast samples as observed with (a) Raman spectroscopy and (b) XRD analysis.

A 514 nm 30 mW Argon Ion laser selected as the excitation source of the UV Raman spectra, Figure 3-5 (a). As expected, before calcination, a broad shoulder at 225 cm^{-1} is observed with broad bands at 320, 439 and 590 cm^{-1} indicating the amorphous nature of the sample (TiO_2). After calcination, the Raman spectra shows major bands at 149, 205, 400, 520 and 642 cm^{-1} can be attributed to the Raman active modes of anatase phase[51, 52]. The change from amorphous to anatase is also confirmed via XRD analysis, Figure 3-5 (b). No peaks are observed before calcination (amorphous phase, black curve in Figure 3-5 b). When calcined at 500 °C, narrow anatase diffraction peaks at 2θ = 25.3°, 37.0°, 37.8°, 38.6°, 48.1°, 53.9°,

55.1° and 62.87° were observed (red line in Figure 3-5 b). Theses peaks represent the (101), (103), (004), (112), (200), (105), (211), and (213) planes of the anatase phase respectively and match the anatase standard values of the XRD pattern JCPDS no. 21-1272 (shown in blue in Figure 3-5 b). Although Raman and XRD spectra were recorded on titanium dioxide powder, we cautiously believe that our titanium dioxide nanowires will have the same crystalline phase *i.e.* anatase.

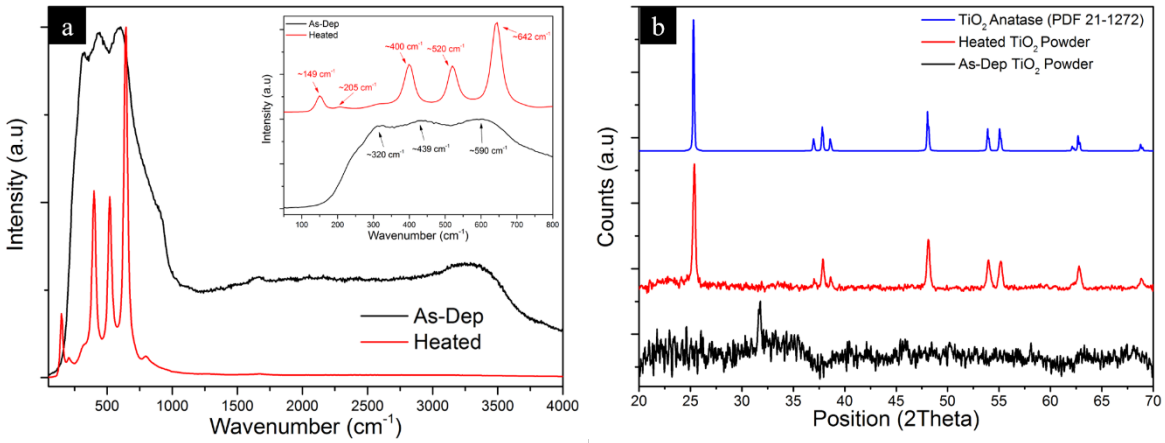

Figure 3-5. Raman spectra of titanium dioxide powder before (black curve, top) and after (red curve, bottom) calcination at 500 °C, showing the intensity as a function of wavenumber. **(b)** XRD spectra of titanium dioxide powder before (black curve, bottom), after (red curve, middle) calcination, and according to PDF 21-1271 anatase (blue curve, top)

Alongside the phase change from amorphous to crystalline materials, the calcination process was also used to test the thermal stability of the titanium dioxide nanowires formed. GISAXS was performed on titanium dioxide nanowires before and after the calcination process (Figure S3-6). Data show that the overall order of the system increases after calcination, with an increase in the intensity of the first order scattering peak and a second order scattering peak becoming visible. Additionally, there is a small shift in the position of the first order peak (0.01724 to 0.01709 $Å^{-1}$), which is ascribed to a small increase in the domain spacing and a reduction in nanowire width, consistent with high temperature densification.

3.5. Conclusions

In summary, this work demonstrates how block copolymer thin films may be used to template the formation of titanium dioxide nanostructure via exposure to alkoxide precursor

vapour followed by subsequent oxidization. This CVD-based approach decouples thin film ordering from titanium dioxide deposition to allow definition and control of the geometry of the initial PS-*b*-PEO pattern and, hence, the resulting titanium dioxide structure. Pattern arrangement and size is intrinsically dependent on the molecular weight and the relative volume fraction of the block copolymer used.

Titanium dioxide was selectively deposited into the hydrophilic block, PEO, utilizing low temperature (from ambient temperature to 40 °C) and a well-known CVD-inspired chemistry: titanium tetraisopropoxide (TTIP) and water as precursors. The quantity of water introduced in the system was controlled by the relative humidity present in the chamber, which was modified from 20 to 70 RH. Alongside the relative humidity, the quality of the titanium dioxide nanostructures was tuneable as a function of exposure time to TTIP and temperature. SEM images and GISAXS data suggest the existence of an optimal process window that provides the best ordered pattern: 30 °C, 60 RH, and 15 minutes exposure to TTIP. XPS data taken after UV-O_3 treatment confirm the presence of titanium dioxide. Further XPS data, taken after calcination at 500 °C for 2 hours, show that all PEO and polymer matrix are removed. Because titanium dioxide nanowires obtained were small (~24 nm in diameter), Raman and XRD analysis were carried out on pure calcined drop casted TTIP exposed using the same processing conditions. Both Raman and XRD data confirmed the phase transformation of TiO_2 nanowires from amorphous to anatase after calcination.

Compared to ALD and CVD approaches, this evaporation-based process operates at a much lower temperature and is free from costly equipment and complex processing. Compared to sol-gel techniques used to form titanium dioxide, this approach is more user and environmentally friendly as there is no need to prepare a metal precursor solution *i.e.* TTIP is used pure and no solvent (ethanol, methanol, etc.) is utilised. Furthermore, additional calcination fully removes the remaining organic mask, and most likely crystallises amorphous titanium dioxide to anatase without any loss of order. We believe that the evaporation-based approach demonstrated here is a suitable technique for selective deposition at low temperature and a safe environment to produce a large variety of oxides. With the titanium dioxide nanostructures being a few nanometres high after pattern transfer, those nanostructures are fit for industrial purposes, notably in the solar cell industry and gas sensor. A further advantage of our process is the short process time (less than two hours) for

microphase separation of the block copolymer thin film to followed by the calcination of the titanium dioxide nanostructures.

3.6. References

(1) Varghese, O. K.; Gong, D.; Paulose, M.; Ong, K. G.; Grimes, C. A. Hydrogen Sensing Using Titania Nanotubes. *Sensors and Actuators B: Chemical* **2003**, *93* (1–3), 338–344. https://doi.org/10.1016/S0925-4005(03)00222-3.

(2) Zhu, Y.; Shi, J.; Zhang, Z.; Zhang, C.; Zhang, X. Development of a Gas Sensor Utilizing Chemiluminescence on Nanosized Titanium Dioxide. *Anal. Chem.* **2002**, *74* (1), 120–124. https://doi.org/10.1021/ac010450p.

(3) Adachi, M.; Murata, Y.; Okada, I.; Yoshikawa, S. Formation of Titania Nanotubes and Applications for Dye-Sensitized Solar Cells. *J. Electrochem. Soc.* **2003**, *150* (8), G488–G493. https://doi.org/10.1149/1.1589763.

(4) Nedelcu, M.; Lee, J.; Crossland, E. J. W.; Warren, S. C.; Orilall, M. C.; Guldin, S.; Hüttner, S.; Ducati, C.; Eder, D.; Wiesner, U.; et al. Block Copolymer Directed Synthesis of Mesoporous TiO_2 for Dye-Sensitized Solar Cells. *Soft Matter* **2008**, *5* (1), 134–139. https://doi.org/10.1039/B815166K.

(5) Langlet, M.; Kim, A.; Audier, M.; Guillard, C.; Herrmann, J. M. Transparent Photocatalytic Films Deposited on Polymer Substrates from Sol–Gel Processed Titania Sols. *Thin Solid Films* **2003**, *429* (1–2), 13–21. https://doi.org/10.1016/S0040-6090(02)01290-7.

(6) Guan, Z.-S.; Zhang, X.-T.; Ma, Y.; Cao, Y.-A.; Yao, J.-N. Photocatalytic Activity of TiO_2 Prepared at Low Temperature by a Photo-Assisted Sol-Gel Method. *Journal of Materials Research* **2001**, *16* (04), 907–909. https://doi.org/10.1557/JMR.2001.0128.

(7) He, J.; Zhou, W.; Zhou, X.; Zhong, X.; Zhang, X.; Wan, P.; Zhu, B.; Chen, W. The Anatase Phase of Nanotopography Titania Plays an Important Role on Osteoblast Cell Morphology and Proliferation. *J Mater Sci: Mater Med* **2008**, *19* (11), 3465–3472. https://doi.org/10.1007/s10856-008-3505-3.

(8) Ahmad, Md. I.; Fasel, C.; Mayer, T.; Bhattacharya, S. S.; Hahn, H. High Temperature Stability of Nanocrystalline Anatase Powders Prepared by Chemical Vapour Synthesis under Varying Process Parameters. *Applied Surface Science* **2011**, *257* (15), 6761–6767. https://doi.org/10.1016/j.apsusc.2011.02.121.

(9) Shi, J.; Wang, X. Growth of Rutile Titanium Dioxide Nanowires by Pulsed Chemical Vapor Deposition. *Crystal Growth & Design* **2011**, *11* (4), 949–954. https://doi.org/10.1021/cg200140k.

(10) Halary, E.; Benvenuti, G.; Wagner, F.; Hoffmann, P. Light Induced Chemical Vapour Deposition of Titanium Oxide Thin Films at Room Temperature. *Applied Surface Science* **2000**, *154–155*, 146–151. https://doi.org/10.1016/S0169-4332(99)00425-0.

(11) Agafonov, A. V.; Vinogradov, A. V. Sol–Gel Synthesis, Preparation and Characterization of Photoactive TiO_2 with Ultrasound Treatment. *Journal of Sol-Gel Science and Technology* **2009**, *49* (2), 180–185. https://doi.org/10.1007/s10971-008-1856-3.

(12) Wang, C.-C.; Ying, J. Y. Sol-Gel Synthesis and Hydrothermal Processing of Anatase and Rutile Titania Nanocrystals. *American Chemical Society* **1999**, *11*, 3113–3120. https://doi.org/10.1021/cm990180f.

(13) Major, B.; Ebner, R.; Zieba, P.; Wolczynski, W. Titanium-Based Films Deposited Using a Nd:YAG Pulsed Laser. *Appl Phys A* **1999**, *69* (1), S921–S923. https://doi.org/10.1007/s003390051559.

(14) Potts, S. E.; Profijt, H. B.; Roelofs, R.; Kessels, W. M. M. Room-Temperature ALD of Metal Oxide Thin Films by Energy-Enhanced ALD. *Chem. Vap. Deposition* **2013**, *19* (4–6), 125–133. https://doi.org/10.1002/cvde.201207033.

(15) Ratzsch, S.; Kley, E.-B.; Tünnermann, A.; Szeghalmi, A. Influence of the Oxygen Plasma Parameters on the Atomic Layer Deposition of Titanium Dioxide. *Nanotechnology* **2015**, *26* (2), 024003. https://doi.org/10.1088/0957-4484/26/2/024003.

(16) Ritala, M.; Leskela, M.; Niinisto, L.; Haussalo, P. Titanium Isopropoxide as a Precursor in Atomic Layer Epitaxy of Titanium Dioxide Thin Films. *Chem. Mater.* **1993**, *5* (8), 1174–1181. https://doi.org/10.1021/cm00032a023.

(17) Sinha, A.; Hess, D. W.; Henderson, C. L. Area Selective Atomic Layer Deposition of Titanium Dioxide: Effect of Precursor Chemistry. *Journal of Vacuum Science & Technology B* **2006**, *24* (6), 2523–2532. https://doi.org/10.1116/1.2359728.

(18) van de Krol, R.; Goossens, A. Structure and Properties of Anatase TiO_2 Thin Films Made by Reactive Electron Beam Evaporation. *Journal of Vacuum Science & Technology A: Vacuum, Surfaces, and Films* **2003**, *21* (1), 76. https://doi.org/10.1116/1.1525817.

(19) Matsen, M. W.; Bates, F. S. Unifying Weak- and Strong-Segregation Block Copolymer Theories. *Macromolecules* **1996**, *29* (4), 1091–1098. https://doi.org/10.1021/ma951138i.

(20) Erothu, H.; Kolomanska, J.; Johnston, P.; Schumann, S.; Deribew, D.; Toolan, D. T. W.; Gregori, A.; Dagron-Lartigau, C.; Portale, G.; Bras, W.; et al. Synthesis, Thermal Processing, and Thin Film Morphology of Poly(3-Hexylthiophene)–Poly(Styrenesulfonate) Block Copolymers. *Macromolecules* **2015**, *48* (7), 2107–2117. https://doi.org/10.1021/acs.macromol.5b00213.

(21) Borah, D.; Rasappa, S.; Senthamaraikannan, R.; Kosmala, B.; Shaw, M. T.; Holmes, J. D.; Morris, M. A. Orientation and Alignment Control of Microphase-Separated PS- *b* -PDMS Substrate Patterns via Polymer Brush Chemistry. *ACS Applied Materials & Interfaces* **2013**, *5* (1), 88–97. https://doi.org/10.1021/am302150z.

(22) Cummins, C.; Ghoshal, T.; Holmes, J. D.; Morris, M. A. Strategies for Inorganic Incorporation Using Neat Block Copolymer Thin Films for Etch Mask Function and Nanotechnological Application. *Adv. Mater.* **2016**, *28* (27), 5586–5618. https://doi.org/10.1002/adma.201503432.

(23) Gutierrez, J.; Tercjak, A.; Garcia, I.; Peponi, L.; Mondragon, I. Hybrid Titanium Dioxide/PS-b-PEO Block Copolymer Nanocomposites Based on Sol–Gel Synthesis. *Nanotechnology* **2008**, *19* (15), 155607. https://doi.org/10.1088/0957-4484/19/15/155607.

(24) Cha, M.-A.; Shin, C.; Kannaiyan, D.; Jang, Y. H.; Kochuveedu, S. T.; Ryu, D. Y.; Kim, D. H. A Versatile Approach to the Fabrication of TiO_2 nanostructures with Reverse Morphology and Mesoporous Ag/TiO_2 Thin Films via Cooperative PS-b-PEO Self-Assembly and a Sol-Gel Process. *J. Mater. Chem.* **2009**, *19* (39), 7245–7250. https://doi.org/10.1039/B907922J.

(25) Gutierrez, J.; Tercjak, A.; Mondragon, I. Conductive Behavior of High TiO_2 Nanoparticle Content of Inorganic/Organic Nanostructured Composites. *J. Am. Chem. Soc.* **2010**, *132* (2), 873–878. https://doi.org/10.1021/ja908359k.

(26) Agarwala, S.; Ho, G. W. Synthesis and Tuning of Ordering and Crystallinity of Mesoporous Titanium Dioxide Film. *Materials Letters* **2009**, *63* (18–19), 1624–1627. https://doi.org/10.1016/j.matlet.2009.04.036.

(27) Yoshida, M.; Prasad, P. N. Sol−Gel-Processed SiO_2/TiO_2/Poly(Vinylpyrrolidone) Composite Materials for Optical Waveguides. *Chem. Mater.* **1996**, *8* (1), 235–241. https://doi.org/10.1021/cm950331o.

(28) Boettcher, S. W.; Fan, J.; Tsung, C.-K.; Shi, Q.; Stucky, G. D. Harnessing the Sol-Gel Process for the Assembly of Non-Silicate Mesostructured Oxide Materials. *Accounts of Chemical Research* **2007**, *40* (9), 784–792. https://doi.org/10.1021/ar6000389.

(29) Brezesinski, T.; Groenewolt, M.; Gibaud, A.; Pinna, N.; Antonietti, M.; Smarsly, B. Evaporation-Induced Self-Assembly (EISA) at Its Limit: Ultrathin, Crystalline Patterns by Templating of Micellar Monolayers. *Adv. Mater.* **2006**, *18* (17), 2260–2263. https://doi.org/10.1002/adma.200600258.

(30) Ghoshal, T.; Maity, T.; Godsell, J. F.; Roy, S.; Morris, M. A. Large Scale Monodisperse Hexagonal Arrays of Superparamagnetic Iron Oxides Nanodots: A Facile Block Copolymer Inclusion Method. *Advanced Materials* **2012**, *24* (18), 2390–2397. https://doi.org/10.1002/adma.201200357.

(31) Ghoshal, T.; Shaw, M. T.; Bolger, C. T.; Holmes, J. D.; Morris, M. A. A General Method for Controlled Nanopatterning of Oxide Dots: A Microphase Separated Block Copolymer Platform. *J. Mater. Chem.* **2012**, *22* (24), 12083–12089. https://doi.org/10.1039/C2JM30468F.

(32) Mayeda, M. K.; Hayat, J.; Thomas H Epps, I. I. I.; Lauterbach, J. Metal Oxide Arrays from Block Copolymer Thin Film Templates. *J. Mater. Chem. A* **2015**, *3* (15), 7822–7829. https://doi.org/10.1039/C5TA00117J.

(33) Lee, D. H.; Shin, D. O.; Lee, W. J.; Kim, S. O. Hierarchically Organized Carbon Nanotube Arrays from Self-Assembled Block Copolymer Nanotemplates. *Adv. Mater.* **2008**, *20* (13), 2480–2485. https://doi.org/10.1002/adma.200702712.

(34) Peng, Q.; Tseng, Y.-C.; Darling, S. B.; Elam, J. W. A Route to Nanoscopic Materials via Sequential Infiltration Synthesis on Block Copolymer Templates. *ACS Nano* **2011**, *5* (6), 4600–4606. https://doi.org/10.1021/nn2003234.

(35) Peng, Q.; Tseng, Y.-C.; Darling, S. B.; Elam, J. W. Nanoscopic Patterned Materials with Tunable Dimensions via Atomic Layer Deposition on Block Copolymers. *Adv. Mater.* **2010**, *22* (45), 5129–5133. https://doi.org/10.1002/adma.201002465.

(36) Peng, Q.; Tseng, Y.-C.; Long, Y.; Mane, A. U.; DiDona, S.; Darling, S. B.; Elam, J. W. Effect of Nanostructured Domains in Self-Assembled Block Copolymer Films on Sequential Infiltration Synthesis. *Langmuir* **2017**, *33* (46), 13214–13223. https://doi.org/10.1021/acs.langmuir.7b02922.

(37) Thomas, S.; Grohens, Y.; Jyotishkumar, P. *Characterization of Polymer Blends: Miscibility, Morphology and Interfaces*; John Wiley & Sons, 2014.

(38) Hansen, C. M. *Hansen Solubility Parameters: A User's Handbook, Second Edition*; CRC Press, 2007.

(39) Auras, R. A.; Lim, L.-T.; Selke, S. E. M.; Tsuji, H. *Poly(Lactic Acid): Synthesis, Structures, Properties, Processing, and Applications*; John Wiley & Sons, 2011.

(40) Besley, L. M.; Bottomley, G. A. Vapour Pressure of Toluene from 273.15 to 298.15 K. *The Journal of Chemical Thermodynamics* **1974**, *6* (6), 577–580. https://doi.org/10.1016/0021-9614(74)90045-7.

(41) Mokarian-Tabari, P.; Collins, T. W.; Holmes, J. D.; Morris, M. A. Cyclical "Flipping" of Morphology in Block Copolymer Thin Films. *ACS Nano* **2011**, *5* (6), 4617–4623. https://doi.org/10.1021/nn2003629.

(42) Woodley, D. M.; Dam, C.; Lam, H.; LeCave, M.; Devanand, K.; Selser, J. C. Draining and Long-Ranged Interactions in the Poly(Ethylene Oxide)/Water Good Solvent System. *Macromolecules* **1992**, *25* (20), 5283–5286. https://doi.org/10.1021/ma00046a027.

(43) Rawolle, M.; Ruderer, M. A.; Prams, S. M.; Zhong, Q.; Magerl, D.; Perlich, J.; Roth, S. V.; Lellig, P.; Gutmann, J. S.; Müller-Buschbaum, P. Nanostructuring of Titania Thin Films by a Combination of Microfluidics and Block-Copolymer-Based Sol–Gel Templating. *Small* **2011**, *7* (7), 884–891. https://doi.org/10.1002/smll.201001734.

(44) Mahshid, S.; Askari, M.; Ghamsari, M. S. Synthesis of TiO_2 Nanoparticles by Hydrolysis and Peptization of Titanium Isopropoxide Solution. *Journal of Materials Processing Technology* **2007**, *189* (1–3), 296–300. https://doi.org/10.1016/j.jmatprotec.2007.01.040.

(45) Tsvetanov, C. B.; Stamenova, R.; Dotcheva, D.; Doytcheva, M.; Belcheva, N.; Smid, J. Intelligent Networks Based on Poly(Oxyethylene). *Macromolecular Symposia* **1998**, *128* (1), 165–182. https://doi.org/10.1002/masy.19981280117.

(46) Bullock, E. L.; Patthey, L.; Steinemann, S. G. Clean and Hydroxylated Rutile TiO_2(110) Surfaces Studied by X-Ray Photoelectron Spectroscopy. *Surface Science* **1996**, *352–354*, 504–510. https://doi.org/10.1016/0039-6028(95)01188-9.

(47) Briggs, D. Handbook of X-Ray Photoelectron Spectroscopy C. D. Wanger, W. M. Riggs, L. E. Davis, J. F. Moulder and G. E.Muilenberg Perkin-Elmer Corp., Physical Electronics Division, Eden Prairie, Minnesota, USA, 1979. 190 Pp. $195. *Surf. Interface Anal.* **1981**, *3* (4), v–v. https://doi.org/10.1002/sia.740030412.

(48) Liu, F.-M.; Wang, T.-M. Surface and Optical Properties of Nanocrystalline Anatase Titania Films Grown by Radio Frequency Reactive Magnetron Sputtering. *Applied Surface Science* **2002**, *195* (1–4), 284–290. https://doi.org/10.1016/S0169-4332(02)00569-X.

(49) Fuyuki, T.; Kobayashi, T.; Matsunami, H. Effects of Small Amount of Water on Physical and Electrical Properties of TiO_2 Films Deposited by CVD Method. *J. Electrochem. Soc.* **1988**, *135* (1), 248–250. https://doi.org/10.1149/1.2095566.

(50) Mathews, N. R.; Morales, E. R.; Cortés-Jacome, M. A.; Toledo Antonio, J. A. TiO_2 Thin Films - Influence of Annealing Temperature on Structural, Optical and Photocatalytic Properties. *Solar Energy* **2009**, *83* (9), 1499–1508. https://doi.org/10.1016/j.solener.2009.04.008.

(51) Ohsaka, T.; Izumi, F.; Fujiki, Y. Raman Spectrum of Anatase, TiO_2. *Journal of Raman Spectroscopy* **1978**, *7* (6), 321–324. https://doi.org/10.1002/jrs.1250070606.

(52) Zhang, J.; Li, M.; Feng, Z.; Chen, J.; Li, C. UV Raman Spectroscopic Study on TiO_2. I. Phase Transformation at the Surface and in the Bulk. *J. Phys. Chem. B* **2006**, *110* (2), 927–935. https://doi.org/10.1021/jp0552473.

3.7. Appendix

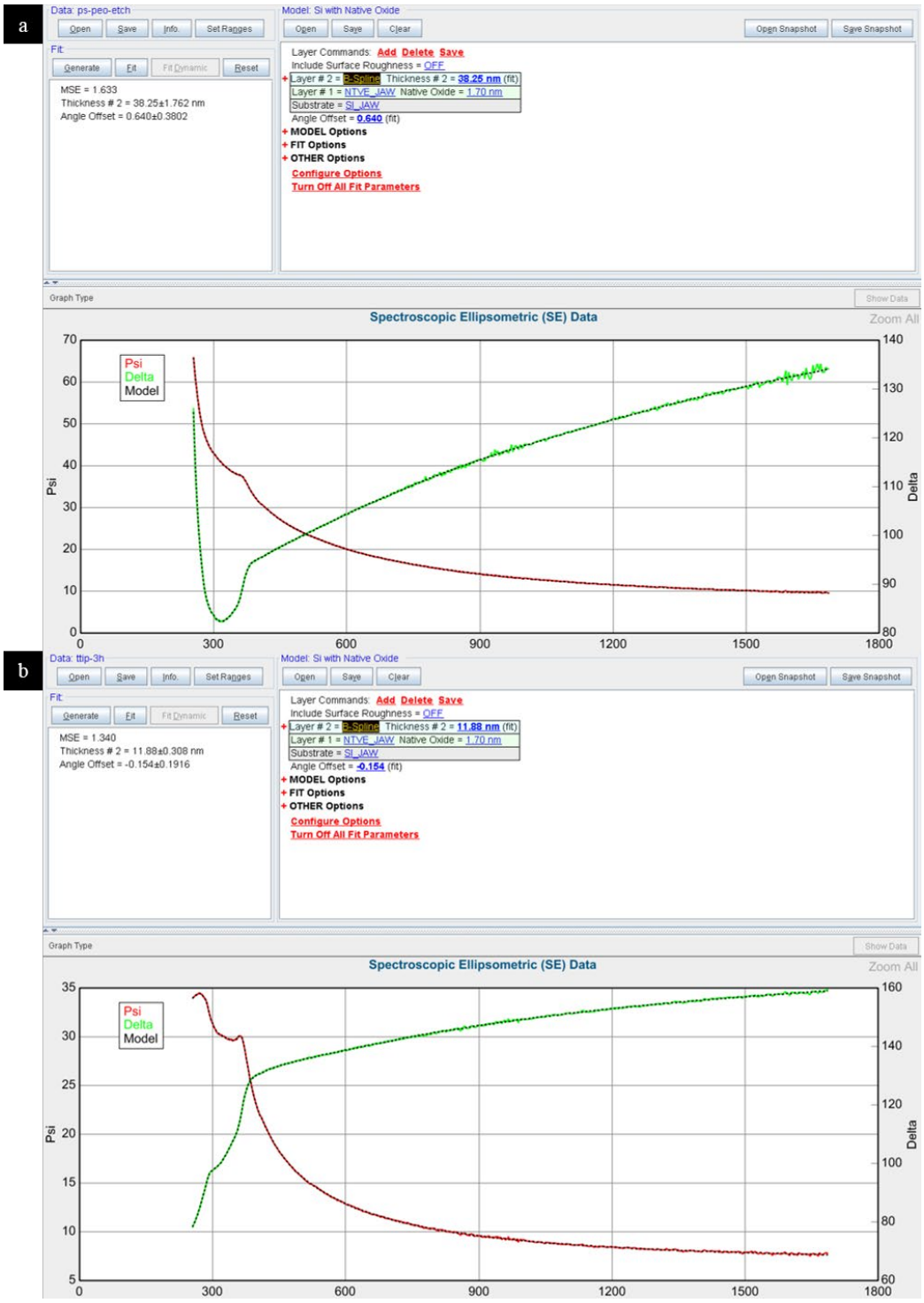

Figure S3-1. Spectroscopic Ellipsometric (SE) data giving the average thickness of (a) PS-*b*-PEO self-assemble thin film and (b) TiO_2 nanowires formed after 3 hours exposure to TTIP under ambient condition (ambient temperature, without control over relative humidity).

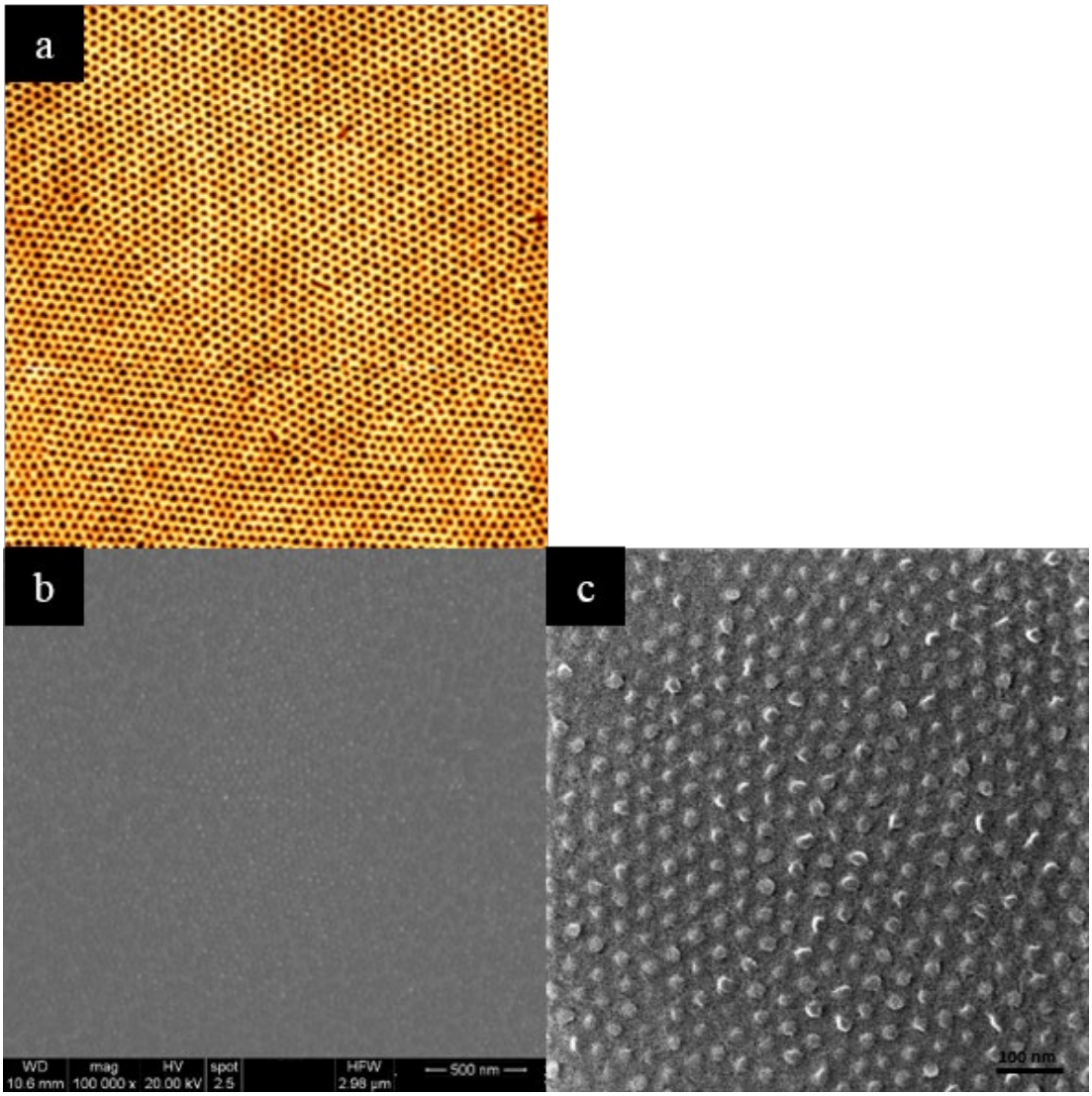

Figure S3-2. Vertical orientation perpendicular to the surface of (a) PEO domain within PS matrix as shown with AFM (2x2 µm), obtained after one hour and 30 minutes exposure to toluene vapours at 50 °C and (b,c) titanium dioxide nanodots obtained after 3 hours of exposure to TTIP and UV-O_3 treatment. (b) is obtained *via* SEM while (c) was imaged with a Helium Ion Microscope, HIM.

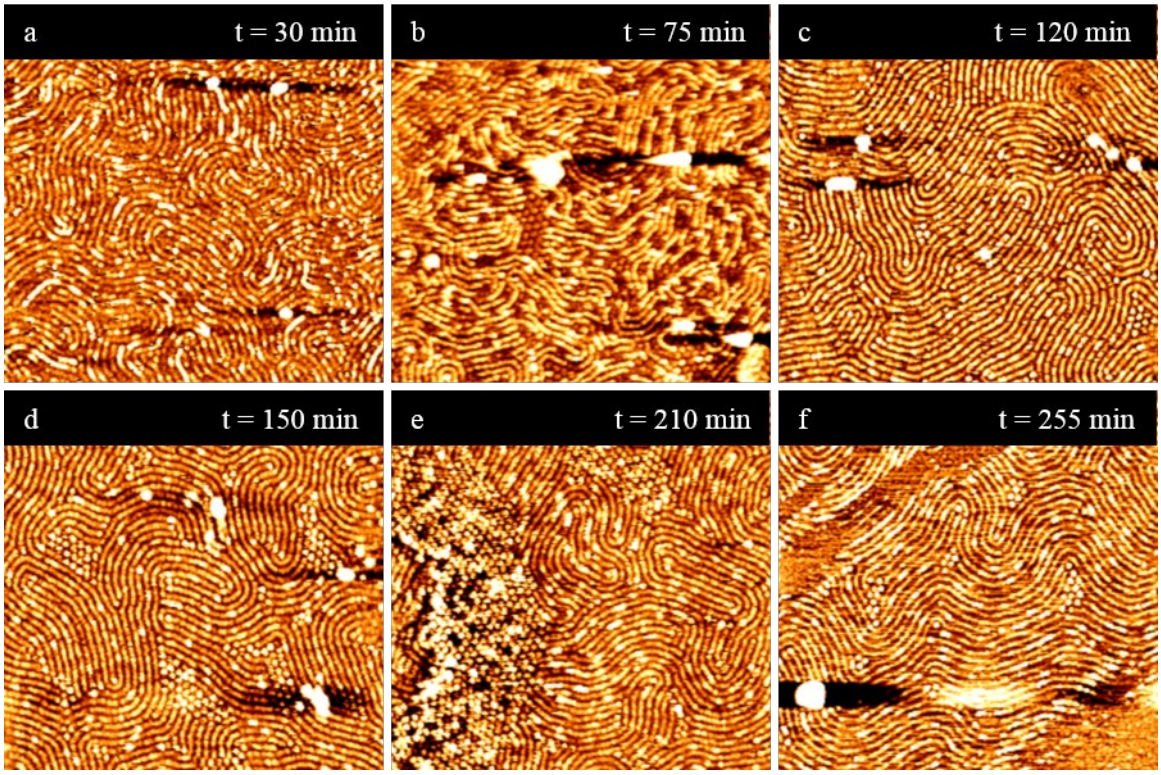

Figure S3-3. AFM images of titanium dioxide nanowires formed under ambient conditions (ambient temperature, without control over relative humidity) after exposure to TTIP vapours for (a) 30 min, (b) 75 min, (c) 120 min, (d) 150 min, (e) 210 min and (f) 255 min

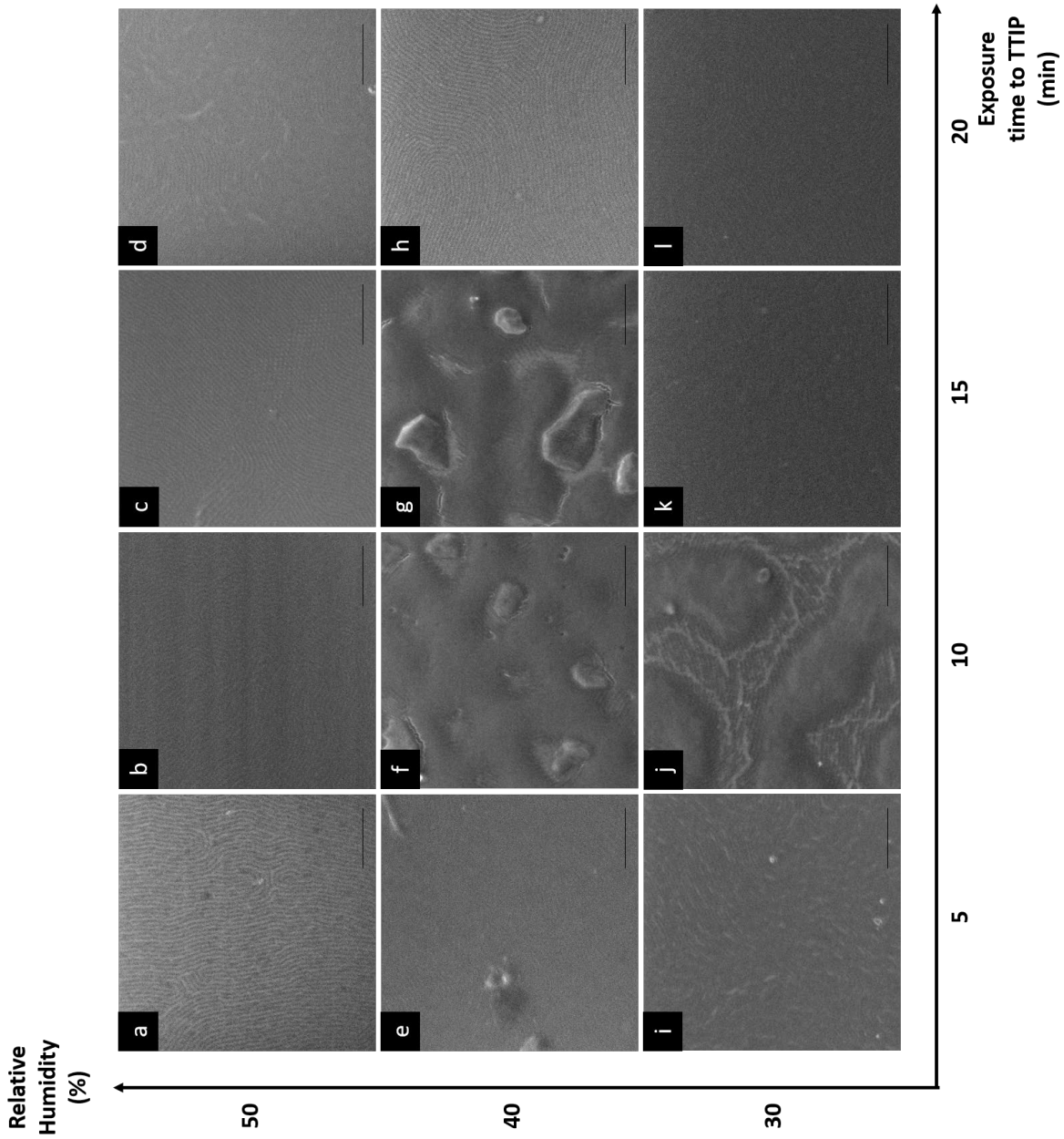

Figure S3-4. SEM images showing the evolution of formed titanium dioxide nanowires at 40 °C as a function of exposure time to TTIP (x-axis) and relative humidity (y-axis). The self-assemble BCP thin films were exposed to TTIP in 50% relative humidity for (a) 5 min, (b) 10 min, (c) 15 min and (d) 20 min ; in 40% relative humidity for (e) 5min, (f) 10 min, (g) 15 min, (h) 20 min ; in 30% relative humidity for (i) 5 min, (j) 10 min, (k) 15 min and (l) 20 min. All images were taken after a 3-hour UV-ozone treatment. All scale bars = 500 nm.

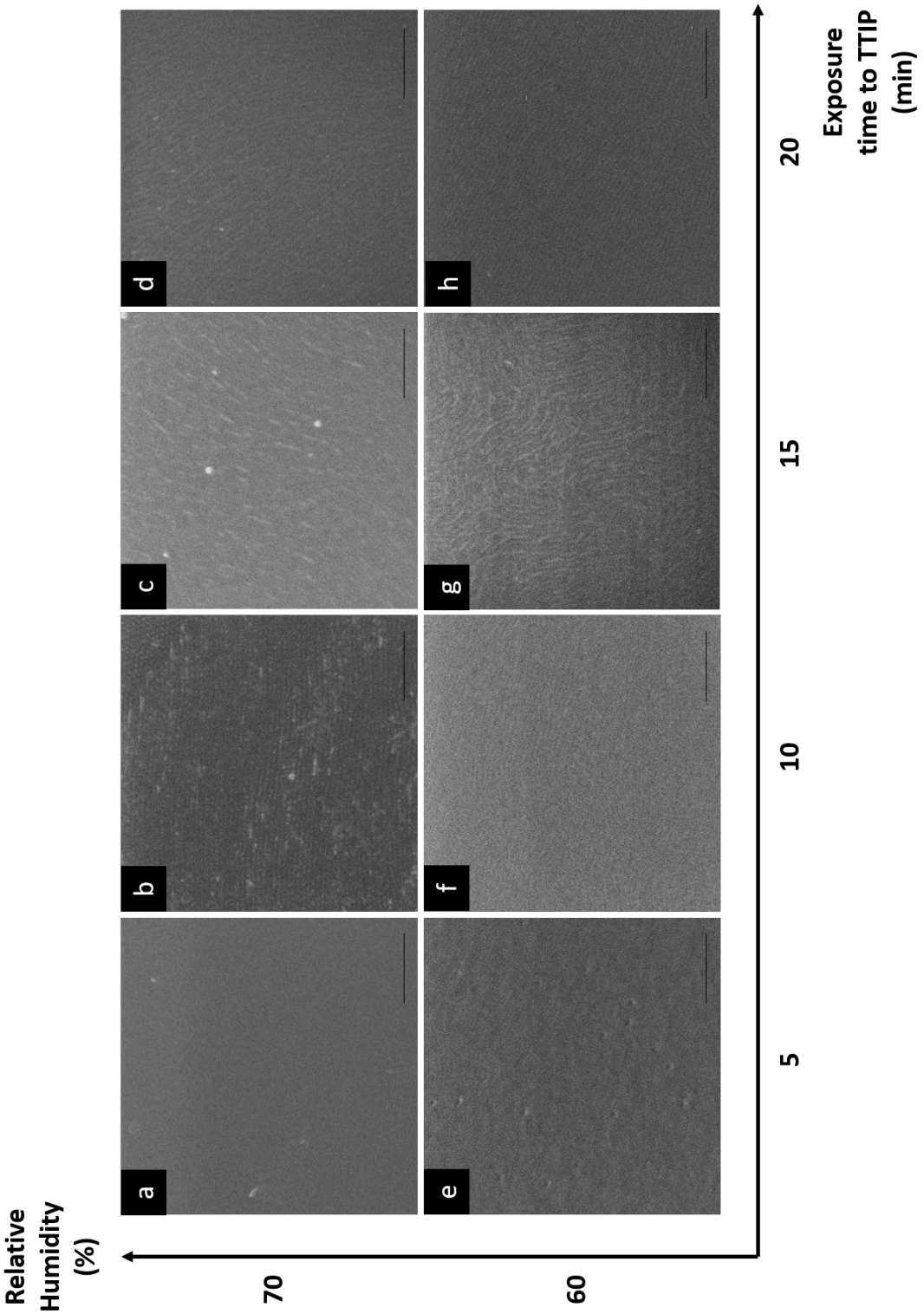

Figure S3-5. SEM images showing the evolution of formed titanium dioxide nanowires at 40 °C as a function of exposure time to TTIP (x-axis) and relative humidity (y-axis). The self-assemble BCP thin films were exposed to TTIP in 70% relative humidity for (a) 5 min, (b) 10 min, (c) 15 min and (d) 20 min and in 60% relative humidity for (e) 5min, (f) 10 min, (g) 15 min, (h) 20 min. All images were taken after a 3-hour UV-ozone treatment. All scale bars = 500 nm.

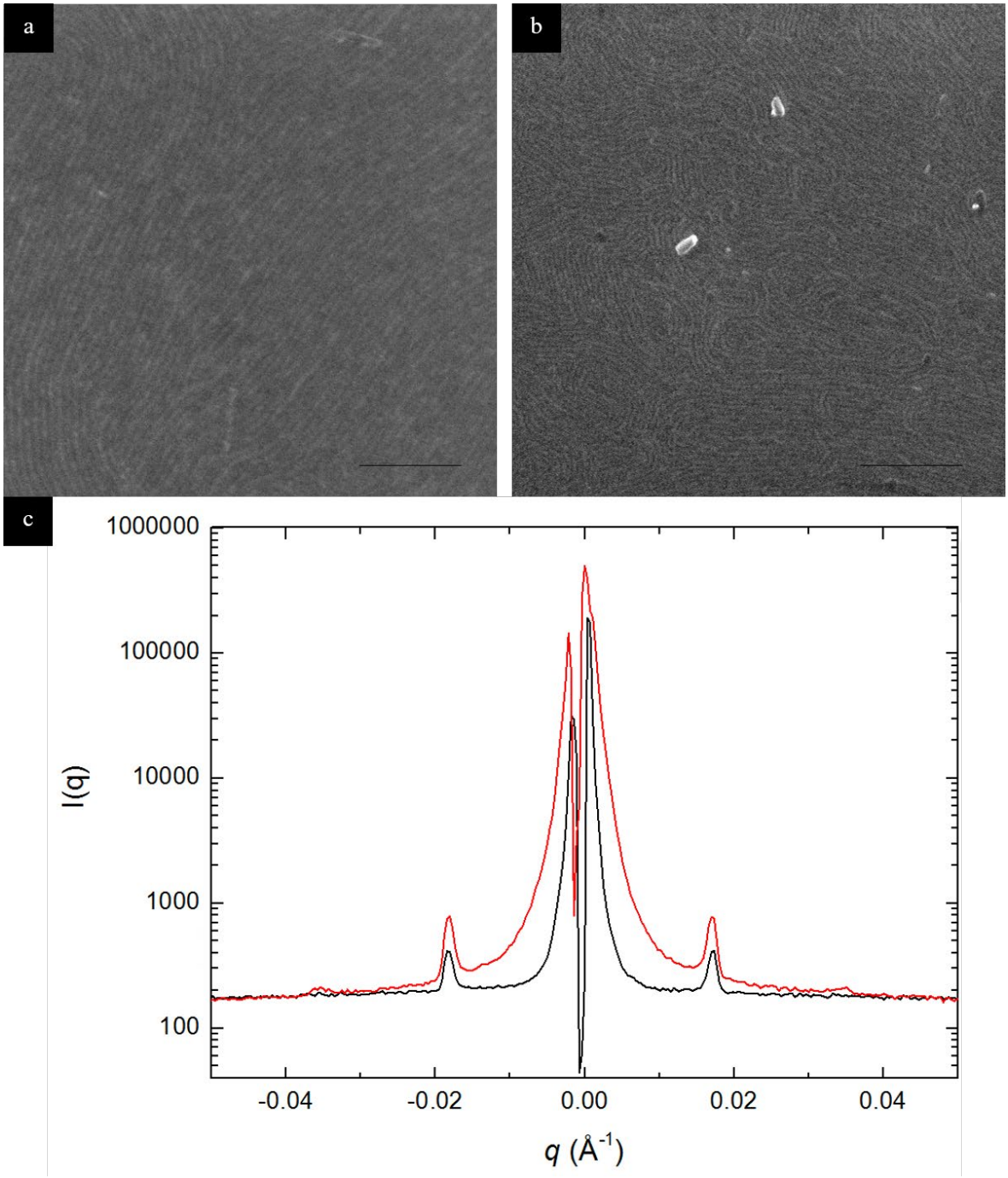

Figure S3-6. Titanium dioxide nanowires are formed at 30 °C after 20 minutes exposures to TTIP under a relative humidity of 50%. (a) and (b) are SEM characterization of the nanowires after UV-O_3 treatment and (a) before calcination (scale bar = 500 nm) and (b) after calcination at 800 °C for 2 hours (scale bar = 1 µm). The intensity profiles of the nanowires are presented in (c), as a function of q, where black line (lower line) is sample before calcination and red line (upper line) is the same after calcination.

Chapter 4

Formation of Europium-doped Gadolinium Oxide Phosphor Nanostructures via Salt Inclusion in Self-Assembled Block Copolymer Scaffold

4.1. Abstract

Europium-doped gadolinium oxide (Eu-doped Gd_2O_3) find applications in numerous luminescent applications, from bioprobes to phosphor storage, due to the nature of their *f-f* transitions resulting in fine and sharp emission peaks. In this chapter, we report the formation of Eu-doped Gd_2O_3 nanofeatures (*i.e.* nanodots or nanowires) by combining a bottom-up copolymer (BCP) templating process *via* thermo-solvent annealing, and the incorporation of inorganic materials in the hydrophilic block *via* a europium-gadolinium nitrate precursor solution. To study the effect of Eu^{2+} and Eu^{3+} dopant on the emission spectra, we studied a range of Eu:Gd ratio in the precursor solution, from 1:99 to 20:80. Structural characterization was performed mainly by atomic force microscopy (AFM) and scanning electron microscopy (SEM). Chemical composition was assessed by X-Ray photoelectron spectroscopy (XPS) and confirmed with absorption and emission spectroscopy. Both Eu^{2+} and Eu^{3+} ions are present in the Gd_2O_3 host, with the latter being the majority ion. Blue emission bands and red emission bands excited by 320 nm are attributed to Eu^{2+} and Eu^{3+} ions, respectively. Synthesized nanofeatures have a narrow size distribution (standard deviation of few nanometres), and their size is tuneable with the overall precursor solution, from 28.7 to 33.7 nm almost independently of the Eu:Gd ratio. This Eu:Gd ratio, however, yields increased intensity emission peak when increasing europium concentration. This study provides further application of block copolymers for the formation of doped-inorganic nanomaterials.

4.2. Introduction

Lanthanide(III)-doped oxides in inorganic phosphors materials have attracted a great deal of attention for potential luminescent applications due to the unique nature of *f-f* transitions, resulting in sharp photoluminescence (PL) spectra[1,2] with resistance to photobleaching (dye molecules) and photoblinking[3] (high photochemical stability). Additionally, lanthanide-doped nanomaterials have size-independent optical properties meaning the emission depends on the dopant ion(s), low toxicity and high chemical stability[4-6]. Their applications are numerous from biosensors to the possibility of up- and down-conversion PL due to their long-lived excited states[7-9]. Lanthanide ions like ytterbium (Yb), erbium (Er), samarium (Sm), dysprosium (Dy) and europium (Eu) or a mixture thereof have been used as dopant in a suitable host matrix, with Gd_2O_3 being one of the most common[10-13].

Among lanthanide ions, europium doped materials are of great interest. Europium ions can exist in both trivalent (Eu^{3+}) and divalent (Eu^{2+}) forms, with different optical properties. The electronic configuration[14] of Eu is [Xe]$4f^6 5d^0 6s^2$. Upon excitation, Eu^{3+} ion yield intense red emission, with a series of narrow bands distributed between 570 and 720 nm, and ascribed to $^5D_0 \rightarrow {}^7F_J$ transitions, where J = 0-4. Peak intensity is related to the ion environment, and to the symmetry of the host[15,16]. Narrow absorption and emission bands are either of pure magnetic (*e.g.* $^5D_0 \rightarrow {}^7F_1$) or pure electric (*e.g.* $^5D_0 \rightarrow {}^7F_2$) dipole moment origin[17]. However, upon excitation, Eu^{2+} yield intense blue emission due to the parity allowed $4f^6 5d^1 \rightarrow 4f^7$ ($^8S_{7/2}$). As such, the active electronic level is not shielded, and both position and peak of the emission band rely on the host material[18]. If most applications rely on a single colour emission, and hence on a single Eu-dopant in the host, coexistence of both oxidation states finds interest in the design of x-ray storage[1], or persistent phosphors[19].

Typical routes for the generation of Eu-doped gadolinium oxide include thermolysis[3], spray pyrolysis[20], hydrogen flame pyrolysis[21], combination of solid-state reaction and laser ablation in liquids[22] or microemulsion[23]. Pyrolysis and heat treatment are often associated with aggregation and enlarged size, that would not be suitable for biological application such as imaging or drug delivery[3] that require controlled narrow size and shape distribution.

Block-copolymers (BCP) thin films offer a facile strategy for the formation of numerous oxides, as they can act as a scaffold for inorganic incorporation[24,25]. A block-copolymer is a macromolecule consisting of two chemically incompatible polymer chains, linked covalently. The immiscibility of the polymer blocks leads to microphase separation, with domains ranging from sub-10 to 100 nm ; the presence of the covalent bond prevents macrophase separation. Microphase separation in thin films is achieved traditionally through an annealing process which can be achieved by thermal-, solvent- or thermo-solvent input[26,27]. Microphase separation leads to the formation of different morphology such as cylinders, spheres or lamellae structures. Hence, the use of BCPs offer a promising route to create nanofeature inorganic materials suitable for biological application with (i) uniformed shape and (ii) narrow size distribution. Different shapes, or morphologies, can be achieved for a given BCP after an annealing process. Although size distribution is narrow for a given BCP, it is possible to tune their diameter by using block copolymers with different molecular weights.

In this chapter, we adapt the block copolymer approach by utilising poly(styrene)-*block*-poly(ethylene oxide) (PS-*b*-PEO) block copolymers. Annealing process for different BCP yields perpendicular- or parallel orientation of the hydrophilic block in the PS matrix. Mixture of europium-gadolinium nitrate solutions are then used to infiltrate the hydrophilic block. After subsequent removal of the block copolymer scaffold, a one-to-one registration of the nanofeatures is visible between the inorganic Eu-doped Gd_2O_3 and the sacrificial PS-*b*-PEO template.

4.3. Experimental

Materials. Two cylinders forming PS-*b*-PEO block copolymers with total Mn = 53.5 kg.mol^{-1} with Mn_{PS} = 42 kg.mol^{-1} and Mn_{PEO} = 11.5 kg.mol^{-1} with a polydispersity of 1.07 (referred as SEO_{42K}) and total Mn = 43 kg.mol^{-1} with Mn_{PS} = 32 kg.mol^{-1} and Mn_{PEO} = 11 kg.mol^{-1} with polydispersity of 1.06 (referred as SEO_{32K}) were purchased from Polymer Source Inc. and used without any further purification. Highly polished single-crystal silicon <100> wafers (p-type) with a native oxide layer were purchased from Siltronix and used as a substrate without any attempt to remove the native layer (~ 2-5 nm). Toluene (CHROMASOLV Plus, for HPLC, ≥ 99.9 %), $Gd(NO_3)_3.6H_2O$ (gadolinium(III) nitrate hexahydrate) and $Eu(NO_3)_3.5H_2O$ (europium(III) nitrate pentahydrate) were purchased from Sigma-Aldrich and used without any further purification.

Film Processing and Oxide Formation. Silicon substrates were cleaned by ultrasonication in acetone and toluene for 20 minutes respectively and dried under a nitrogen stream. SEO_{42K} and SEO_{32K} were dissolved in toluene to yield a 1 wt% solution and left to stir overnight. Following complete dissolution, solutions were spin coated at 3000 rpm for 30 s (incl. 5 s ramp) using a SCS G33-8 spincoater. Spun cast SEO_{42K} and SEO_{32K} thin films were subsequently processed using solvent vapour annealing technique: SEO_{42K} were annealed in toluene vapours at 50 °C for 1 hours and SEO_{32K} were annealed in toluene vapours at 55 °C for 1 hour 30 minutes to obtain perpendicular or parallel orientation of PEO domains to the surface, respectively. Following microphase separation, the films were immersed in anhydrous ethanol to create an activated porous template (a) for 12 hours at 40 °C for SEO_{42K} films and (b) 17 minutes in an ultrasonication bath for SEO_{32K} films. This step allows the PEO domains to stretch without being etched (covalently bond to PS domains) in order to react more readily with the oxide precursors. The precursor uptake is increased. Mixtures of

gadolinium and europium nitrates were used as precursors to form Eu-doped Gd_2O_3 nanofeatures within the block copolymer templates. 0.4, 0.6, 1, 2, 5 and 10 wt% ethanolic solution of europium and gadolinium with different ratio of Eu:Gd (1:99, 5:95, 10:90, 15:85 and 20:80) were mixed and left stirring overnight to ensure complete dissolution. Precursor solutions were spin coated on "activated" SEO_{42K} and SEO_{32K} templates at 3200 rpm for 30 s (incl. a 5 s ramp). Films were subsequently treated in a UV-ozone system for a period of 3 hours (PSD Pro Series Digital UV Ozone System, Novascan Technologies, Inc.). The UV source consists of two low-pressure mercury vapour grid lamps, with a power of 65-100 W and an output current of 0.8-0.95 A. They have strong emission in the UV at wavelength 184.9 and 253.7 nm.

Characterization. Surface morphologies were analysed with and AFM (Park systems, XE-100 and XE-7) in tapping-mode (XE-100) and true non-contact mode (XE-7) using silicon microcantilever probe tips. Topographic, phase and amplitudes images were recorded simultaneously. Top-down scanning electron microscope (SEM) images were obtained by a high-resolution Field Emission Zeiss Ultra Plus-Scanning Electron microscope at an accelerating voltage of 2-5 kV. X-Ray photoelectron spectroscopy (XPS) was performed on VG Scientific ECSAlab Mk II system using Al Kα mono X-Ray source (1486.6eV), under ultra-high vacuum conditions. The analyser pass energy was set to 100 eV for survey spectra and 20 eV for core-level scans. Charge correction was set to 284.8 eV (C *1s* peak). To calculate the average diameter, over fifty measurements on three repeat samples were taken at random on the surface.

4.4. Results and Discussion

Block Copolymer Self Assembly by Thermo-Solvent Annealing.

Phase-separated BCP thin films can serve as a scaffold for the formation of inorganic nanostructures. In this study, we have selected a strongly segregated polymer system with an asymmetric structure, PS-*b*-PEO, and focused on two different molecular weights. In order to be suitable for the generation of ordered nanostructures, films were exposed to solvothermal annealing where combination of solvent vapour and heat improve long-range ordering.

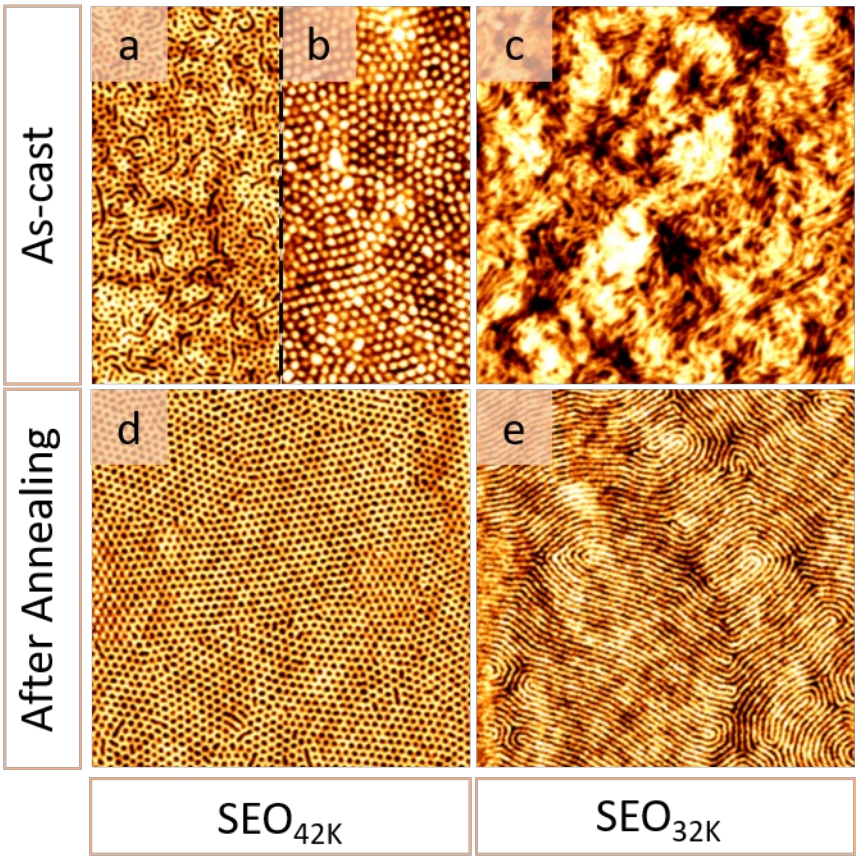

Figure 4-1. Morphology differences of PS-b-PEO thin films, SEO_{42K} and SEO_{32K}.Tapping mode AFM images for SEO_{42K} thin films (a-b) as cast and (d) after solvent vapour annealing in toluene at 50 °C for 1 hour at 10 RH, and for SEO_{32K} thin film (c) as cast and (e) after solvent vapour annealing in toluene at 55 °C for 1 hour and 30 minutes. All images are 2 x 2 μm.

Calculating the χ_{AB} polymer-solvent Flory-Huggins interaction parameters provides reasonable indication of miscibility between polymer and solvent; the parameter indicates good dissolution if smaller than 0.5. During solvent annealing, the solvent diffuses into the polymer enhancing chain mobility by creating free volume and allowing polymer chains to stretch and reorganize themselves. Toluene is proven to be a good solvent of PS domains, while air moisture from the annealing chamber is enough to induce the mobility of PEO chains. Flory-Huggins interaction parameters calculations are available in the supporting information. Applying heat to the system also helps with enhancing chains mobility as it increases the vapour pressure of the solvent and, hence, their diffusion into the polymer blocks.

Both SEO_{42K} and SEO_{32K} polymer thin films were fabricated via spin coating of a 1wt% toluene casting solution to produce highly ordered films. However, as-cast films show poorly

ordered features with (a) mixed orientation of PEO cylinders within a PS matrix and/or micellar arrangement for SEO_{42K} and (b) worm-like micelle structure for SEO_{32K} as presented in Figure 4-1 (a,b). To induce improve ordering, films were exposed to toluene vapours at 50 °C and 55 °C for SEO_{42K} and SEO_{32K} respectively. SEO_{42K} thin films exhibited $C_{\perp}$ arrangement PEO domains in PS matrix after 1-hour exposure to toluene vapours at 50°C, Figure 4-1 (c). Measured thickness was calculated at 48 nm. Perpendicular PEO domains have a 45 nm periodicity (L_0) close to the film thickness and a diameter of 26.4 (± 1.5) nm. Figure 4-1 (d) shows phase separated SEO_{32K} in a $C_{\parallel}$ arrangement of PEO domains within PS matrix, when thermo-solvent annealed at 55 °C for 1 hour 30 minutes. Periodicity L_0 was measured to be ~ 31nm, with PEO domain diameter of 22.3 (± 2.9) nm.

Initially, SEO_{42K} thin films were exposed to toluene vapours at 60 °C under the same experimental conditions exposed in Chapter 3. However, resulting samples presented either (i) a parallel orientation of PEO cylinders to the surface or (ii) some dewetting. In order to reproducibly produce phase separated block copolymer thin films, the annealing temperature was dropped to 50 °C to reduce dewetting and the annealing time was kept at 2 hours. Resulting morphologies were $C_{\perp}$ orientation of PEO domains within a PS matrix as seen in Figure 4-2 (c, f, and i). However, dewetting of the samples kept occurring. The exposure time to toluene vapour was reduced to 1 – 1.5 hour and the morphologies varied from one sample to another.

We hypothesised that there was an extra factor impacting on the solvent annealing, specifically the amount of water in the atmosphere. To reduce the uncertainties in the process, we decided to study the effect of the relative humidity in the process chamber on the morphologies as a function of the exposure time to toluene vapours at 50°C. Such an evolution is available in Figure 4-2. Results shown here were reproduced at least four times, and only important changes are reported.

At medium to high relative humidity, above 50 RH, morphologies were fluctuant depending on the exposure time to toluene vapours. Until 30 minutes, little to no modification of the surface morphology was observed as seen in Figure 4-2 (a). For exposure times between 30 minutes and 2 hours, the orientation of PEO cylinders was either (i) parallel, (ii) perpendicular to the surface or (iii) a mix thereof as seen in Figure 4-2 (b). As a result, the relative humidity was decreased to 40 RH, Figure 4-2 (d-f). Morphologies obtained under 2

hours of exposure to toluene vapours were proven by AFM to be perpendicular PEO cylinders. Unfortunately, the polymer thin film had a high roughness.

$C_{\perp}$ orientation of PEO domains within a PS matrix was obtained for exposure to toluene vapours at 50 °C, under an exposure time of 2 hours, and for low relative humidity (10 – 30 RH) as presented in Figure 4-2 (g-h). As a result, working at low RH allows for a more reproducible process.

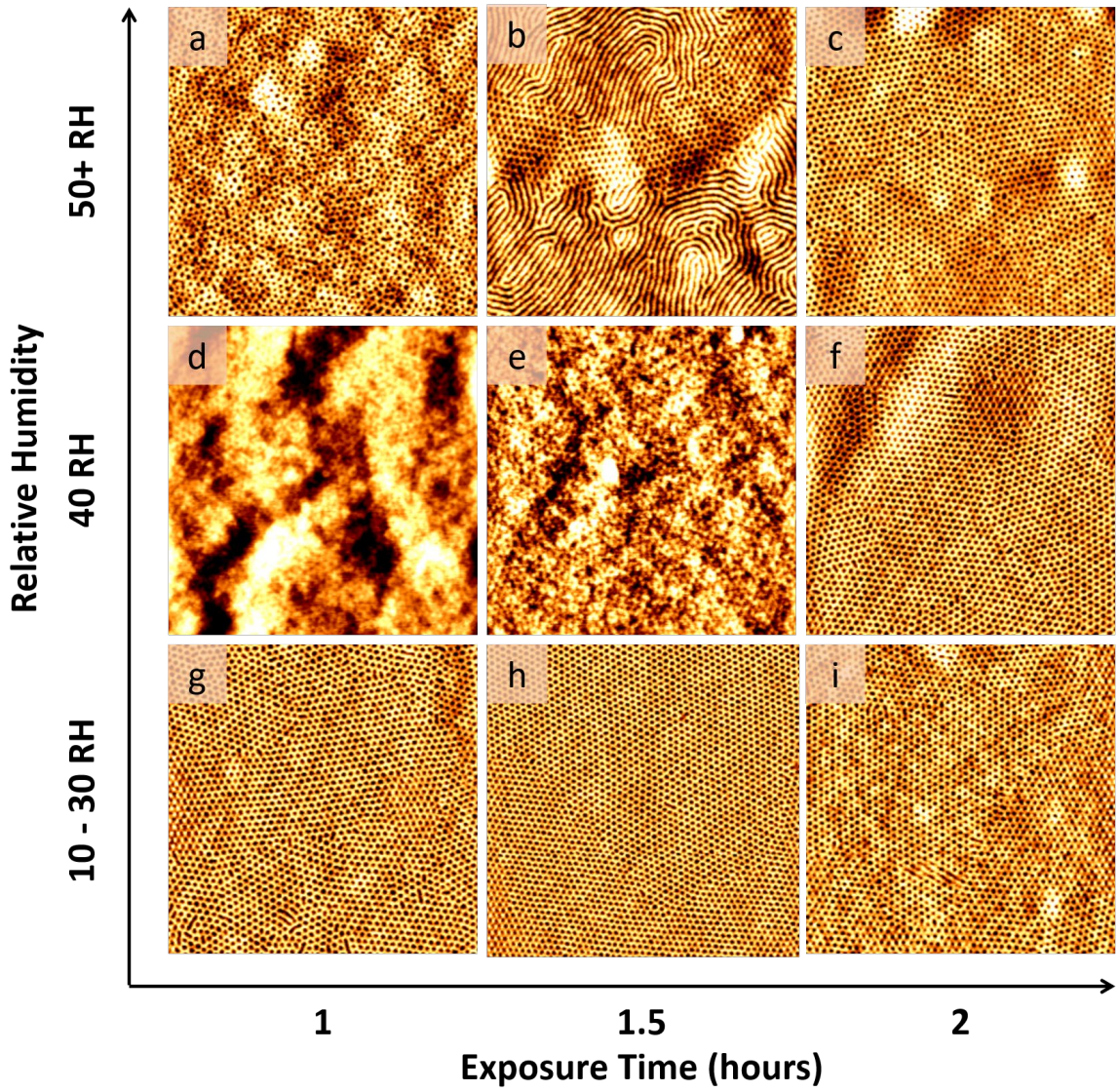

Figure 4-2. AFM matrix showing the evolution of phase separated SEO_{42K} thin films morphologies during the solvent annealing process at exposure time to toluene vapours (x-axis) and relative humidity (y-axis).

Block Copolymer Film Reconstruction with Anhydrous Ethanol.

To facilitate the incorporation of metal nanoparticles, surface reconstruction was performed on phase separated thin films. This is possible though the use of a solvent non-selective for the majority block, PS, but highly selective for the minority one, PEO – as determined by χ_{AB}, the Flory-Huggins interaction parameter. This process enhances the etching contrast between both PS and PEO blocks by swelling and/or etching PEO blocks, as well as facilitating metal inclusion. Both polymer films were immersed in anhydrous ethanol for 12 hours at 40 °C for SEO_{42K} and 17 minutes in an ultrasonication bath for SEO_{32K}. Over exposure of the films could lead to increased roughness and delamination of phase separated films as shown in Figure 4-3.

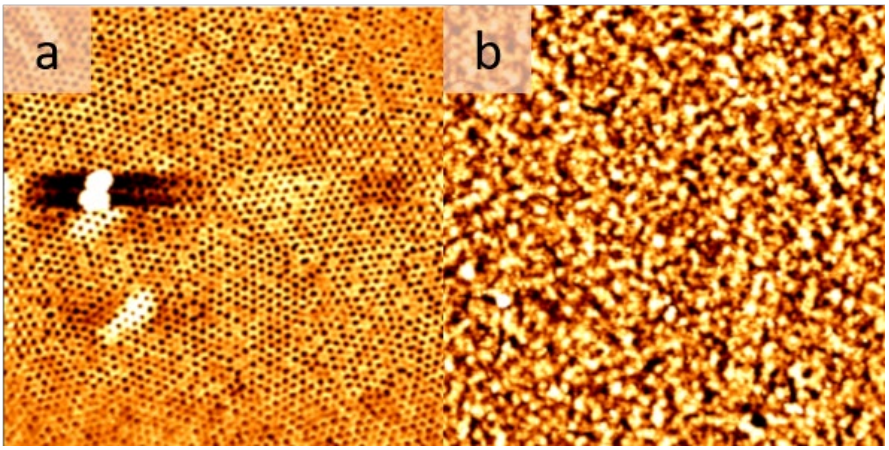

Figure 4-3. AFM images of "reconstructed' thin film in anhydrous ethanol at 40 °C for (a) 12 hours and (b) 17 hours showing increased roughness of the block copolymer thin film when immersed for too long.

Europium-doped Gadolinium Oxides Nanostructures Fabrication by Inclusion Technique.

To achieve the formation of europium-doped gadolinium oxide nanostructures, a europium-gadolinium nitrate solution was spun cast on the surface to fill the nanoporous 'ethanol reconstructed' structures. Metal deposition process is straight forward, and has been extensively studied by Ghoshal *et al*[28,29]. Following ion inclusion, UV ozone treatment was performed for a 3-hour period to ensure complete oxidation of the oxide(s) nanomaterial and to remove the organic polymer matrix. Evidence of inorganic material is provided in Figure

4-4 showing AFM topography and top-down SEM images of well-ordered structure with a one-to-one registration to the original BCP thin film.

Diameter of the nanodots shown in Figure 4-4 was measured to be 32.5 (± 4.5) nm. The measured average was calculated on three different samples, with at least 50 different measurements taken at random on the substrate. Calculated centre-to-centre distance of 44.7 (± 2.5) nm is in close agreement with the one from the SEO_{42K} phase separated thin film (45 nm), comforting the idea of a one-to-one registration with the BCP template. This distance was constant across all samples. On the contrary, the diameter of the nanodots can be manipulated by altering the initial concentration of the europium and gadolinium nitrate solution, see Figure S4-2 and Table S4-1. Higher concentration of nitrate solution leads to larger feature. Using BCPs provides a facile route to tune and tailor nanofeatures dimensions that would not be possible for other fabrication methods.

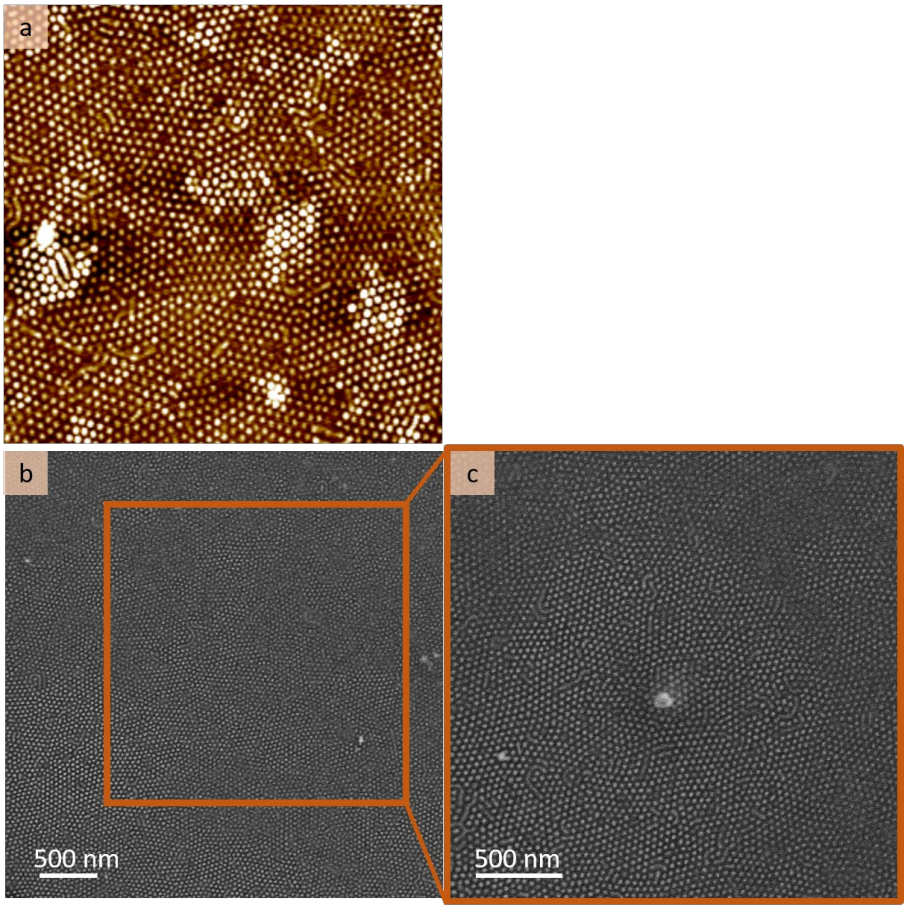

Figure 4-4. Evidence of inorganic europium-doped gadolinium nanodots, post UV ozone treatment for 3 hours on SEO_{42K} template. Nitrate solution: 5wt% precursor solution with 5:95 Eu:Gd. (a) Non-contact AFM topography image and (b-c) SEM image of the same sample at two different magnification. AFM image is a 2 x 2 µm.

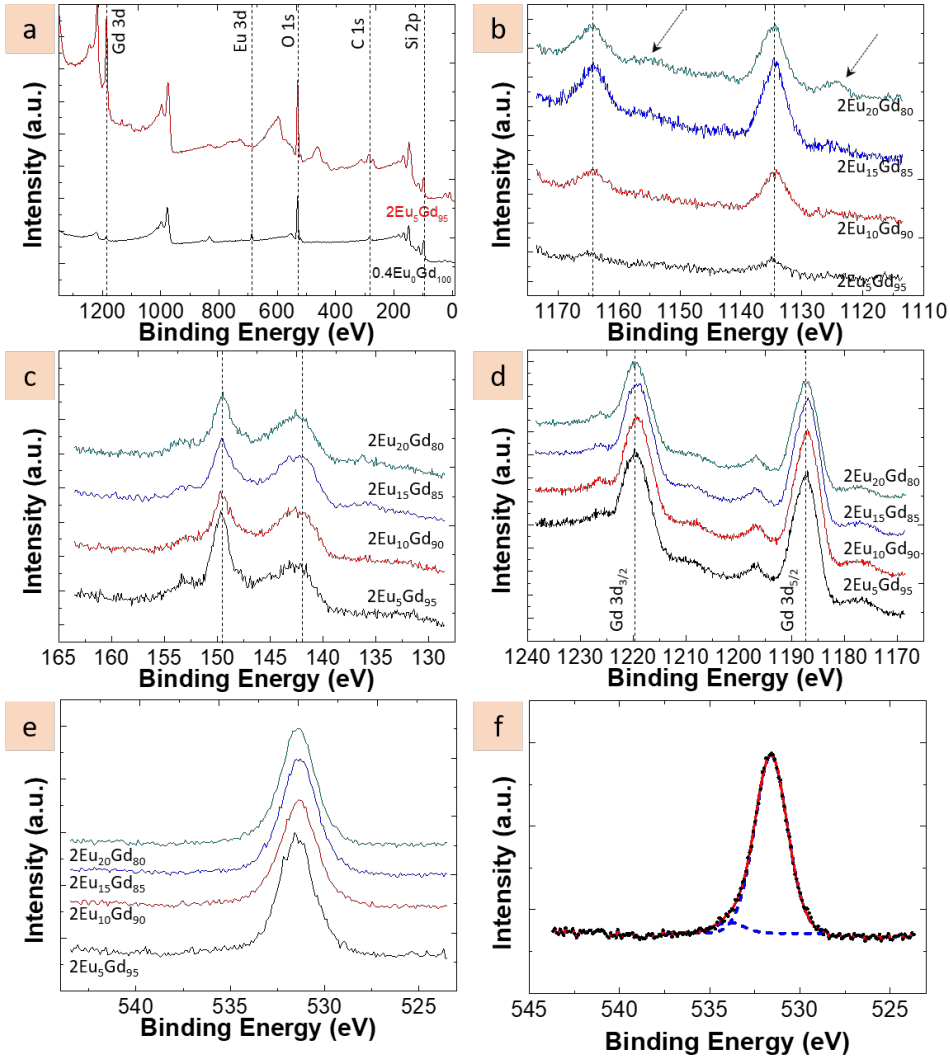

Figure 4-5. Evolution of chemical composition of Eu-doped Gadolinium Oxides $2Eu_xGd_y$ where x:y is the Eu:Gd ratio in a 2wt% nitrate solution. (a) Survey spectra of $2Eu_5Gd_{95}$ (top, red) and undoped $0.4Eu_0Gd_{100}$. Core level spectra of (b) Eu *3d*, (c) Eu 4d, Gd *4d* and Si *2s*, (d) Gd *3d* and (e) O *1s* for various $2Eu_xGd_y$ compositions. (f) core-level of O *1s* spectrum of $2Eu_{20}Gd_{80}$ and its deconvoluted peaks (blue, dash).

To better understand the processed nanofeatures, XPS was employed to examine the chemical composition and valence state of the elements in Eu-doped Gd oxide nanodots as shown in Figure 4-5 after a 3-hour UV ozone treatment. To compensate for charging effect, adventitious carbon C 1s was adjusted to 284.8 eV. Recorded surface survey showed the presence of expected elemental signals: Gd, Eu, Si, O and C as seen in Figure 4-5 (a). Binding energies located at 1164.5 eV and 1134.7 eV, Figure 4-5 (b), are ascribed to Eu^{3+} $3d_{3/2}$ and Eu^{3+} $3d_{5/2}$. Bands peaking at 1155.1 eV and 1124.6 eV (designated by a small

arrow) are consistent with Eu^{2+} $3d_{3/2}$ and Eu^{2+} $3d_{5/2}$ emerging gradually with increased doping of Eu^{3+} ions for a specific concentration of Eu-Gd mixture[30]. The increased relative intensity (peak area) of Eu^{2+} ions equally increases with the overall concentration of Eu-Gd nitrate solution, as more chemical elements are readily available to infiltrate the porous PEO structure. Interestingly, there is little to no evidence of Eu^{2+} ions for the 10 wt% nitrate solution. Data for Eu^{3+} and Eu^{2+} matches literature values[31-33]. This suggest trivalent and bivalent Eu ions co-exist in host Gd_2O_3.

Extensive Eu *4d* core level spectrum is often given to decipher between Eu^0, Eu^{2+} and Eu^{3+} contributions for a given europium-containing sample[34]. Elemental Eu *4d* is registered at 128.4 eV while binding energies[35,36,37] centred at 135.9 and 141.8 eV belonged to Eu^{3+}, 125 and 129 eV assigned to Eu^{2+}. However, due to system limitation, we could not decipher between oxidation states, as seen in Figure 4-5 (c). This spectrum shows two major peaks at 149.7 eV and 143.4 eV, evidencing the presence of gadolinium oxide[35,38,39] with Gd $4d_{3/2}$ and Gd $4d_{5/2}$ respectively. It is worth noting those two peaks are overlapping with Si *2s* peak, usually recorded at 149-152 eV and with Eu^{3+} *4d* peak, usually recorded around 136-142 eV as stated above. Contribution of Si *2s*, Eu *4d* and Gd *4d* would explain the asymmetric shapes of this core-level spectrum.

Further evidence of gadolinium is available in Figure 4-5 (d) in core level spectrum of Gd *3d*. Peaks at 1219.2 eV and 1187.1 eV are characteristic of spectra lines Gd $3d_{3/2}$ and Gd $3d_{5/2}$ of Gd_2O_3, respectively. Core level O *1s* spectrum, in Figure 4-5 (e), confirms the presence of Gd_2O_3 with an intense and fine peak at 531.5 eV associated with O^{2-} of the gadolinium (III) trioxide[40]. Note the O *1s* peak is lightly asymmetric with small deconvoluted peak at 533.9 eV attributed to O^{2-} species from the native oxide layer SiO_2 of the substrate[41], Figure 4-5 (f). Atomic percentage of C *1s* was quite high at ~16% for the lowest europium doping and europium-gadolinium nitrate solution concentration, reaching as high as ~32% for highest doping solutions. This suggests incomplete removal of the PS-*b*-PEO template. Longer exposure to UV ozone treatment and/or calcination of the sample might be required. All atomic percentage are available in Table S4-1.

Europium-doped Gadolinium Oxides Nanostructures Fabrication by Inclusion Technique.

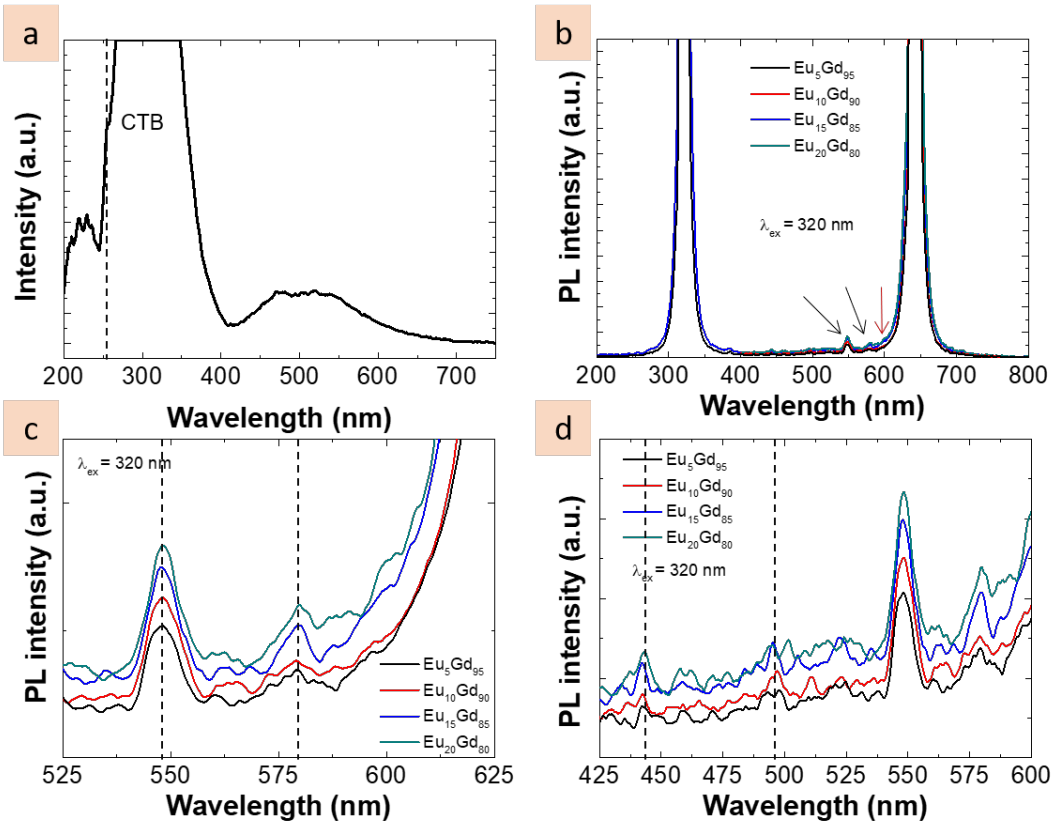

Figure 4-6. Absorption (a) and photoluminescence spectra (b-d) of europium-doped gadolinium oxide $10Eu_xGd_y$ where x:y is the Eu:Gd ratio in a 10wt% europium-gadolinium nitrate solution excited at 320 nm.

The optical properties of the europium-doped gadolinium nanodots were studied by absorption and emission spectroscopy. The absorption spectrum showed a strong saturated peak at ~ 254 nm, Figure 4-6 (a), arising as the charge transfer band[42,43] (CTB) between Eu^{3+} and O^{2-} species from Gd_2O_3. This peak is slightly visible on the left side of the large band at 245-408 nm, attributed to apparatus limitations. In addition, the excitation spectra exhibited a broad band between 415 nm and 575 nm where small peaks arise. Small line at 475 nm is due to the $^7F_0 \rightarrow {}^5D_2$ transition (*f-f* excitation lines of Eu^{3+}). This suggest the presence of Eu^{3+} in host Gd_2O_3. Presence of Eu^{2+} is usually evidenced by three peaks at ~253, 293 and 325 nm due to crystal field splitting[44] of Eu^{2+}. Unfortunately, absorption spectrum alone is not enough to conclude on the presence of Eu^{2+} ions.

Under excitation of 320 nm UV radiation, the sample exhibited few peaks in the 400-625 nm region, between two apparatus-saturated peaks at 325 and 625 nm, Figure 4-6 (b). Emission spectra exhibited two peaks, indicated by the black arrows ; close-up spectra are available in Figure 4-6 (c,d). The red arrow pointed out the hypersensitive $^5D_0 \rightarrow {}^7F_2$ transition of Eu^{3+} ions, usually observed at 610-619 nm due to electronic transitions[45,46]. However, because of limited spectra resolution, it was not possible to gain more information for *f-f* transition above 600 nm.

Close-up spectra in Figure 4-6 (c) consisted of two peaks (Stark components) at 548 and 579 nm ascribed to $^5D_1 \rightarrow {}^7F_2$ and $^5D_0 \rightarrow {}^7F_0$ transitions[47,48] of Eu^{3+}. The latter suggests Eu^{3+} ions are in a low symmetry environment without an inversion centre in Gd_2O_3 host[49]. Eu^{3+} ions could equally occupier higher symmetry environment, with inversion centre, at 597 nm assigned to $^5D_0 \rightarrow {}^7F_1$ transitions due to magnetic dipole[15]. The presence of characteristic emission peaks of Eu^{3+} suggests that the nanofeatures formed are partially crystalline at least, as the peaks are related to the crystal symmetry around the emissive ions. Lack of crystallinity (*i.e.* amorphous europium-doped gadolinium oxide) would give emission spectra without any peaks[50].

Other close-up spectra, Figure 4-6 (d), at lower wavelength exhibited peaks at 443 and 495 nm, although the low intensity of the second one could associate it with noise. The blue emission peak centred at 443 nm is attributed to the allowed electronic transition of $4f^6 5d^1$ to $4f^7$ of Eu^{2+} ions[51]. Altogether with XPS data, emission spectra of synthesized europium-doped gadolinium oxide confirm the presence of both Eu^{2+} and Eu^{3+} ions in Gd_2O_3 host, resulting blue and red emission respectively. The intensity of emission peaks can be related to the relative concentration of both ions: Eu^{3+} ions are the dominant oxidation state.

As expected, increasing concentration of europium in the europium-gadolinium nitrate solution lead to increased relative intensity of all Eu^{2+} and Eu^{3+} characteristic peaks.

4.5. Conclusion

A simple, generic and cost-effective route to the formation of Eu-doped Gd_2O_3 phosphor nanofeatures (*i.e.* nanodots and nanowires) has been demonstrated using self-assembled block copolymer thin film as a template. The nanodots have uniform size and shape, with a one-to-one registration to the block copolymer scaffold. The size of the nanodots can be

tuned by changing (i) the block copolymer molecular weight and volume fraction, and (ii) the concentration of precursor solutions (overall concentration of the europium-gadolinium mixture). The chemical composition was assessed by XPS and confirmed with absorption and emission spectroscopy at excitation wavelength of 320 nm.

Effect of Eu^{2+} and Eu^{3+} dopant on the emission spectra was thoroughly investigated by studying a range of Eu:Gd ratio (1:99 to 20:80) while increasing the overall Eu:Gd concentration of the nitrate solution. Emission spectra exhibit peaks characteristics of $^5D_1 \rightarrow {}^7F_2$ and $^5D_0 \rightarrow {}^7F_0$ transitions at 548 and 579 nm ascribed to Eu^{3+}. The hypersensitive $^5D_0 \rightarrow {}^7F_2$ transition usually visible at 619 nm is not present. It could be (i) shadowed by apparatus limitation or (ii) linked to the hypothetic lack of symmetry in the Eu^{3+} ion environment. The blue emission peak centred at 443 nm is attributed to the allowed electronic transition of $4f^6 5d^1$ to $4f^7$ of Eu^{2+} ions. However, peak intensity related to Eu^{2+} is significantly weaker compared to Eu^{3+}stating trivalent europium is the dominant oxidation state. All emission peaks show greater intensity with increased concentration of europium in Gd_2O_3 host, proving the doping effect of europium ion on the photoluminescent properties of Gd_2O_3:Eu.

4.6. References

(1) Ghodsi, V.; Layek, A.; Hegde, M.; Yildirim, B.; Radovanovic, P. V. Native Defects Determine Phase-Dependent Photoluminescence Behavior of Eu^{2+} and Eu^{3+} in In_2O_3 Nanocrystals. *Chem. Commun.* **2016**, *52* (23), 4353–4356. https://doi.org/10.1039/C6CC01122E.

(2) Ueda, J.; Matsuishi, S.; Tokunaga, T.; Tanabe, S. Preparation, Electronic Structure of Gadolinium Oxyhydride and Low-Energy 5d Excitation Band for Green Luminescence of Doped Tb^{3+} Ions. *J. Mater. Chem. C* **2018**, *6* (28), 7541–7548. https://doi.org/10.1039/C8TC01682H.

(3) Saha, A.; Mohanta, S. C.; Deka, K.; Deb, P.; Devi, P. S. Surface-Engineered Multifunctional Eu:Gd_2O_3 Nanoplates for Targeted and PH-Responsive Drug Delivery and Imaging Applications. *ACS Appl. Mater. Interfaces* **2017**, *9* (4), 4126–4141. https://doi.org/10.1021/acsami.6b12804.

(4) Gnach, A.; Bednarkiewicz, A. Lanthanide-Doped up-Converting Nanoparticles: Merits and Challenges. *Nano Today* **2012**, *7* (6), 532–563. https://doi.org/10.1016/j.nantod.2012.10.006.

(5) Liu, H.; Zhang, C.; Tan, Y.; Wang, J.; Wang, K.; Zhao, Y.; Jia, G.; Hou, Y.; Wang, S.; Zhang, J. Biodistribution and Toxicity Assessment of Europium-Doped Gd_2O_3 Nanotubes in Mice after Intraperitoneal Injection. *J Nanopart Res* **2014**, *16* (3), 2303. https://doi.org/10.1007/s11051-014-2303-8.

(6) Liu, Y.; Tu, D.; Zhu, H.; Chen, X. Lanthanide-Doped Luminescent Nanoprobes: Controlled Synthesis, Optical Spectroscopy, and Bioapplications. *Chem. Soc. Rev.* **2013**, *42* (16), 6924–6958. https://doi.org/10.1039/C3CS60060B.

(7) V. Eliseeva, S.; G. Bünzli, J.-C. Lanthanide Luminescence for Functional Materials and Bio-Sciences. *Chemical Society Reviews* **2010**, *39* (1), 189–227. https://doi.org/10.1039/B905604C.

(8) Wen, S.; Zhou, J.; Zheng, K.; Bednarkiewicz, A.; Liu, X.; Jin, D. Advances in Highly Doped Upconversion Nanoparticles. *Nat Commun* **2018**, *9* (1), 2415. https://doi.org/10.1038/s41467-018-04813-5.

(9) Zheng, W.; Huang, P.; Gong, Z.; Tu, D.; Xu, J.; Zou, Q.; Li, R.; You, W.; Bünzli, J.-C. G.; Chen, X. Near-Infrared-Triggered Photon Upconversion Tuning in All-Inorganic Cesium Lead Halide Perovskite Quantum Dots. *Nat Commun* **2018**, *9* (1), 3462. https://doi.org/10.1038/s41467-018-05947-2.

(10) Deng, H.; Chen, F.; Yang, C.; Chen, M.; Li, L.; Chen, D. Effect of Eu Doping Concentration on Fluorescence and Magnetic Resonance Imaging Properties of Gd_2O_3:Eu^{3+} Nanoparticles Used as Dual-Modal Contrast Agent. *Nanotechnology* **2018**, *29* (41), 415601. https://doi.org/10.1088/1361-6528/aad347.

(11) Wen, D.; Feng, J.; Li, J.; Shi, J.; Wu, M.; Su, Q. $K_2Ln(PO_4)(WO_4)$:Tb^{3+},Eu^{3+} (Ln = Y, Gd and Lu) Phosphors: Highly Efficient Pure Red and Tuneable Emission for White Light-Emitting Diodes. *J. Mater. Chem. C* **2015**, *3* (9), 2107–2114. https://doi.org/10.1039/C4TC02406K.

(12) Liu, Y.; Liu, G.; Dong, X.; Wang, J.; Yu, W. Tunable Photoluminescence and Magnetic Properties of Dy^{3+} and Eu^{3+} Doped $GdVO_4$ Multifunctional Phosphors. *Phys. Chem. Chem. Phys.* **2015**, *17* (40), 26638–26644. https://doi.org/10.1039/C5CP04373E.

(13) Qian, B.; Wang, D.; Wang, H.; Song, Y.; Zhou, X.; Sheng, Y. Solvothermal Synthesis of Columnar $Gd_2O_2S:Eu^{3+}$ and a Comparative Study with Columnar $Gd_2O_3:Eu^{3+}$. *J. Am. Ceram. Soc.* **2019**. https://doi.org/10.1111/jace.16747.

(14) Gao, G.; Reibstein, S.; Peng, M.; Wondraczek, L. Tunable Dual-Mode Photoluminescence from Nanocrystalline Eu-Doped Li_2ZnSiO_4 Glass Ceramic Phosphors. *J. Mater. Chem.* **2011**, *21* (9), 3156. https://doi.org/10.1039/c0jm03273e.

(15) Hussain, S.; Chen, X.; Harrison, W. T. A.; Ahmad, S.; Elsegood, M. R. J.; Khan, I. U.; Muhammad, S. Synthesis, Thermal, Structural Analyses, and Photoluminescent Properties of a New Family of Malonate-Containing Lanthanide(III) Coordination Polymers. *Front. Chem.* **2019**, *7*. https://doi.org/10.3389/fchem.2019.00260.

(16) Driesen, K.; Tikhomirov, V. K.; Görller-Walrand, C. Eu3+ as a Probe for Rare-Earth Dopant Site Structure in Nano-Glass-Ceramics. *Journal of Applied Physics* **2007**, *102* (2), 024312. https://doi.org/10.1063/1.2759195.

(17) Brito, H. F.; Malta, O. L.; Souza, L. R.; Menezes, J. F. S.; Carvalho, C. A. A. Luminescence of the Films of Europium (III) with Thenoyltrifluoroacetonate and Macrocyclics. **1999**, 5.

(18) Joshi, B.; Lee, S. W. Luminescence Properties of Eu^{2+}, Gd^{3+} and Pr^{3+} Doped Translucent Sialon Phosphors. *Journal of Rare Earths* **2015**, *33* (11), 1142–1147. https://doi.org/10.1016/S1002-0721(14)60538-X.

(19) Gingasu, D.; Mindru, I.; Ianculescu, A.; Preda, S.; Negrila, C.; Secu, M. Photoluminescence and Thermoluminescence Properties of the $Sr_3Al_2O_6:Eu^{3+}/Eu^{2+},Tb^{3+}$ Persistent Phosphor. *Journal of Luminescence* **2019**, *214*, 116540. https://doi.org/10.1016/j.jlumin.2019.116540.

(20) Nichkova, M.; Dosev, D.; Gee, S. J.; Hammock, B. D.; Kennedy, I. M. Microarray Immunoassay for Phenoxybenzoic Acid Using Polymer Encapsulated $Eu:Gd_2O_3$ Nanoparticles as Fluorescent Labels. *Analytical Chemistry* **2005**, *77* (21), 6864–6873.

(21) Goldys, E. M.; Drozdowicz-Tomsia, K.; Jinjun, S.; Dosev, D.; Kennedy, I. M.; Yatsunenko, S.; Godlewski, M. Optical Characterization of Eu-Doped and Undoped Gd_2O_3 Nanoparticles Synthesized by the Hydrogen Flame Pyrolysis Method. *J. Am. Chem. Soc.* **2006**, *128* (45), 14498–14505. https://doi.org/10.1021/ja0621602.

(22) Liu, J.; Tian, X.; Luo, N.; Yang, C.; Xiao, J.; Shao, Y.; Chen, X.; Yang, G.; Chen, D.; Li, L. Sub-10 Nm Monoclinic $Gd_2O_3:Eu^{3+}$ Nanoparticles as Dual-Modal Nanoprobes for Magnetic Resonance and Fluorescence Imaging. *Langmuir* **2014**, *30* (43), 13005–13013. https://doi.org/10.1021/la503228v.

(23) Wu, Y.; Xu, X.; Li, Q.; Yang, R.; Ding, H.; Xiao, Q. Synthesis of Bifunctional Gd_2O_3:Eu^{3+} Nanocrystals and Their Applications in Biomedical Imaging. *Journal of Rare Earths* **2015**, *33* (5), 529–534. https://doi.org/10.1016/S1002-0721(14)60452-X.

(24) Giraud, E. C.; Mokarian-Tabari, P.; Toolan, D. T. W.; Arnold, T.; Smith, A. J.; Howse, J. R.; Topham, P. D.; Morris, M. A. Highly Ordered Titanium Dioxide Nanostructures via a Simple One-Step Vapor-Inclusion Method in Block Copolymer Films. *ACS Appl. Nano Mater.* **2018**, *1* (7), 3426–3434. https://doi.org/10.1021/acsanm.8b00632.

(25) Cummins, C.; Ghoshal, T.; Holmes, J. D.; Morris, M. A. Strategies for Inorganic Incorporation Using Neat Block Copolymer Thin Films for Etch Mask Function and Nanotechnological Application. *Adv. Mater.* **2016**, *28* (27), 5586–5618. https://doi.org/10.1002/adma.201503432.

(26) Lundy, R.; Flynn, S. P.; Cummins, C.; Kelleher, S. M.; Collins, M. N.; Dalton, E.; Daniels, S.; Morris, M. A.; Enright, R. Controlled Solvent Vapor Annealing of a High χ Block Copolymer Thin Film. *Phys. Chem. Chem. Phys.* **2017**, *19* (4), 2805–2815. https://doi.org/10.1039/C6CP07633E.

(27) Sinturel, C.; Vayer, M.; Morris, M.; Hillmyer, M. A. Solvent Vapor Annealing of Block Polymer Thin Films. *Macromolecules* **2013**, *46* (14), 5399–5415. https://doi.org/10.1021/ma400735a.

(28) Ghoshal, T.; Shaw, M. T.; Bolger, C. T.; Holmes, J. D.; Morris, M. A. A General Method for Controlled Nanopatterning of Oxide Dots: A Microphase Separated Block Copolymer Platform. *J. Mater. Chem.* **2012**, *22* (24), 12083–12089. https://doi.org/10.1039/C2JM30468F.

(29) Ghoshal, T.; Fleming, P. G.; Holmes, J. D.; Morris, M. A. The Stability of "Ce2O3" Nanodots in Ambient Conditions: A Study Using Block Copolymer Templated Structures. *J. Mater. Chem.* **2012**, *22* (43), 22949–22957. https://doi.org/10.1039/C2JM35073D.

(30) Wang, Z.; Hou, X.; Liu, Y.; Hui, Z.; Huang, Z.; Fang, M.; Wu, X. Luminescence Properties and Energy Transfer Behavior of Colour-Tunable White-Emitting $Sr_4Al_{14}O_{25}$ Phosphors with Co-Doping of Eu^{2+}, Eu^{3+} and Mn^{4+}. *RSC Adv.* **2017**, *7* (83), 52995–53001. https://doi.org/10.1039/C7RA07970B.

(31) Yu, C.; Cao, M.; Yan, D.; Lou, S.; Xia, C.; Xuan, T.; Xie, R.-J.; Li, H. Synthesis of Eu^{2+}/Eu^{3+} Co-Doped Gallium Oxide Nanocrystals as a Full Colour Converter for White Light Emitting Diodes. *Journal of Colloid and Interface Science* **2018**, *530*, 52–57. https://doi.org/10.1016/j.jcis.2018.06.047.

(32) Dai, Q.; Foley, M. E.; Breshike, C. J.; Lita, A.; Strouse, G. F. Ligand-Passivated Eu:Y_2O_3 Nanocrystals as a Phosphor for White Light Emitting Diodes. *J. Am. Chem. Soc.* **2011**, *133* (39), 15475–15486. https://doi.org/10.1021/ja2039419.

(33) Gong, X.; Liu, Z.; Yan, D.; Zhao, H.; Li, N.; Zhang, X.; Du, Y. EuS–CdS and EuS–ZnS Heterostructured Nanocrystals Constructed by Co-Thermal Decomposition of Molecular Precursors

in the Solution Phase. *J. Mater. Chem. C* **2015**, *3* (16), 3902–3907. https://doi.org/10.1039/C5TC00312A.

(34) Li, Q.; Gong, C.; Cheng, X.; Zhang, Y. A Novel Polymer-Derived Method to Prepare Eu-Doped Si_3N_4 Yellow Phosphor. *Ceramics International* **2015**, *41* (3, Part A), 4227–4230. https://doi.org/10.1016/j.ceramint.2014.11.032.

(35) Wagner, C. D. The NIST X-Ray Photoelectron Spectroscopy (XPS) Database. 76.

(36) Sienkiewicz-Gromiuk, J.; Rusinek, I.; Kurach, Ł.; Rzączyńska, Z. Thermal and Spectroscopic (IR, XPS) Properties of Lanthanide(III) Benzene-1,3,5-Triacetate Complexes. *J Therm Anal Calorim* **2016**, *126* (1), 327–342. https://doi.org/10.1007/s10973-016-5521-8.

(37) Baltrus, J. P.; Keller, M. J. Rare Earth Oxides Eu_2O_3 and Nd_2O_3 Analyzed by XPS. *Surface Science Spectra* **2019**, *26* (1), 014001. https://doi.org/10.1116/1.5085768.

(38) Liu, J.; Tian, X.; Chen, H.; Shao, Y.; Yang, G.; Chen, D. Near-Infrared to Visible and near-Infrared Upconversion of Monoclinic Gd_2O_3:Yb^{3+}/Tm^{3+} Nanoparticles Prepared by Laser Ablation in Liquid for Fluorescence Imaging. *Applied Surface Science* **2015**, *348*, 60–65. https://doi.org/10.1016/j.apsusc.2014.11.105.

(39) Ge, W.; Liu, K.; Deng, S.; Shen, L.; Yang, P.; Liu, M.; Lu, Y. Modification of $Bi_6Fe_{1.9}Co_{0.1}Ti_3O_{18}$/$SiO_2$/$NaGdF_4$:$Yb^{3+}$,$Er^{3+}$ Nanocomposites with Different SiO_2 Thicknesses for Tunable Upconversion Luminescent and Ferromagnetic Properties. *CrystEngComm* **2019**, *21* (29), 4329–4339. https://doi.org/10.1039/C9CE00655A.

(40) Raiser, D.; Deville, J. P. Study of XPS Photoemission of Some Gadolinium Compounds. *Journal of Electron Spectroscopy and Related Phenomena* **1991**, *57* (1), 91–97. https://doi.org/10.1016/0368-2048(91)85016-M.

(41) Clarke, T. A.; Rizkalla, E. N. X-Ray Photoelectron Spectroscopy of Some Silicates. *Chemical Physics Letters* **1976**, *37* (3), 523–526. https://doi.org/10.1016/0009-2614(76)85029-4.

(42) Dorenbos, P. The Eu^{3+} Charge Transfer Energy and the Relation with the Band Gap of Compounds. *Journal of Luminescence* **2005**, *111* (1), 89–104. https://doi.org/10.1016/j.jlumin.2004.07.003.

(43) de Jesus, F. A.; Santos, S. T. S.; Caiut, J. M. A.; Sarmento, V. H. V. Effects of Thermal Treatment on the Structure and Luminescent Properties of Eu^{3+} Doped SiO_2–PMMA Hybrid Nanocomposites Prepared by a Sol–Gel Process. *Journal of Luminescence* **2016**, *170*, 588–593. https://doi.org/10.1016/j.jlumin.2015.05.030.

(44) Sahu, I. P.; Bisen, D. P.; Brahme, N.; Wanjari, L.; Tamrakar, R. Luminescence Properties of $Sr_2MgSi_2O_7$:Eu^{2+}, Ce^{3+} Phosphor by Solid State Reaction Method. *Physics Procedia* **2015**, *76*, 80–85. https://doi.org/10.1016/j.phpro.2015.10.015.

(45) Dhanaraj, J.; Jagannathan, R.; Kutty, T. R. N.; Lu, C.-H. Photoluminescence Characteristics of Y_2O_3:Eu^{3+} Nanophosphors Prepared Using Sol−Gel Thermolysis. *J. Phys. Chem. B* **2001**, *105* (45), 11098–11105. https://doi.org/10.1021/jp0119330.

(46) Liu, J.; Lian, H.; Shi, C. Improved Optical Photoluminescence by Charge Compensation in the Phosphor System $CaMoO_4:Eu^{3+}$. *Optical Materials* **2007**, *29* (12), 1591–1594. https://doi.org/10.1016/j.optmat.2006.06.021.

(47) Reddy, K. R.; Annapurna, K.; Buddhudu, S. Fluorescence Spectra of $Eu^{3+}:Ln_2O_2S$ (Ln = Y, La, Gd) Powder Phosphors. *Materials Research Bulletin* **1996**, *31* (11), 1355–1359. https://doi.org/10.1016/0025-5408(96)00129-8.

(48) S. Barbosa, C. D. E.; Luz, L. L. da; Almeida Paz, F. A.; L. Malta, O.; O. Rodrigues, M.; A. Júnior, S.; S. Ferreira, R. A.; D. Carlos, L. Site-Selective Eu(III) Spectroscopy of Highly Efficient Luminescent Mixed-Metal Pb(II)/Eu(III) Coordination Polymers. *RSC Advances* **2017**, *7* (10), 6093–6101. https://doi.org/10.1039/C6RA27850G.

(49) Nascimento, J. F. S. do; Araújo, A. M. U. de; Kulesza, J.; Monteiro, A. F. de F.; Júnior, S. A.; Barros, B. S. Solid-State Tunable Photoluminescence in Gadolinium-Organic Frameworks: Effects of the Eu^{3+} Content and Co-Doping with Tb^{3+}. *New J. Chem.* **2018**, *42* (7), 5514–5522. https://doi.org/10.1039/C7NJ04625A.

(50) Wawrzynczyk, D.; Samoć, M.; Nyk, M. Controlled Synthesis of Luminescent $Gd_2O_3:Eu^{3+}$ Nanoparticles by Alkali Ion Doping. *CrystEngComm* **2015**, *17* (9), 1997–2003. https://doi.org/10.1039/C4CE02500H.

(51) Xiao, W.; Zhang, X.; Hao, Z.; Pan, G.-H.; Luo, Y.; Zhang, L.; Zhang, J. Blue-Emitting $K_2Al_2B_2O_7:Eu(^{2+})$ Phosphor with High Thermal Stability and High Color Purity for near-UV-Pumped White Light-Emitting Diodes. *Inorganic chemistry* **2015**, *54* (7), 3189–3195. https://doi.org/10.1021/ic502773t.

4.7. Appendix

Formation of a different morphology of europium-doped gadolinium oxide obtained on SEO_{32K} phase-separated block copolymer thin films: Figure S4-1

Figure S4-1 shows the possibility of forming Eu-doped gadolinium nanowires using SEO_{32K} as a scaffold. As seen with Figure S4-1 (a-b) there is a one-to-one registration between the microphase-separated template obtained *via* thermo-solvent annealing (a) and the post 3-hour UV ozone treatment obtained after spin coating a 0.6 wt % europium-gadolinium nitrate precursor solution with a 1:99 Eu:Gd ratio (b). Figure S4-1 (c) and (d) represent the surface survey of the sample and the core-level spectra of Gd *3d,* respectively. The survey spectra show expected elemental peaks: Gd *3d,* Eu *3d,* O *1s,* C *1s* and Si *2p*. Corresponding Gd *3d* atomic percentage was 0.08 %, and although a small Eu *3d* peak is visible on the survey, no quantitative data nor core-level Eu *3d* spectrum could be obtained. The core-level spectrum of Gd *4d* is available is Figure S4-1**,** with peaks at 156 eV, 153 eV and 150 eV attributed to Si *2s,* Gd *4d* and Eu *4d* respectively. These binding energies differ slightly from the ones observed in Figure 4-5 as the adventitious carbon peak was assigned to a higher value, 285.6 eV.

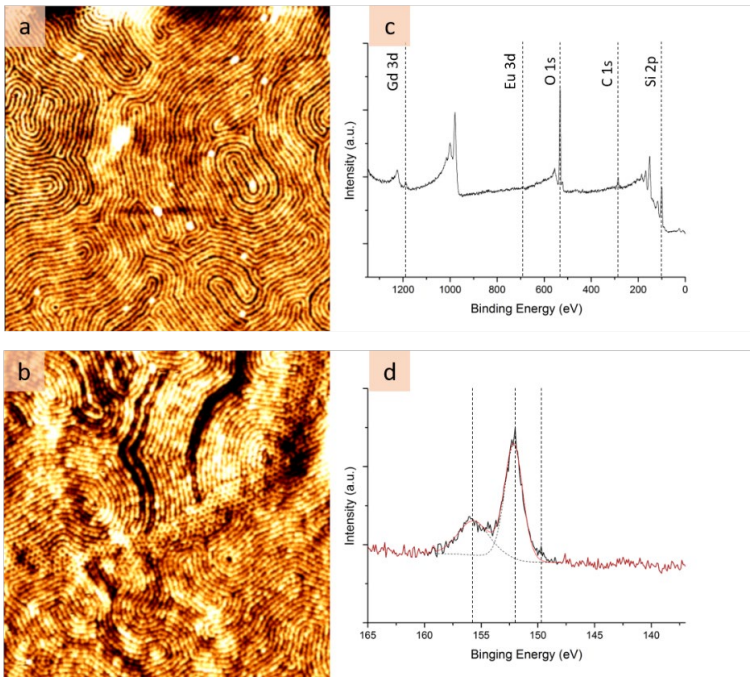

Figure S4-1. Application of the process to form Eu-doped Gd nanowires with AFM images of (a) phase-separated BCP film and (b) corresponding nanofeatures after UV ozone treatment. Chemical composition assessed by XPS with (c) surface survey and (d) Gd *4d,* Eu *4d* and Si *2s* core-level spectrum.

Evolution of europium-doped gadolinium oxide nanodots obtained on SEO_{42K} phase-separated block copolymer thin films after a 3-hour UV ozone treatment for different europium-gadolinium solution concentrations and for different europium-gadolinium ratio: Figure S4-2 and Table S4-1.

Figure S4-2 shows the evolution of nanodots size when increasing the concentration of precursor europium-gadolinium nitrate solutions : higher concentration leads to bigger nanodots diameters, although the centre-to-centre distance remains constant. This suggests varying the nitrate solution concentration can alter the diameter by a few nanometres (~ 28.7 nm to ~ 33.2 nm, as seen in Table S4-1). Because of the nature of the process, drastic changes of diameter could be obtained by using another favourable block-copolymer with a different chemistry and/or molecular weights. For example, Chapter 3 of this thesis showed PS-*b*-P4VP block copolymers were also suitable for infiltration of inorganic material into P4VP domains, yielding nanostructured oxides. Another alternative would be to change the molecular weight of the block copolymer: higher molecular weight would of PEO in a cylinder-forming PS-*b*-PEO would yield larger PEO domains and, hence, diameter of the resulting oxide.

Table S4-1 summarizes the average atomic concentration of the elements present on the substrate surface, as determined by XPS and deconvolution using CasaXPS software. The '*%Eu (XPS)*' register the percentage of europium compared to a europium-gadolinium mixture, calculated with XPS data. This is to compare with the actual Eu:Gd ratio present in the nitrate precursor solution, as presented in the '*%Eu (sol)*'.

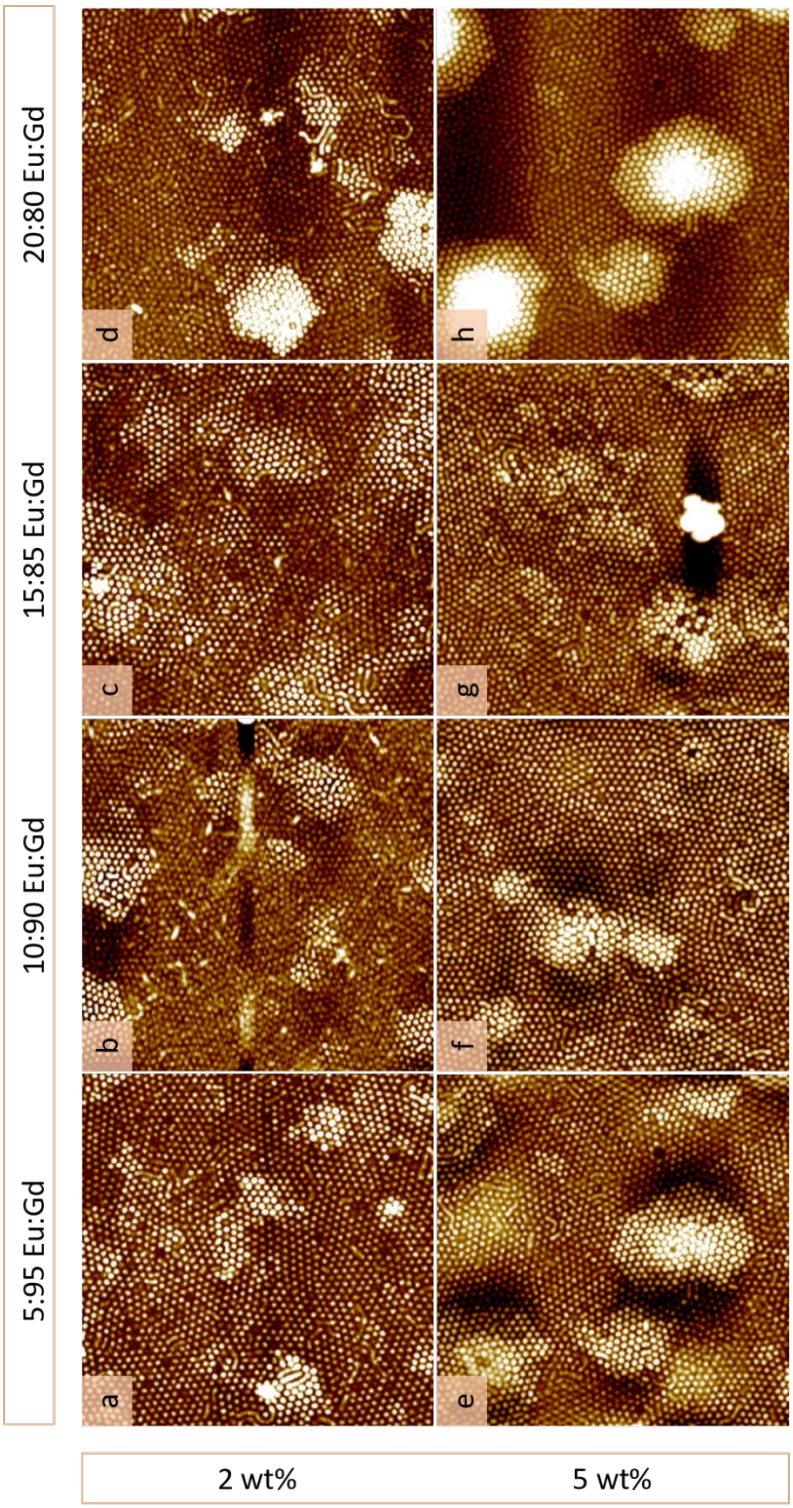

Figure S4-2. Topographic AFM images of europium-doped gadolinium after 3-hour UV ozone treatment with (a-d) 2 wt% and (e-h) 5 wt% europium-gadolinium nitrate solution, for different ratio Eu:Gd.

Sample Charac.		Atomic Concentration (%)							Diameter Ø (nm)			
	Name	O *1s*	C *1s*	Si *2p*	Gd *3d*	Eu *3d*	%Eu (XPS)	%Eu (sol)	mean	SD	min	max
1 wt%	$1Eu_5Gd_{95}$	43.48	15.94	38.66	1.85	0.07	3.6	5.1				
	$1Eu_{10}Gd_{90}$	40.45	17.71	40.20	1.47	0.17	10.4	9.8				
	$1Eu_{15}Gd_{85}$	39.79	23.52	35.86	1.60	0.22	12.1	11.4				
	$1Eu_{20}Gd_{80}$	39.53	26.85	31.41	1.74	0.47	21.3	19.7				
2 wt%	$2Eu_5Gd_{95}$	41.86	20.54	35.69	1.83	0.08	4.2	5.2	28.70	3.38	22.15	36.37
	$2Eu_{10}Gd_{90}$	48.12	18.68	30.65	2.29	0.26	10.2	10.0	29.39	2.39	24.82	33.83
	$2Eu_{15}Gd_{85}$	49.13	21.43	26.28	2.20	0.56	20.3	14.4	30.20	1.65	27.14	33.20
	$2Eu_{20}Gd_{80}$	46.32	19.13	32.23	1.83	0.48	20.8	19.7	32.50	2.94	28.09	38.09
5 wt%	$5Eu_5Gd_{95}$	48.92	29.45	19.12	2.38	0.13	5.2	5.0	32.71	3.10	25.65	38.00
	$5Eu_{10}Gd_{90}$	50.03	23.91	23.62	2.19	0.25	10.2	9.4	33.83	2.44	28.65	37.92
	$5Eu_{15}Gd_{85}$	49.09	23.11	25.19	2.25	0.37	14.1	15.0	33.91	2.85	28.39	40.52
	$5Eu_{20}Gd_{80}$	45.59	31.68	20.18	2.02	0.54	21.1	20.1	33.71*	2.96	27.68	40.18
10 wt%	$10Eu_5Gd_{95}$	50.38	37.44	9.82	2.19	0.17	7.2	4.8	33.23	2.72	26.34	38.67
	$10Eu_{10}Gd_{90}$	49.64	31.10	16.89	2.12	0.25	10.5	9.0				
	$10Eu_{15}Gd_{85}$	54.57	32.18	10.72	2.18	0.35	13.8	15.1				
	$10Eu_{20}Gd_{80}$	51.67	32.17	13.34	2.19	0.63	22.3	19.5				

Table S4-1. Atomic percentage of element as determined by XPS, Eu:Gd ratio (referred as %Eu) obtained from XPS and from experiment, and average diameters of nanofeatures calculated on 3 different samples and with 50+ distinct measurements.

Chapter 5

Conclusions and Future Work

5.1 Conclusions and Future Work

Block copolymers have a wide range of potential applications in nanoscale fabrication due to their tuneable feature size, scalability and formation of well-ordered patterns. Their propensity to phase separate make them ideal candidates in the production of the next generation of electronic devices. Namely, they are a viable alternative to lithographic process due to their 'bottom-up' approach, and ability to access sub-10 nm features. Other advantages of BCP patterns include (i) low cost, (ii) high density and (iii) possibility of patterning a large surface. However, BCP integration to the manufacturing process is facing roadblocks such as defect densities, and formation of large phase-separated surfaces.

In Chapter 2, the phase separation of block copolymer was explored using an unconventional plasma treatment. During exposure to Ar^+ ion bombardment, there is a balance between self-assembly and possible damage and/or etching of the first few nanometres of the surface. The energy provided by the argon plasma during mild process (low RF power and argon flow) is sufficient to overcome the energy barrier to drive surface rearrangement and subsequent microphase separation. Observed nanofeatures were parallel and perpendicular arrangement of the BCP microdomains to the surface. The surface rearrangement could be due to three distinct phenomena, namely (i) heat gradient between the surface of the film and the substrate, (ii) active reorganisation and (iii) etching of the surface. Although, little etching was observed during this process. Recent advances of plasma treatment with block copolymer suggested the use of filter plasma to reduce physical bombardment of the surface by Ar^+ ion and surface modification by VUV-UV[1]. Further experiment with a filter plasma could help determining the process behind surface rearrangement and possibly reduce the induced damage to obtain a larger process window.

Chapter 3 highlighted a simple and effective processing route to yield titanium dioxide nanostructures using a CVD- and evaporation-based method. This route utilises the amphiphilic properties of the block copolymer film and the volatility of the precursor to form inorganic nanostructures. The process presented herein is suitable for selective deposition at low temperature and a safe environment to produce a large variety of oxides. Although those data were not presented in this thesis, this evaporation-based process can also yield hafnium dioxide, tungsten oxide and mixtures of titanium dioxide and vanadium oxide nanostructures *via* selective inclusion in PS-*b*-PEO and PS-*b*-P4VP films.

Chapter 4 detailed the formation of europium-doped gadolinium oxide *via* a liquid-phase approach. Ghoshal *et al.* spin-coating method[2,3] of salt precursor solution was utilised for the generation of nanodots with a diameter ranging from 27 to 33 nm depending on the concentration of the precursor solution. The formed nanostructures exhibit characteristic photoluminescent peaks attributed to Eu^{2+} and Eu^{3+} ion. Relative intensity of the peaks proves that the incorporation of europium in Gd_2O_3 is mainly in its trivalent state. Although some application requires single colour emission, the coexistence of both oxidation states can find applications in designing x-ray storage phosphors or multiplexed imaging[4]. If a single colour emission is required, this can be done by (i) reducing Eu^{3+} to Eu^{2+} in a reducing atmosphere in order to work with the bivalent cation Eu^{2+} or by (ii) using small Eu:Gd ratio as the quantity of Eu^{2+} ions increases with its relative concentration, in order to work with the trivalent cation Eu^{3+}. Additionally, the peak intensity increases with the europium concentration in a given precursor solution. Finally, the emission spectra of formed nanofeatures emphasises the lack of symmetry[5,6] in the material surrounding europium (Eu^{3+} and *f-f* transitions provides information on the presence of an inversion centre with the $^5D_0 \rightarrow {}^7F_2$ transition or lack thereof with the $^5D_0 \rightarrow {}^7F_1$ transition) and possibly lack of crystallinity. In future work, extra annealing (calcination) is required to study its effect on the photoluminescent properties.

Whilst this thesis has documented the phase separation of block copolymer thin films, many challenges exist, and other annealing process are being developed as alternative to traditional thermal and solvent vapour annealing such as microwave-assisted annealing or laser-assisted annealing. Additionally, new metrology technique will need to be developed to characterise and inspect the films for sub-10 nm as current microscopy technique does not have sufficient resolution. This thesis also documented alternatives to the selective infiltration *via* the use of an evaporation-based method. Finally, formed nanostructures could find application in various areas such as photovoltaics (titanium dioxide) or biosensing (europium-doped gadolinium) proving other industries than the microelectronics could benefit from the miniaturisation and the propensity of block copolymer to self-assemble in various nanostructured morphologies.

5.2 References

(1) Oh, J.; Suh, H. S.; Ko, Y.; Nah, Y.; Lee, J.-C.; Yeom, B.; Char, K.; Ross, C. A.; Son, J. G. Universal Perpendicular Orientation of Block Copolymer Microdomains Using a Filtered Plasma. *Nat Commun* **2019**, *10* (1), 1–8. https://doi.org/10.1038/s41467-019-10907-5.

(2) Ghoshal, T.; Fleming, P. G.; Holmes, J. D.; Morris, M. A. The Stability of "Ce_2O_3" Nanodots in Ambient Conditions: A Study Using Block Copolymer Templated Structures. *J. Mater. Chem.* **2012**, *22* (43), 22949–22957. https://doi.org/10.1039/C2JM35073D.

(3) Ghoshal, T.; Shaw, M. T.; Bolger, C. T.; Holmes, J. D.; Morris, M. A. A General Method for Controlled Nanopatterning of Oxide Dots: A Microphase Separated Block Copolymer Platform. *J. Mater. Chem.* **2012**, *22* (24), 12083–12089. https://doi.org/10.1039/C2JM30468F.

(4) Ghodsi, V.; Layek, A.; Hegde, M.; Yildirim, B.; Radovanovic, P. V. Native Defects Determine Phase-Dependent Photoluminescence Behavior of Eu^{2+} and Eu^{3+} in In_2O_3 Nanocrystals. *Chem. Commun.* **2016**, *52* (23), 4353–4356. https://doi.org/10.1039/C6CC01122E.

(5) Dhanaraj, J.; Jagannathan, R.; Kutty, T. R. N.; Lu, C.-H. Photoluminescence Characteristics of Y_2O_3:Eu^{3+} Nanophosphors Prepared Using Sol−Gel Thermolysis. *J. Phys. Chem. B* **2001**, *105* (45), 11098–11105. https://doi.org/10.1021/jp0119330.

(6) Joshi, B.; Lee, S. W. Luminescence Properties of Eu^{2+}, Gd^{3+} and Pr^{3+} Doped Translucent Sialon Phosphors. *Journal of Rare Earths* **2015**, *33* (11), 1142–1147. https://doi.org/10.1016/S1002-0721(14)60538-X.